4D PRINTING OF LIQUID CRYSTALS

MARC DEL POZO PUIG

4D Printing of Liquid Crystals

PROEFSCHRIFT

ter verkrijging van de graad van doctor aan de Technische Universiteit Eindhoven, op gezag van de rector magnificus prof.dr.ir. F.P.T. Baaijens, voor een commissie aangewezen door het College voor Promoties, in het openbaar te verdedigen op woensdag 22 december 2021 om 16:00 uur

door

Marc del Pozo Puig

Geboren te Girona, Spanje

Dit proefschrift is goedgekeurd door de promotoren en de samenstelling van de promotiecomissie is als volgt:

voorzitter: prof.dr. F. Gallucci

1e promotor: prof. dr. A.P.H.J. Schenning

copromotors: prof. dr.ing. C.W.M. Bastiaansen (Queen Mary University of London)

dr. M.G. Debije

leden: dr.ir. T.H. Ware (Texas A&M University)

prof.dr.ir. J.M.J. den Toonder

prof.dr. P.Y.W. Dankers

adviseur: dr. L. Florea (Trinity College Dublin)

Het onderzoek of ontwerp dat in dit proefschrift wordt beschreven is uitgevoerd in overeenstemming met de TU/e Gedradscode Wetenschapsbeoefening.

"Crec que la vida ha de ser una festa continua."

I think life should be a continuous party.

– Salvador Dalí

PROPOSITIONS

ACCOMPAYING THE THESIS:

4D Printing of Liquid Crystals

1. From all the stimuli-responsive materials available, liquid crystals are by far the most attractive option for 4D printing. (*Chapter 1*)

2. Good scientific articles are like liquid crystals, success is only achieved when there is order.

3. At the microscale, the identification and tracking of microstructures can be frustrating due to their size. Making them colorful make them easier to locate and to monitor their changes. (*Chapter 2-3*)

4. Advances such as 4D printing are the ones responsible for making science fiction objects reality.

5. Despite the limitations of Lambert-Beer's law, light is still the best way to control large, untethered soft robots. (*Chapter 4-5*)

6. In a society where short visual content is predominant in social media, scientists should have a basic knowledge of graphic design to maximize their outreach.

7. Less is more. (*Chapter 5*)

8. Additive manufacturing should eliminate the need for warehousing in Mars colonies.

9. The manufacturing of centimeter scale 4D objects via direct ink writing is less wasteful than the fabrication of microstructures via direct laser writing by two-photon polymerization. However, it remains challenging to produce recyclable objects (*Chapter 6*)

10. As a Catalan living in the Netherlands, I have concluded that "doei!", screamed very loudly, is the only correct way to say goodbye in Dutch.

— Marc del Pozo Puig

Summary

4D Printing of Liquid Crystals

Additive manufacturing (AM), or 3D printing, consists of building an object from smaller elements deposited in a pre-designed manner. This approach was first intended for small scale, rapid prototyping of new device designs since it has few barriers of achievable geometries. Alongside advances in equipment, expansion of the material portfolio for AM has been dramatic over the last decade, making 3D printing a common tool in many fields. Of special interest is the printing of stimuli-responsive materials, also known as "4D printing", which combines freedom of design with the capacity of the responsive materials to perform untethered, autonomous tasks; making 4D printing appealing to fields such as soft robotics and health care. Common stimuli-responsive materials deposited with AM techniques include shape memory polymers, hydrogels, and liquid crystals (LC). The latter, despite being the latest addition to the portfolio, have the advantage over the earlier materials in that they can deliver programmed, reversible, rapid deformations triggered by different stimuli in both dry and wet environments. LC materials hold great potential when 3D printed, calling for advancement in: (*1*) the design of new LC materials suitable for AM, (*2*) materials that combine different functionalities and stimuli responses, and (*3*) approaches that facilitate multiple, controlled deformation modes in single devices. This thesis explores these three points to advance the state-of-the-art of 4D printing of liquid crystals. The work is divided in two main sections: fabrication of responsive microstructures via direct laser writing by two-photon polymerization (DLW-TPP) (Chapter 2&3) and fabrication of centimeter scale objects via direct ink writing (DIW) (Chapter 4&5).

DLW-TPP consists of the formation of a 3D object by scanning a focused laser beam in a vat of monomers. The reaction mechanism is such that only at the focus of the laser beam polymerization does occur. This grants this technique outstanding resolution. However, when designing a stimuli-responsive photoresist for DLW-TPP a decision needs to be made: high resolution or large deformations. This choice arises because low crosslink-density networks, characteristic for stimuli-responsive materials, can easily swell during the DLW-TPP step. Swelling hampers the maximum resolution attainable during the printing process. To reduce the swelling, one can choose to increase the crosslink density of the network, which in turn improves resolution. However, this also compromises device performance at the same time. Chapter 2 explores the limits of this compromise. A LC-photoresist is designed that results in a network with a high crosslink

density. Distinct 3D microstructures are generated showing sub-micron features. These structures showed only small shape changes upon heating to high temperatures. In Chapter 3, a more optimized cholesteric LC-photoresist is presented using monomers with supramolecular hydrogen bonds and monomers acting as crosslinking loci. As a result, during printing a high crosslink density network is formed by chemical and physical bonding, reducing swelling during the fabrication step and so enabling a high resolution. After DLW-TPP, the supramolecular bonds can be cleaved, lowering the effective crosslink density without significantly effecting the structure's geometry or integrity, allowing the network large shape deformations upon environmental changes. Furthermore, the helical molecular alignment of these structures results in a 1D Bragg reflector. This characteristic structural color acts as an optical sensor for the response of the microstructures to environmental changes in temperature and humidity.

DIW consists of the extrusion and deposition of a material through a nozzle in a pre-determined way; line-by-line a layer is formed, and layer-by-layer a 3D structure is constructed. DIW has demonstrated suitable for printing LC-oligomers with molecules aligned parallel to the printing path, giving both freedom and a high degree of control over the alignment in the 3D object, crucial for pre-programming actuator response. LC-actuators enabled via DIW show inherent response to temperature, but light is a much versatile trigger and a promising platform to control movement in an easy and rapid manner. Chapter 4 shows the design and characterization of a LC-oligomer suitable for DIW that results in a network with temperature-controlled directionality of light-driven bending motion. By carefully combining different stimuli, DIW is used to fabricate a rectangular actuator in which three different deformation modes are shown. Illumination at room temperature result in a bending away from the light source, while at temperatures around 60 °C it bends towards the light source. Temperature by itself induces an anisotropic expansion-contraction. Furthermore, this actuator functions in both wet and dry environments. Chapter 5 studies the use of this material to fabricate actuators with multiple deformation modes while combining multiple functionalities in one device. This is accomplished by printing different patterns on top of a thermoplastic sheet with a thickness of 10 µm. By carefully illuminating areas of the patterns, or their entirety, different distinct, controlled light-driven deformations are achieved underwater. In addition, the possibility of combining multiple functionalities in a single device is demonstrated by printing a photonic material between the light-responsive pattern. This approach in fabricating bilayers via DIW explores how amphibious actuators that show diverse and controlled deformation modes while having various functionalities can be produced.

Chapter 6 puts the advances demonstrated in this thesis for the fabrication of micro- and centimeter scale stimuli-responsive objects in context. In addition, suggestions on new research areas to pursue in terms of material and use of AM techniques are offered.

Overall, this thesis elucidates new LC materials suitable for different AM techniques and on their use for the fabrication of devices that show multiple functionalities or/and deformations modes. The results shown here bring autonomous untethered 4D printed liquid crystal devices one step closer to widespread deployment.

Table of Contents

Frequently used abbreviations:

3D	three-dimensional
4D	four-dimensional
AM	additive manufacturing
CAD	computer aided design
CLC	cholesteric liquid crystal
DIW	direct ink writing
DLW-TPP	direct laser writing by two-photon polymerization
DSC	differential scanning calorimetry
GPC	gel permeation chromatography
H-NMR	proton nuclear magnetic resonance
LC	liquid crystals
LCE	liquid crystal elastomer
LCN	liquid crystal network
N	nematic
POM	polarized optical microscopy
RM	reactive mesogen
RT	room temperature
SEM	scanning electron microscopy
Sm	smectic
TPA	two-photon absorption
TPP	two-photon polymerization
UV	ultraviolet

Chapter 1

Additive Manufacturing of Liquid Crystals
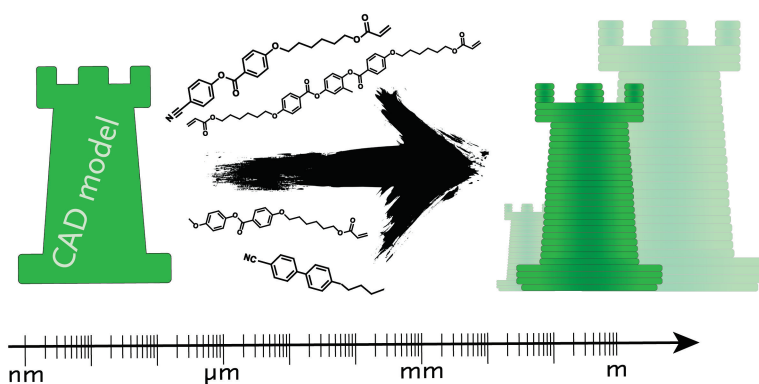
Abstract

Recent years have seen major advances in the developments of both additive manufacturing concepts and stimuli-responsive materials. When these two are combined in a process known as 4D printing, the result can lead to functional devices for use in health, energy generation, sensing, and soft robots. Among responsive materials, liquid crystals -which can deliver programmed, reversible, rapid responses in both air and underwater- are a prime contender for additive manufacturing, given their ease of use and adaptability to many different applications. In this chapter the junction between liquid crystals and additive manufacturing is introduced by using selected examples that embody the current state-of-the-art of this exciting, emerging field.

1.1 Introduction

Additive manufacturing (AM) is a bottom-up approach that builds an object from smaller elements by consecutively adding them step-by-step. The initial use of AM was for rapid prototyping of device designs, usually with inferior materials optimized for production speed at the expense of final material or device properties.[1] In development for about four decades, AM has now achieved greater public recognition, and is being applied in a growing variety of academic and industrial fields to produce performance materials and devices. AM is beginning to be considered a manufacturing technique in its own right—its forte being ease of use (no large industrial machines are required), ease of model design (any personal computer can be used to generate designs) and a growing library of materials available for printing, ranging from thermoplastics to cement.[2] Control of AM techniques is such that objects can be manufactured spanning from micrometers[3] to tens of meters:[2] consider the wide variety of current uses of AM, including in aviation,[4,5] biomedical and tissue engineering,[6–8] dietary,[9,10] construction,[2,11,12] garment design,[13] laboratory wares,[14,15] water purification,[16] and sensing applications.[17–19]

Most of the materials used in AM have essentially been static. What is needed for new applications are materials that can react to changes in their environment, autonomously altering their properties to perform untethered tasks, which are most desired for compliant soft robotics for healthcare,[20] or devices that work at the human-machine interface or handling fragile objects.[21] This is where the term "4D printing" originates: a printed object generated from stimulus-responsive materials (sometimes called "smart"). Since both the geometry and responsivity of the materials can be tuned, impactful applications are envisioned for 4D printed devices.[22,23] Among the different stimuli-responsive materials available, liquid crystals (LC) polymers are emerging as a prime contender as they deliver pre-programmable, reversible, anisotropic actuation in both dry and wet environments while having tunability in terms of material properties and stimuli that triggers their response. LCs have a proven track record as "smart" materials in a wide variety of application fields, including water purification, optical sensing, display technology, energy management, and as artificial muscles.[24–32] Despite LCs being a recent addition to the materials library used in 4D printing, they are already proving to be an appealing alternative to the conventional stimuli-responsive materials such as hydrogels or shape memory polymers which cannot show response in dry environments or reversible deformations, respectively.[33–43] 4D printing of LC is still in its infancy, and further development of the material and applications are imperative to truly unleash the potential of this young, rapidly-advancing, and exciting field.

1.2 Additive Manufacturing Techniques

Over the past four decades, since the introduction of stereolithography (SLA)[44] and fused filament fabrication (FFF, also commercially known as "fused deposition modeling", FDM),[45] the two most known techniques, additive manufacturing has been the umbrella term encompassing 3D printing techniques.[1] These techniques can be classified in different branches, but all have one thing in common: fabrication of 3D objects by depositing and/or solidifying material in place, rather than sculpting an object out of a larger material block. The process always starts with a computer-assisted design (CAD) which is "sliced" into layers using software that generates a fabrication instruction file for the printing equipment (**Figure 1.1**) written in "G-code". When creating this instruction file, decisions are made affecting the structure's fidelity to the CAD design (degree of correspondence of the final print to the intended structure in the CAD model) and its physical integrity (the physical "stability" of the print resulting from proper adhesion between layers). Depending on the layer thickness chosen, less or more layers are used in fabrication: the more layers,
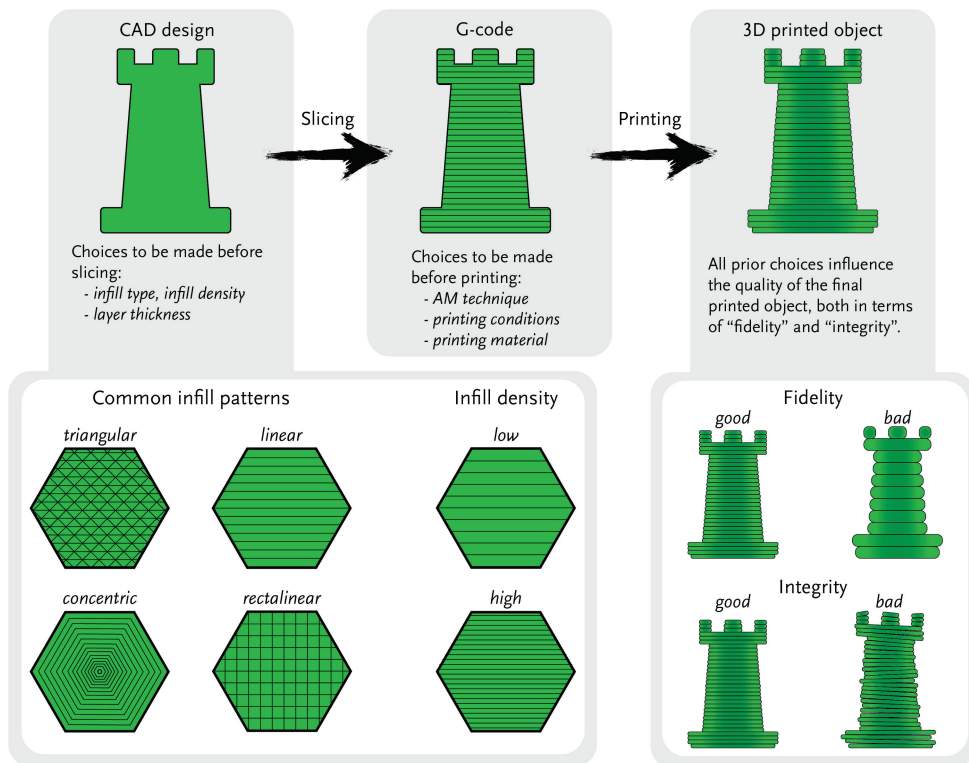
Figure 1.1 Schematic describing the process from a CAD design to a 3D printed object.

Powder fusion

Length scales available
to common AM techniques:

Inkjet printing

(Micro)extrusion

Vat photopolymerization

nm   μm   mm   m
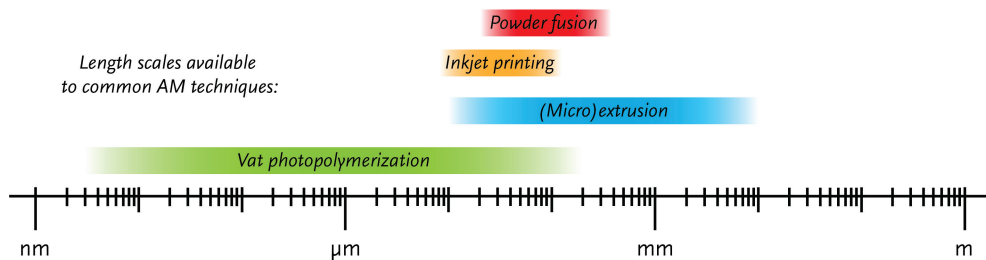
Figure 1.2 Overview of the most common additive manufacturing type classified by the resolution typically achieved.

the more faithful the final object to the original design. In some techniques, the layer "infill" also needs to be defined, the infill being the track pattern which the individual physical print lines follow in building the layers. There are several options for infill: rectilinear, concentric, or triangular, among others (**Figure 1.1**). For anisotropic materials aligned by the print path direction, such as liquid crystal elastomers (LCE), the type and density of infill can strongly affect the final mechanical properties in all three spatial dimensions (*see Section 1.5*).[39,46,47] What determines the technique best used for the print is dictated by the structure's dimensions and the properties of the materials chosen to create it. As shown in **Figure 1.1**, in each step of the process different decisions are made which affect the final structure.

For fabrication of LC-based 3D objects, two categories of AM techniques have been primarily used: vat polymerization and 3D microextrusion.[33–37,39,40,46,48–51] Each branch is suitable for specific classes of LC monomers. Vat polymerization is appropriate for low molecular weight mesogens, and 3D microextrusion for mesogenic oligomers.[52] For each technique there are equipment options, each with different resolution as shown in **Figure 1.2**. Vat polymerization tends to have a higher resolution than microextrusion, and so it is often used for fabrication of microstructures, while 3D microextrusion is typically employed for millimeter- to centimeter-scale objects. These two branches will be discussed in more detail in *Section 1.4* and *Section 1.5* after LC have been properly introduced in the next section.

1.3 Liquid Crystals

Over the past fifty years, advances in the LC field have expanded them out of liquid crystal displays (LCDs) and into functional devices of all kinds, and now into the AM world. As materials that can

be molecularly aligned, they are the ideal constituents for bottom-up construction of responsive objects. Situated between ordered solid and isotropic liquid phases (abbreviated as "I" or "Iso" in the LC literature), the LC phases combine molecular orientational order with the ability to flow and reorient when an appropriate trigger is imposed, first seen over 150 years ago.[53–55] This stimuli-responsive molecular reorientation is the basis of their wide applicability in stimuli-responsive, "smart" materials.[24] In the 1970s, the first compounds with liquid crystalline properties at room temperature (RT) were developed for LCDs,[56] which also ushered in a time of wider applicability of this class of matter. Since then, many different LCs have been developed for a variety of applications, as well as LC mixes aimed specifically for AM techniques.

LC phases are also called "mesophases" (after Ancient Greek μέσος, *mésos*, "middle, between"), and the molecules "mesogens". LC phase behavior can be a function of temperature ("thermotropic"), or for those that occur in solution, dependent on both temperature and concentration of LC in the host medium ("lyotropic").[57] Thermotropic mesogens have strongly anisotropic geometries, whether disc-shaped ("discotic") or rod-like ("calamitic") (**Figure 1.3a**), although there are even more possibilities, such as bent-core.[58]

Here, only thermotropic, calamitic LCs and their uses, are considered given their leading position in stimuli-responsive materials for 4D printing.[24,29,59,60] Additionally, there are liquid crystal polymers (LCPs) that are not liquid crystalline in bulk at room temperature like the low-molecular weight molecules discussed here, but show LC phases during processing. The initial molecular alignment is retained which gives these materials—such as polyaramids—their exceptional anisotropic mechanical properties.

Low molecular weight calamitic mesogens are conventionally constructed from a stiff core built using a (series of) ringed structures (phenyl, pyridyl, cyclohexyl) substituted with flexible alkyl chains of variable lengths, typically C_3 up to C_{12} (**Figure 1.4**). Given a suitable environmental temperature, these mesogens self-organize into a nematic phase (N) wherein the molecules display orientational order; some mesogens can form one of many smectic phases (Sm), which combine orientational with spatial ordering (**Figure 1.3b**). The averaged direction of the molecular long axes of the mesogens is described as the molecular director (**n**) (**Figure 1.3c**). Numerically, the degree of alignment order can be described with the order parameter (*S*), defined as:

$$S = 3\langle \cos^2(\theta) - 1 \rangle / 2 \tag{1}$$

with θ being the tilt of a mesogen relative to **n**. Typical nematic mesophase S-values are 0.5 to 0.6,[31] with smectics having slightly higher order (0.7-0.8).[61] S can be determined using optical[62] or X-ray scattering[63] methods.

As a result of the anisotropic shape of calamitic molecules, the dielectric properties are also anisotropic; a trait at the root of the "smartness" of many LCN-based devices. This is expressed as two orthogonal relative permittivity values, extraordinary (ε_e) and ordinary (ε_o). Depending on the difference, $\Delta\varepsilon=\varepsilon_e$ -ε_o, the mesogens will reorient along ($\Delta\varepsilon > 0$, positive dielectric) or against ($\Delta\varepsilon < 0$, negative dielectric) imposed electric fields. The inherent link between ε and index of refraction (n) means that LCs also have two refractive indices, extraordinary (n_e) and ordinary (n_o), which when the mesogens are aligned over large length scales, expresses itself as birefringence ($\Delta n= n_e$ - n_o) (**Figure 1.3d**). This birefringence allows users to swiftly recognize alignment patterns and mesophases by observing samples held between crossed polarization filters.

Classes of Liquid Crystal Alignments

The molecular order is an important characteristic of LCs that has a direct effect on the quality of its anisotropic properties and how it responds to external stimuli. Thus, controlling the molecular alignment during the 3D printing process is imperative. The mesogenic orientation can be homogenized at the macroscale by imposing boundary conditions. These boundary conditions can be obtained via treating the substrate surface(s) chemically, applying electric or magnetic fields, or using mechanical force fields such as shear or elongation. AM techniques where the LC is in a vat generally use treated surfaces in the vat or electric/magnetic fields across it. Extrusion-based AM mostly depend on process-inherent elongation and shear of the ink for alignment. Typically, the bulk of the material is first heated to the isotropic temperature and then cooled down to the LC phase (**Figure 1.3e**) in which depending on the boundary conditions imposed different organization of the mesogens can be obtained. The most common arrangements have names that helps their identification: when they are aligned parallel ("planar"),[33] perpendicular to the substrate ("homeotropic"),[64] with mesogens aligned parallel to the surface plane at one side and perpendicular to the surface plane at the other ("splay"),[51] or with the mesogens at different surfaces pointing in different directions("twisted")[65] (**Figure 1.3f**).

A self-induced helicoidal alignment pattern in the bulk of the material can be attained by adding a chiral molecule to a nematic LC. This forms a chiral nematic (N*), or "cholesteric" (Ch), phase. When the periodicity of the mesogenic rotation is at the same scale as the wavelength of
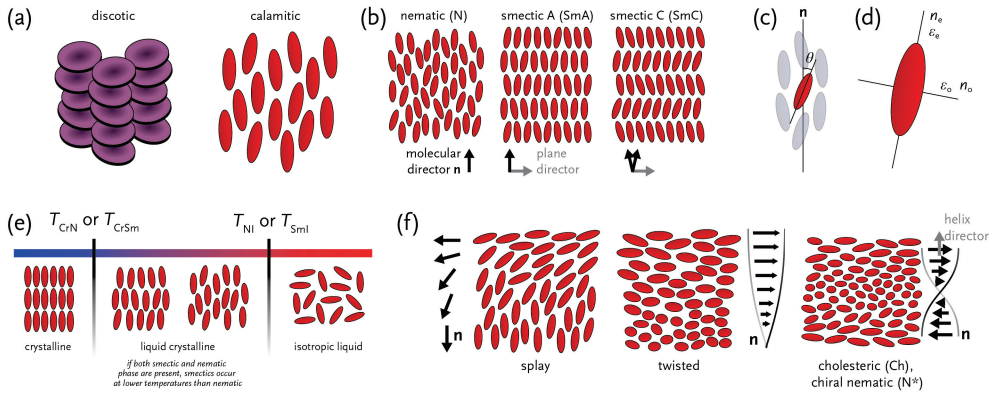
Figure 1.3 Schematic drawings of (a) discotic and calamitic mesogens in an unspecified mesophase. (b) Typical calamitic mesogen alignments in the nematic (N), smectic A (SmA), and smectic C (SmC) mesophases. Visualized underneath are the molecular directors **n**. (c) Molecular orientation and angle θ with respect to the molecular director **n**. (d) Orientation of ordinary (n_o) and extraordinary (n_e) refractive indices and relative permittivities (ε_o, ε_e). (e) Generalized temperature-dependence of calamitic mesophases between crystalline (Cr) solid and isotropic (I) liquid. (f) Splay, twisted, and chiral nematic/cholesteric (N*/Ch) director configurations and the associated local molecular directors **n**. Also shown for cholesteric is $p/2$, half the length of a full 360° rotation (the "pitch") of **n**.

light, selective reflection of light can occur, similar to a one-dimensional Bragg reflector,[28] but in this case the circular polarization of the reflected light matches the helical pitch of the cholesteric, either right- or left-handed. The birefringence of the host LC determines the width of the reflection band, while the concentration of chiral dopant dictates the central wavelength of reflection. The alignment periodicity is quantified with pitch length (p), which is the distance taken for a 360° rotation of **n** along the helix director (**Figure 1.3f**). For reflection in the visible region of the electromagnetic spectrum, this means p is required to be in the hundreds of nanometers. Multiple factors influence the reflected wavelength (λ_{max}) and width of the reflection band ($\Delta\lambda$), these being the average refractive index of the LC ($\langle n \rangle$), "helical twisting power" (HTP) of the chiral dopant, and its weight fraction (x). These are connected through the following equations:

$$\langle n \rangle = (n_e + 2n_o)/3 \tag{2}$$

$$p = (HTP \cdot x)^{-1} \tag{3}$$

$$\lambda_{max} = p \langle n \rangle \cos(\theta) \tag{4}$$

$$\Delta\lambda = (n_e - n_o)\, p \tag{5}$$

The helical twisting power is perhaps the most abstract variable in this set. Briefly, it is a property deriving from the unique interactions between the chiral dopant species and the LC mixture, defined with units μm^{-1}. Larger HTP means a lower weight fraction is required to reflect a given wavelength, while the sign of HTP indicates whether the resulting helix is left-handed (−) or right-handed (+).

Liquid Crystal Networks and Elastomers

Macroscopic expression of liquid crystalline properties, such as birefringence and thermal contraction, requires the presence of molecular ordering. Normally, this only occurs in the LC mesophases, which are situated at defined temperature ranges, typically above room temperature. This temperature range can be extended by fixing the molecular alignment of the mesogens into a chemically bound polymer network. Calamitic reactive mesogens (RMs), LC mesogens modified with crosslinkable chemical end-groups either at one or both ends of the mesogen (**Figure 1.4a**), were first developed in the 1980s.[66] A selection of common materials and their names are given in **Figure 1.4b**. By reacting the crosslinkable chemical groups, the RMs are chemically bonded, fixing the mesogenic alignment pattern (**Figure 1.4c**). This densely crosslinked material is known
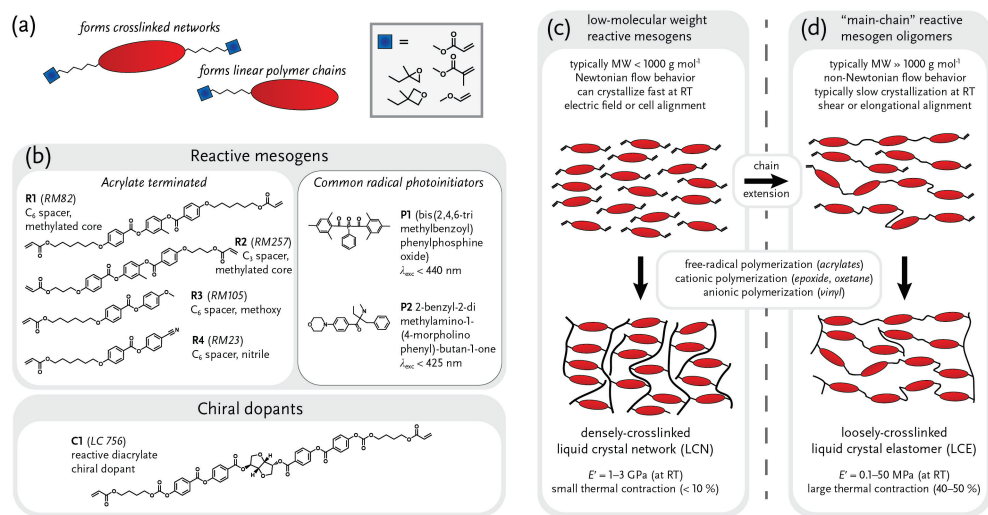
Figure 1.4 (a) Visualization of reactive mesogens (di- and mono-substituted) and the reactive functional groups commonly encountered. (b) Molecular structures and common names of some typical mesogens used in reactive LC research. (c) and (d) are schematic drawings of the monomers used to make LCNs and LCEs and characteristic figures defining each class. Idealized network structure for LCNs and LCEs after crosslinking, and common mechanical properties.[29]

as an liquid crystal network (LCN). LCNs characteristically have glass transition temperatures (T_g) above RT and high crosslink densities.[60]

Reducing the crosslink density can be accomplished by forming LC oligomers by chemically concatenating RMs before crosslinking. Crosslinking LC oligomers leads to a loose network, known as an liquid crystal elastomer, LCE, which are, as the name suggests, more "elastic"; they typically feature viscoelastic, non-Newtonian flow behavior[46,67,68] with large strain-at-break values and low elastic moduli at RT compared to the densely crosslinked LCNs (**Figure 1.4d**).

Liquid Crystal-based Actuators and Triggers

Molecular alignment coupled with chemical crosslinking is the basis of many "smart" applications, including 4D printing of LCs. The most basic actuation arising from planar and homeotropic crosslinked networks is thermal contraction, but many other, more complex motions are possible. With increased temperature, mesogens making up LC networks naturally lose order—the "order–disorder transition"—which in the case of an aligned network leads to contraction along **n** as the mesogens pull the network together through their crosslinked ends, and expansion perpendicular to **n**. As a result, a temperature change acts as the trigger for the response of the actuator.

Reduced crosslink densities, as found in LCEs, leads to large contractions, since the order–disorder transition is given more freedom to strain the network.[69] As a result, LCNs contractile strains are generally below 10 %,[29] being restricted by the high crosslinking density; while in cross-linked LCEs, values up to 50 % are common. When it comes to designing an 4D printed object with LCEs, the two distinguishing features—freedom in structural design, and mesogen alignment—are best used in synergy. As depicted in **Figure 1.5**, the molecular alignment of the liquid crystals determines the direction of contraction and/or bending. For example, a strip with uniaxial molecular alignment leads to contraction along a single direction (see **Figure 1.5a**), a design suited for artificial muscles. In cholesterics, since there is a continuously rotating molecular director distribution along the helix director, disorder leads to expansion along this helix director and a slight contraction in-plane.[70] Out-of-plane deformation, similar to the workings of a hinge, can be accomplished with molecular director patterns such as splay and twisted (see **Figure 1.5b**). Twisting actuation results from actuator with their long axis offset from **n**.[71] Similarly in liquid crystalline particles the molecular director determines the deformation of the particles.[72–76] Additionally, by more intricate patterning of the alignment, highly localized responses can be generated leading to functional actuation pathways.[77] Concentric and azimuthal alignment patterns can also

result in out-of-plane actuations, as these concentrate stresses to a single point (**Figure 1.5c**).[78,79] Tiling multiple concentric domains together leads to the formation of multiple cones within a single film, which can be used to lift masses.[80,81]

The influence of the fabricated object's macroscopic shape has been demonstrated in thin-film LCN devices. Planar films produced with the length cut at angles oblique to **n** lead to coiling upon actuation.[71,82] In splay films, having **n** on the planar aligned side parallel to the film's long axis ("**n ∥** film") forms a thin coil, while having "**n ⊥** film" leads to tube formation (this does not hold for twisted alignments). To add variability, the degree of bending is inversely related to the film thickness, thereby serving as an additional design parameter;[83] and by varying thickness along the film, in essence creating a wedge, the amplitude of the bending can be dramatically enhanced, resulting in tightly rolled films (**Figure 1.5d**).[83] Thus, it is not only the molecular alignment, but also the geometry that has a significant role in actuator performance. Normally, combining domains of different alignments within a single film requires intricate alignment procedures, so assemblies of multiple LCN films have been explored in preference (**Figure 1.5e**). Orienting films in an assembly where they bend towards each other has been used as grippers and feet.[84–87] A film with localized director patterns and cuts in strategic locations can lead to the reversible opening and closing of those cuts through actuating the LCN.[88] Combining an LCN with a support material in a bilayer fashion can also guide the film to bend or curl, akin to bimetallic strips.[89,90] For more information on different alignment-shape combinations, the reader is referred to reviews that showcase actuator designs and principles.[25,26]

Temperature is not the only stimulus, trigger, available for generating the order–disorder transition that triggers the reversible actuation of LC networks (see **Figure 1.6** for common environmental responsivities). Light responsivity is typically obtained by including a dopant in the host LC network that either generates local heating (a photothermal effect), or changes its conformation (a photomechanical effect) upon light exposure.[91,92] Both mechanisms appeal to different applications. In a photothermal effect, the dopant absorbs light and subsequently releases the energy, increasing the local temperature of the network, generating a physical response. Upon removing the light source, the sample rapidly cools, and the response reverses. In the photomechanical response, the dopant changes its configuration and conformation upon absorbing light, forcing molecular re-arrangements and triggering stress in the network. By photoisomerizing, the molecules generate a photomechanical contraction of the network along the molecular director, which is transduced to the macroscopic object as a contractile strain which can last for months

depending on the lifetime of the isomer.[26,60] Additionally, physical response to humidity can be integrated in the LC network by incorporating mesogens with hygroscopic groups which attract environmental moisture: a controlled swelling of the network is achieved dependent on the volume of water taken up. Hydrophilic blocks[93] or polar groups[24,94] are incorporated to make the LC water-absorbant. Polar groups (carboxylic acids or tertiary amines) are not yet sensitive to humidity immediately after polymerization: to become active, these must be converted into a salt using
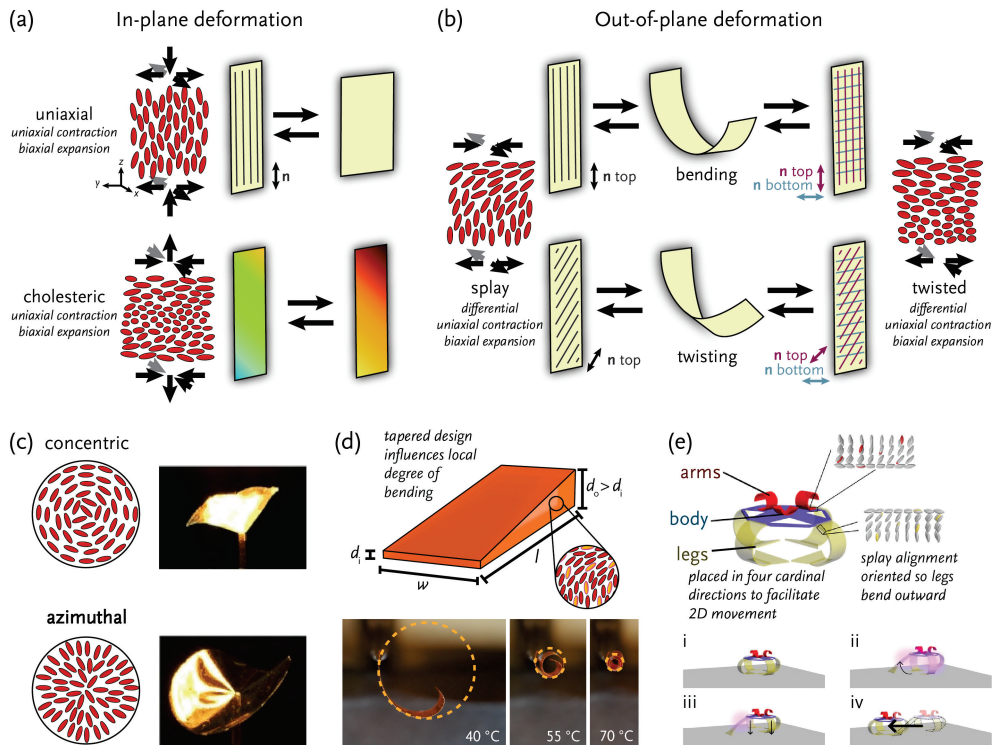
Figure 1.5. Contraction and expansion directions for different LC alignments in response to increased disorder: (a) uniaxial, cholesteric, (b) splay, twisted. (c) Complex alignment patterns concentric and azimuthal depicted schematically and their response when crosslinked into an LCN. Adapted with permission.[79] Copyright 2012, Wiley-VCH. (d) Schematic drawing of a tapered actuator design with photographs showing the obtained effect upon actuation. Adapted with permission.[83] Copyright 2019, Royal Society of Chemistry. (e) Example of an assembly of LCNs in which the alignments and orientations of different actuators have been chosen in such a way that 2D movement is possible. Steps (i) to (iv) illustrate the steps that make up a full "walking cycle": (i) walker in its original location, (ii) legs perpendicular to intended movement direction irradiated, leading these to bend outward and temporarily lift the robot, (iii) front leg is triggered to bend forward, and finally (iv) the leg retracts, pulling the walker into the intended direction. Adapted with permission.[86] Copyright 2020, Wiley-VCH.
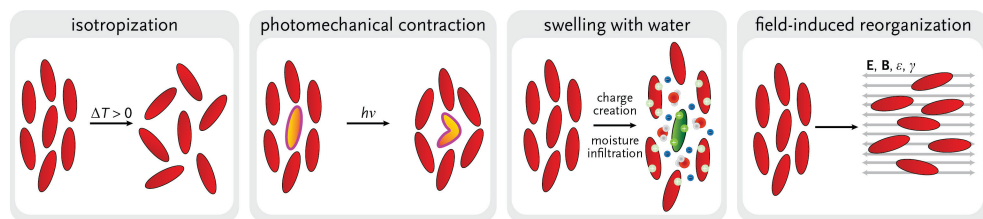
Figure 1.6 Idealized schematic drawings of molecular responses to four different stimuli: temperature (isotropization), photomechanical (photoisomers), swelling in response to water uptake, and field-induced reorganizations (typical examples E: electric, B: magnetic, ε: strain, γ: shear).

alkaline or acidic aqueous solutions, respectively. Finally, besides orchestrating a molecular reorientation, electrical and magnetic fields can also be used to trigger thermal actuation. This can for example be done by loading the LC with a conductive liquid metal,[95–97] or by creating a bilayer of LC and iron doped polydimethylsiloxane (PDMS) layers, where exposure to strong magnetic fields causes induction heating of the sample.[98,99]

1.4 Vat Polymerization of Liquid Crystals

In vat polymerization, localized crosslinking is induced in a bulk of a light-sensitive material, typically known as the "photoresist", using light of specific wavelengths, with a resolution generally between 0.1-100 μm.[1] Direct laser writing by two-photon polymerization (DLW-TPP, **Figure 1.7**), a vat polymerization technique, has become the favorite fabrication method for researchers producing functional microscale structures as it offers both sub-micron resolution and freedom of structural design compatible with a wide variety of photoresists.[100–104] As a result, fabrication of micronscale LC objects has been accomplished mainly via DLW-TPP, which has led to devices as diverse as microgrippers,[51] microlenses,[105] microwalkers,[33] or different photonic elements.[35,40]

In short, DLW-TPP, also known as "multiphoton lithography", is a technique that relies on the non-linear optical process of "two-photon absorption" (TPA) to perform localized crosslinking the vat of monomers. TPA requires an extremely high photon density, as two photons need to be simultaneously absorbed to initiate polymerization. This high photon density can be achieved by focusing a femtosecond laser, typically a ~780 nm fs-pulsed Ti:sapphire, which concentrates the photons temporally; by using a microscope objective to focus the light, the photons are also concentrated spatially. The photon flux is the greatest at the focal point and exponentially decreases from there. Only at the focal point is the density of photons high enough for TPA to occur,

implying polymerization only occurs at the focus. By scanning the focal point through the bath of material, polymerization can be induced anywhere in the resist bath; a feature not possible with SLA or digital light projection (DLP), other vat polymerization techniques, in which polymerization can only occur at the surface of the vat as these rely on single-photon initiation of the crosslinking reaction. The 3D focal point has an ellipsoidal shape, with an equal length in the x- and y-axes, typically around 60 nm, and slightly elongated in the z-axis, this being ~180 nm;[106] both the shape and dimensions are influenced by the laser intensity and the numerical aperture (NA) used.[107,108] Because of the small dimension of the focal point, the resolution of this technique is ~20 nm to 5 µm:[1,109,110] final resolution is critically dependent on both the material and the printing parameters. After the fabrication exposure steps, any unreacted monomer is typically removed during a "developing" step to obtain the final object.

Direct Laser Writing by Two-Photon Photopolymerization in Liquid Crystals
An LC photoresist for DLW-TPP must contain the following: (*1*) difunctional mesogens to act as crosslinkers to form the network and fix the alignment in place, (*2*) monofunctional mesogens to provide flexibility to the network, and (*3*) a two-photon photoinitiator. However, a fourth condition can be imposed by the DLW-TPP equipment: (*4*) the material must have a stable LC phase at RT when there is no heating stage. Most reported LC mixtures satisfy the first three requirements, but their LC phases typically exist above RT or crystallization at ambient conditions occurs after only a few minutes, reducing the available printing time, and hence making these mixtures generally unsuitable for printing. While actual printing times may vary, in our experience single micrometer-scale structures require a few seconds to complete, while structures on the order of a few hundred micrometers take minutes. What usually takes the longest is the period between filling the LC alignment cell and the actual onset of printing, which can take half an hour. This latter restraint imposed by the equipment can be overcome, for example by custom stages allowing heating of the mixture during printing.[111,112]

Other factors are relevant when selecting the mesogens for the LC photoresist. In general, stimuli-responsive objects are typically based on low crosslink density materials, and as a result suffer from swelling with the surrounding monomer both during and after the DLW-TPP process,[113–115] reducing resolution. When working with LCs, swelling can be avoided by increasing crosslink density, that is, the fraction of mesogens with two reactive end groups, which in turn improves the resolution achievable with the resist. Nonetheless, when working with acrylate-terminated monomers, increasing the fraction of bifunctional mesogens augments polymerization

shrinkage. The use of epoxide and oxetane mesogens rather than acrylates can be used not only to reduce polymerization shrinkage, but also to ensure oxygen insensitivity during polymerization and a lower processing viscosity.[111,116] Despite their advantages, epoxide-based LCNs are still in their early stage when compared to acrylate-based LCNs.

The ratio of difunctional to monofunctional mesogens is an important parameter affecting the structure's resolution, but increasing the crosslink density degrades the performance of the actuating structures, as both speed and amplitude in actuation response are reduced.[114] This effect can be exploited to obtain non-reciprocal motion in microstructures that have regions composed of mixtures containing different ratios of difunctional to monofunctional mesogens, thus differing crosslink densities.[117]

Adding dopants to an LC photoresist may allow integration of additional optical properties,[35,37] response to different stimuli, *e.g.* light,[33,118] humidity,[37] or electric field,[40] and/or improve the mechanical performance of the network.[50] The two most important considerations when choosing a dopant are: (*1*) it should not disturb the LC alignment and (*2*) it should be transparent to the laser light, or at least not compete with TPA. The former can be easily satisfied by choosing a dopant that has dimensions and shape like the rod-like LC mesogens, while the latter is more specific to the material and chemical groups possibly present in any dopants. The reader is directed to the following literature for a guide on how to tune LC-photoresist to obtain response to different stimuli.[52]

Additionally, there are several tunable printing parameters that not only influence a structure's fidelity to the computer design, but, in the case of DLW-TPP in LC photoresists, also affect the characteristics of the network formed, and even how the final print actuates. **Figure 1.7** displays these parameters and summarize their effects, for further explanation the reader is directed to the literature.[52]

4D Printed Micrometer Scale LC Structures

Using DLW-TPP, a wide variety of LC microstructures have been fabricated. These can be classified in groups according to different criteria, *e.g.* trigger of the response, application, properties, etc. Here, they are categorized in two different groups according to the structure's intended purpose. Thus, structures that show a shape deformation triggered by an external stimulus are grouped as micro-actuators and structures that have shown to interact with light, either because of their molecular arrangement or due to their dimensions, are grouped as photonic

microstructures. As a result, some structures that could be considered micro-actuators are grouped with photonic structures since they use the anisotropic shape of the network to obtain dynamic optical properties.

Micro-actuators

The key feature of micro-actuators is that there is a triggered shape change upon exposure to an external stimulus. LCs allow for the fabrication of micro-actuators that show a wide variety of pre-programmed shape deformations triggered by different external stimuli. Here, we will discuss somes examples of LC micro-actuators grouped by the stimulus that triggers their response.

LCNs are inherently responsive to temperature changes; however, most of the work on LC-based micro-actuators has not focused on characterizing their response to this stimulus. This could be because it is difficult to analyze this response in microstructures and it is challenging to induce a controlled temperature change in only a single micro-object. Nevertheless, there is one example consisting of a hybrid system: LCN films that have embedded and epoxide-based micro-patterns.[111] The epoxide-based micropatterns are first produced via DLW-TPP inside a cell, after which the non-reacted epoxide mesogens are removed and substituted by acrylate-functionalized
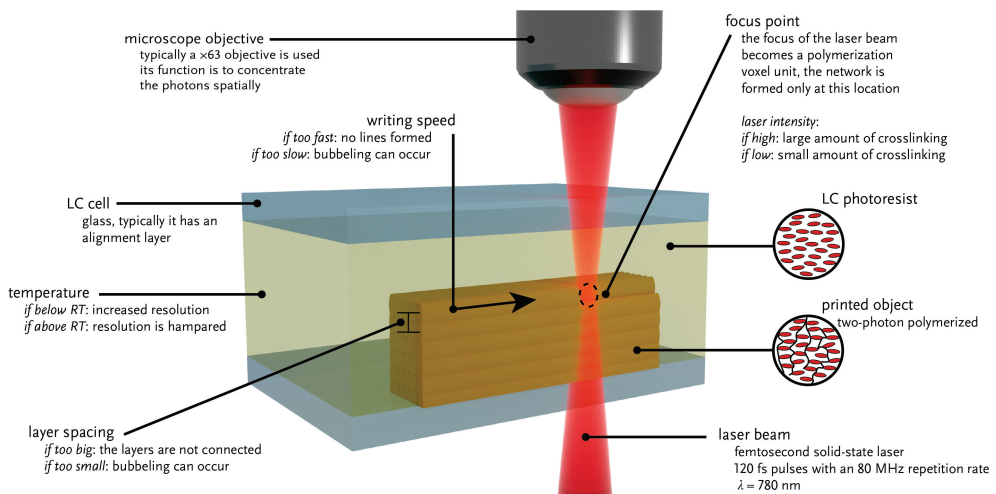
Figure 1.7. Schematic representation of the printing process of LCs in DLW-TPP. In the drawing, the different user-adjustable parameters are highlighted: the writing speed, laser intensity, temperature, and layer spacing. The insets for LC photoresist and LCN show an example for an approximate orientation of the mesogens, in this case planar, in the vat and after polymerization, which are typically the same.

mesogens that are used to then polymerize a film around the epoxide-based micropattern. The advantage of having a micropattern of a different material in the film comes from the enhanced mechanical and actuation performance of the composite which can be tuned by changing the geometry and dimensions of the patterns.

The first LC-based light-triggered microstructure, a microwalker formed by a body of planar aligned LC with four conical legs of a commercial, isotropic acrylate resin ("IP-Dip"), was
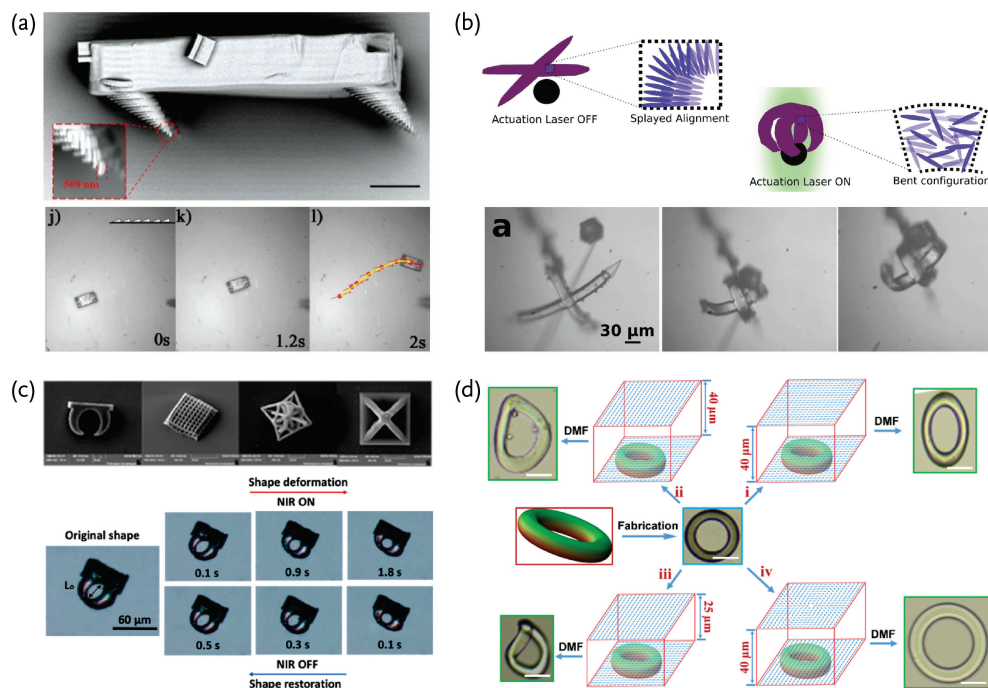
Figure 1.8 (a) A light-fueled microwalker. Top scanning electron microscopy (SEM) image of the walker, scale bar 50 μm. Bottom, electron micrograph sequence that shows the walker movement upon illumination with a green laser. The topography of the surface is shown on the top left of the sequence. Adapted with permission.[33] Copyright 2015, Wiley-VCH. (b) An autonomous light-responsive gripper. On the top, a scheme showing the mechanism for the response to grasp an object. On the bottom, micrographs showing the "microhand" in action. Adapted with permission.[51] Copyright 2017, Wiley-VCH. (c) NIR light-responsive microstructures. On the top, SEM images showing diverse 3D geometries. On the bottom, micrograph images showing the response of structures to near-infrared light. Adapted with permission.[50] Copyright 2019, American Chemical Society. (d) Various 3D-to-3D shape deformation from the same geometry, in this case a ring. The distinct deformations are accomplished by fixing different molecular alignment in the ring. Scale bars represent 50 μm. Reproduced under the terms of the Creative Commons CC BY license.[41] Copyright 2020, Wiley-VCH.

produced in 2015 (**Figure 1.8a**).[33] Upon illumination with a 532 nm (green) laser, the body contracted anisotropically, and when the light was turned off, it expanded to its initial state. Due to the rapid response of the body to a pulsed laser beam, the object could walk. Later work reported an autonomous light-responsive "microhand" composed of two strips forming a cross, each having splay alignment (**Figure 1.8b**).[51] Upon illumination, the strips bent, closing the hand. Again, when the light was turned off, the hand recovered its initial state. Autonomous motion was achieved, as light would be redirected by an object passing in front of the hand, triggering the response, and allowing the hand to catch objects by itself. More recently, there have been reports of 3D planar samples expanding anisotropically upon illumination with near-infrared (NIR) light (**Figure 1.8c**).[50] In all these light-responsive micro-actuators, both to green and NIR light, the actuations were based on photothermal effects. Photomechanical actuation in LC-based micro-actuators has yet to be reported, but it would be more desired than photothermal actuation in some applications, so worth exploring.

Response to ambient changes such as humidity and temperature, or to solvents, can also be desirable. In these cases, the response comes from the swelling of the network, expanding perpendicularly to the molecular alignment. This anisotropic swelling has been explored in microstructures that present different molecular alignments in the same geometrical object shape (**Figure 1.8d**).[41,65] As a result, different deformation modes triggered by swelling in N,N-dimethylformamide (DMF) could be obtained depending on the LC alignment. The solvent triggered an abrupt actuation, while humidity changes, in contrast, result in a gradual actuation which can be much desired in some applications.

Photonic Microstructures
A microstructure is considered photonic when it interacts with light, mainly through reflection and diffraction in printed materials. This can occur at two different length scales: the molecular level when the light is modulated by chromophores in the material itself, and/or the nanometer to micrometer scale when light interacts via the geometry and periodicity of the structural features. Owing to the optical anisotropy of LCs, it is possible to fabricate photonic microstructures that interact with light simultaneously at different length scales.

As described in *Section 1.3*, when a chiral molecule is added to an LC mixture, the mesogenic planes can self-organize in a helical fashion, known as cholesteric alignment, resulting in a chiral 1D photonic crystal, forming a photonic polymer, also known as a cholesteric liquid crystalline

(CLC) network. The use of the cholesteric alignment comes with the advantage that the physical shape of the print can be chosen arbitrarily and, coincidentally, the first DLW-TPP LC photonic microstructures had this alignment.[119] This early work focused on studying defect modes in CLCs by polymerizing regions at the top and bottom of the cell while leaving the intermediate region with unreacted monomers, in essence creating a polymer-monomer-polymer sandwich. After polymerization, the pitch length elongated, while the pitch length in the unreacted regions was reduced, modifying the selective reflective bands (SRB) of each region, in which microscopic indented frames allowed a fine control of the shift of the SRB (**Figure 1.9a**).[120] The contrast between the SRB of the monomer and the polymer results in stable temperature-responsive defects.[119] These photonic microstructures have the potential to become stimuli-responsive narrow band-pass filters, heat sensors in integrated optical circuits, or/and advanced optical and photonic components.

Instead of making use of the cholesteric alignment to fabricate structures in which the materials themselves interact with light, the inherent birefringence of the LC can also be used. When combining electrically addressable LC photoresists with DLW-TPP, the molecular alignment during fabrication can be easily controlled and tuned.[40,121–123] Hence, during fabrication, different molecular alignments can be fixed. As a result, one can accomplish complex spatial variations on the birefringence inside the cell, as the polymerized regions and the surrounding monomer can have different molecular alignments.[122] When that is the case, the optical mismatch results in scattering and the structures being visible; but when viewed under an applied electrical potential matching the potential used during polymerization, the polymerized and non-polymerized components match in birefringence, and the structures become indiscernible (**Figure 1.9b**).[40] Alternatively, the birefringence of LC microstructures can also be used to fabricate temperature-responsive color pixels for encryption, encoding, and anticounterfeiting elements at the microscale (**Figure 1.9c**).[124] Another option using the birefringence of LC is making photonic microstructures via DLW-TPP micropatterns[65,125] and scaffolds[126,127] which serve to precisely change the director of the molecules, creating a controlled variation of the refractive index, within the structure. As a result, microlenses that specifically focus right-handed circularly polarized light and defocus left-handed circular polarized light, or *vice versa*,[125] or as polarization-independent phase modulators (**Figures 1.9d**).[127] Birefringence effects in microscale objects are rare and it would be of interest to investigate with LCs as starting point, as LC are well known for their use in LCDs which make use of their birefringence.
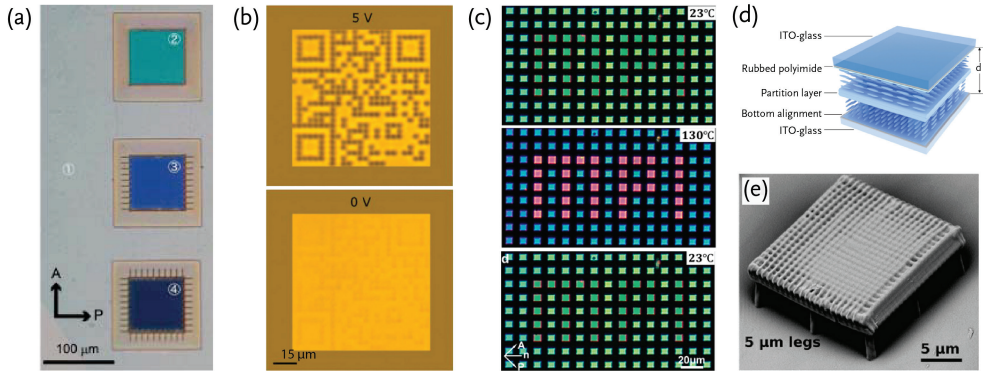
Figure 1.9 (a) Polarized optical micrograph (POM) images of three CLC structures in which the SRB is controlled by introducing indentation in the frames; top without indentations, middle with 20 slits and bottom with 40 slits. Reproduced with permission.[120] Copyright 2008, Optical Society of America. (b) POM images of a quick-response (QR) code formed by micropillars that were polymerized when no electrical potential was applied and consequently the QR code is only visible when a potential is applied. Adapted with permision.[40] Copyright 2018, Wiley-VCH. (c) POM images of arrays of pillars presenting different highs. As a result of the height difference, an encoded message is visible upon heating the structures. Adapted with permision.[124] Copyright 2020, Wiley-VCH. (d) Schematic of a polarization-independent phase modulator that consist a 3D scaffold that align the mesogens in distinctly along the structure. Reproduced with permission.[127] Copyright 2017, Optical Society of America. (e) Scanning electron microscopy image of a light-responsive beam steerer. Reproduced with permission.[118] Copyright 2012, Wiley-VCH.

On the other hand, rather than using the internal material structure itself to interact with light, photonic interactions can be generated by fabricating periodic microstructures. Depending on the scale of the periodicity, the incident beam will be modulated or not. For example, gratings are well-known 2D photonic crystals that diffract incident light. When such a grating is made of a light-responsive LCN with a pitch of 1.5 µm (**Figures 1.9e**), it diffracts red light.[118] Owing to the anisotropic shape change of the LCN, the diffraction pattern could be altered by illuminating the grating with a green laser. The rapid response of the network resulted in the possibility of converting the simple static grating into a beam steerer.[118]

1.5 3D Microextrusion of Liquid Crystals

In extrusion-based equipment, a thread of material known as a "filament" is forced through a nozzle and deposited on a substrate or previously printed layer in a predetermined fashion. Layers are formed line-by-line, and objects layer-by-layer. The resolution, from 100 µm to 1 cm,[1] is

primarily determined by the nozzle diameter and printing speed. Once extruded, the material must be able to maintain its shape. This excludes low viscosity materials and makes thermoplastics and viscoelastic thermoset resists more appropriate for 3D microextrusion equipment.

Among the different extrusion-based equipment, direct ink writing (DIW) printers, **Figure 1.10**, have been predominantly used for 4D printing of LC-based centimeter-scale objects. In short, DIW is suitable for materials that cannot be stored as a solid filament, such as LC oligomers as they are viscoelastic thermosets, and was first intended as a technique to fabricate ceramic objects in complex, three-dimensional shapes.[128] The syringe is loaded with a viscoelastic ink and pressurized mechanically, or pneumatically, and a predefined print path is followed by the printer to write the material in place.[129] Drying or curing of the material can be performed during the print process after each layer is deposited, or after the entire print is completed, depending on the material characteristics.

Direct Ink Writing of Liquid Crystals

Unlike techniques where the resin is in a bath, DIW requires material that does not escape the nozzle under the force of gravity, yet flows well from an extrusion slot under pressure, and shows

LC oligomer ink

heating mantle
typically set to 10 to 20 °C below T_{NI} for obtaining uniaxial nematic alignment

for printing cholesterics: above T_{NI}

printed object
UV-cured per single or double layer

writing speed
higher gives better alignment, 0.5–28 mm s^{-1} reported

layer height
about 75 to 200 µm

nozzle diameter (150–350 µm)
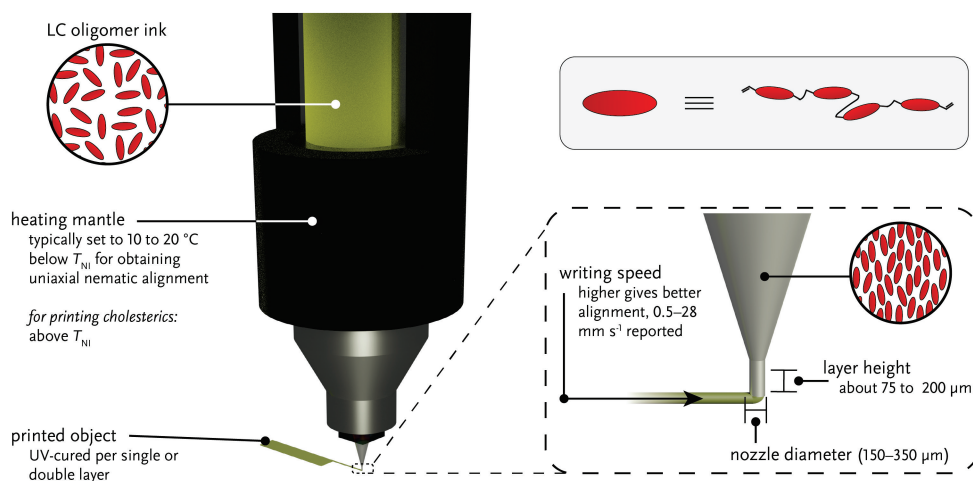
Figure 1.10 Schematic representation of the printing process, detailing the ink reservoir, nozzle, and printed object. The inset shows a detailed schematic representation of the micronozzle indicating the user-adjustable parameters: the writing speed, nozzle diameter, and layer height. The molecular alignment for "LC oligomer ink" and micronozzle shows the approximate orientation of the mesogens in the reservoir, where it is polydomain nematic, and in the high shear environment of the micronozzle, where is it monodomain nematic.

good setting behavior once on the substrate.[130] Such viscoelastic properties are found in LC oligomers, which are the precursors of LCE networks. The last few years of extrusion-based AM of LCs has catapulted one specific class of LCE precursor to the foreground of research: main-chain liquid crystal elastomers (MCLCEs), which are commonly synthesized from oligomers of concatenated reactive mesogens. MCLCEs maintain the anisotropic LC characteristics of the original monomers, but also are viscoelastic; their shear thinning behavior is what makes them useful for DIW. Two similar synthetic methods have found wide appeal for making MCLCEs: amine-acrylate "aza-Michael" and thiol-acrylate "thiol-Michael" addition reactions.[131,132] Both methods have been used extensively for linking diacrylate mesogens with chain extension molecules, the difference between aza-Michael and thiol-Michael being the reactant used for the chain extension. For amine-acrylate, the reaction is between a primary amine and a diacrylate and forms β-aminoester bonds between the reactive mesogens. Thiol-acrylate reactions on the other hand, form β-thioesters. By virtue of the chemistry commonly employed, amine-acrylate or thiol-acrylate, the synthetic procedure for making the LC ink is fast and easily performed. When the diacrylate mesogen is in molar excess over the chain extender, the MCLCE mix obtained is acrylate-terminated and can be photo-crosslinked after addition of a suitable free radical photoinitiator.

In the same manner as LCN, significant research on responsive LCEs that show response to other stimuli than temperature have been reported, however mostly in works not related to 4D printing. Most of the work on DIW of LCs has reported temperature responsive objects; however, response to other stimuli such as light or humidity would be quite appealing. While first reports of DIW printed objects that response to stimuli have been already reported, the cases are still limited and the library of LC inks for DIW remains still limited to a handful of mixtures. Readers interested in learning how to tune an LC ink to obtain centimeter scale object responsive to other stimulus than temperature are directed to literature where different strategies are described.[52]

After loading the ink reservoir with an LC ink composed of MCLCE and a suitable photoinitiator, printing can commence. The key variables that can be adjusted for DIW are printing infill, nozzle diameter, and printing temperature and speed, all of which influence the molecular order obtained after deposition, and thus device functionality and response. Typically, the optimal printing conditions deliver extruded filaments that have a uniaxial alignment parallel to the printing direction,[52] but other type of alignments have also been reported.[47,133] **Figure 1.10** shows schematically the DIW process and its different user-adjustable parameters accompanied with their effects on the printing process; for further explanation, the reader is directed to the literature.[52]

4D Printed Centimeter Scale LC Structures

One of the greatest advantages of DIW of LC is the control that it offers over the mesogenic alignment in the printing direction. Such control over the molecular director within a 3D objects, which determines how the network will respond to an external stimulus, has been explored to obtain actuators displaying different deformation modes including bending, [94,134] lifting, [38,46] and self-propulsion,[34] among others. Objects displaying such actuations can be employed to fabricate soft robots or optical devices, for example. In this section some of these examples, which embody the current state of the art of the field, are presented.

Soft Robots

LCE networks are attractive as artificial muscles as they generally show load-free thermal anisotropic shape changes in the order to 40-50%, [34,36,39,46,67,68,135–137] with actuation stresses in the kPa range at low strains.[68,137] Additionally, typical reported values for the volumetric work capacity of LCE are on the order of 1-40 J kg^{-1}, which is in the same order of magnitude as mammalian skeletal muscle (~8 J kg^{-1}).[138] As a result, lifting a mass vertically against gravity, both triggered by temperature[39,67] or light,[38] has been reported in DIW LCE samples (**Figure 1.11a,b**).

To fabricate an untethered autonomous robot, preprogramed actuation to an external stimulus is imperative. Through engineering the molecular director via DIW in the 3D object, a variety of macroscopic deformations can be preprogramed. Fabricating "+1 point defect" spiral shape causes directional expansion or contraction, upon heating or cooling, respectively, along the mesogenic alignment direction, resulting in an out-of-plane deformation forming cone-like or saddle shapes that can be used to lift weights from below. Bistable architectures can be generated by printing a spiral structure with inner and outer parts having opposite Gaussian curvatures, so heating builds stresses between these two parts that are released as a "snapping" motion, capable of lifting 5× the mass of the actuator.[67] Furthermore, by printing two layers of LCE in orthogonal printing directions, hinges are formed.[139] Strategically placing such hinges in an object in which these are made from different LCEs that respond at different temperatures leads to devices that sequentially respond, *e.g.* folding (**Figure 1.11c**)[34,136] or even displaying self-propulsion.[34] Additionally, control over the porosity of an object can be achieved in a porous woodpile structure that contracts in both length and width with increasing temperature as the structural "beams" increase in diameter, lowering overall porosity.[67]
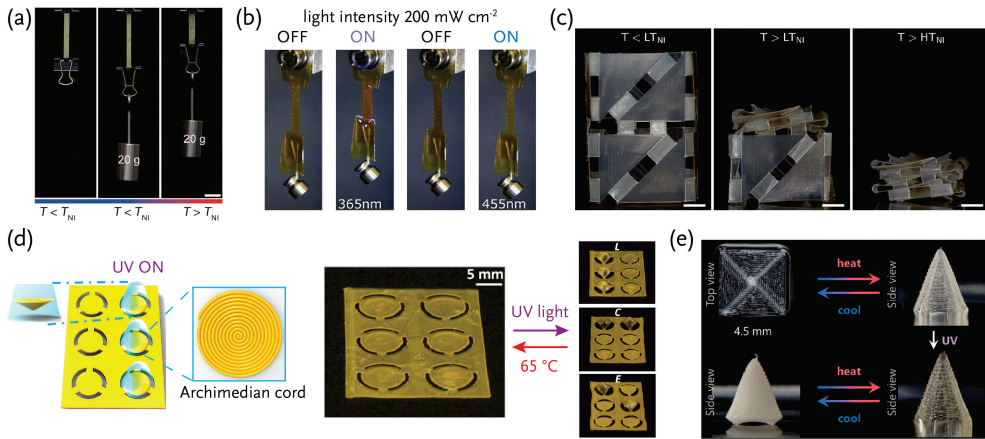
Figure 1.11 (a) Soft actuator showing artificial muscle function. Adapted with permission.[46] Copyright 2018, Wiley-VCH. (b) Light-addressable artificial muscle. Reproduced with permission.[38] Copyright 2020, American Chemical Society. (c) A 4D printed object in which the hinges are made from two different LCE network that result in programmed sequential folding and deformation. Scale bars represent 1 cm. Adapted with permission.[34] Copyright 2019, American Association for the Advancement of Science. (d) Light responsive Braille-like actuator. On the left, an illustration showing the photoswitchable deformation in the pattern. On the right, the actual printed pattern in which the letters "L", "C", and "E" can be written in Braille code by locally triggering certain parts with light. Temperature is used to erase the deformations. Adapted with permission.[142] Copyright 2020, Wiley-VCH (e) Print containing a +1 point defect that pops out into a cone upon heating, and can be permanently fixed in this shape using pendant photoreactive groups. Reproduced with permission.[36] Copyright 2019, Wiley-VCH.

Incorporation of photoswitches, such as azobenzene, in the oligomer chain makes the contraction light-addressable,[38,134,140–142] offering more versatility than only temperature to control the actuation. Light triggers contraction along the alignment direction of the LCE typically leads to a bending motion towards the light source; as the excitation light for the azobenzene is gradually attenuated, a concentration difference in the *cis-* and *trans-*isomers forms through the depth of the film, and thus a gradient in contraction.[38,134,142] As light can be locally applied, a dynamic Braille pattern has been developed (**Figure 1.11d**). Furthermore, light can also be induce reprograming of the deformation post fabrication in reconfigurable LCE.[36] For example, a spiral pattern that forms a cone shaped object upon heating can be fixed by UV light induced polymerization of free vinyl groups that cause network rearrangement (**Figure 1.11e**). More recently, a 4D printed LCE object that responds to light and humidity has also been demonstrated, showing the appealing of combining response to multiple stimuli in a single device.[94]
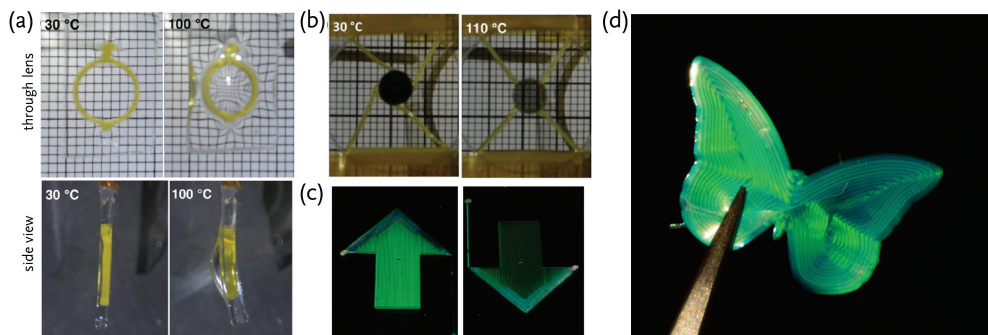
Figure 1.12 (a) LCE-PDMS composite structure. The LCE is printed in a ring that effectively is a section of a +1 point defect. With increased temperature, the ring diameter diminishes, pushing out PDMS bound to it. This is seen in the side view. The transparent PDMS acts as optical element of varying focal point distance depending on its curvature. (b) Chiral architecture in which a small linear polarization filter is rotated to reveal the image behind it. (c) Reflective optical element, the appearance of which was encoded by direct ink writing at high nozzle speed. Depending on the perspective of the viewer with respect to the object, it is either bright green, or very weakly colored. (d) Free-form reflective optical element that was direct ink written at low nozzle speed. After release from the substrate, a self-supporting photonic object is obtained. (a) Adapted and (b) reproduced with permission.[39] Copyright 2017, Wiley-VCH. (c) and (d) were adapted under the terms of the Creative Commons CC BY license.[133] Copyright 2021, Wiley-VCH.

Optical Devices

Contrasting the widespread use of LCs in optical engineering, centimeter-scale printing of LC optics has only rarely been demonstrated. For example, an adjustable lens was made by combining a printed ring of thermally-responsive LCE in a static, compliant PDMS slab.[39] By designing the infill to follow a concentric pattern, heating the composite causes in-plane ring shrinkage, pushing out the clear PDMS, resulting in temperature-sensitive light refraction (**Figure 1.12a**). In another example, a responsive linear polarization filter was demonstrated by printing a chiral holder, in which the center element rotates as the outward spanning fibers contract.[39] This contraction rotates a small linear polarizer placed in the holder, which, when coupled with a second, static polarization filter, forms a thermally addressable, variable transmission element (**Figure 1.12b**).

Direct printing of a structurally colored material was achieved recently using a chiral nematic LC ink from the isotropic phase onto a heated print bed at low printing speeds (~ 1-2 mm s^{-1}, **Figure 1.12d**),[133] making it possible to print objects with optical behavior similar to chiral nematic films fabricated in specialized LC alignment devices.[28] By printing at greater speeds (~8-10 mm s^{-1}), the normal helical alignment of the chiral nematic was distorted, forming

anisotropic reflectors (**Figure 1.12c**). Combining varying print paths and speeds, it is possible to write optical elements with highly perspective-dependent appearances.[133] Consequently, the reflected polarization state can be controlled through the print parameters, as the distorted helical alignment does not discriminate between left- and right-circular polarized light at normal incidence, unlike conventional chiral nematic reflectors or those printed at lower speeds which are exclusively selective to either right- or left-circular polarizations at normal incidence.

1.6 Research Aim and Thesis Outline

In recent years, additive manufacturing of liquid crystal materials has attracted rapidly growing interest from the scientific community. **Chapter 1** has offered the reader an introduction to 4D printing of liquid crystals utilizing, basically, two different AM techniques: direct laser writing by two-photon polymerization and direct ink writing for the fabrication of responsive micrometer and centimeter scale objects, respectively. The examples discussed embody the potential and versatility of 4D printing LCs for fabricating numerous functional structures across different length scales. While significant progress has been made, there still remain several aspects to be addressed to unleash the full potential of this process. This thesis focuses on expanding the library of liquid crystal precursors suitable to use both in DLW-TPP and in DIW equipment with the aim of fabricating, 4D functional materials and devices.

First, we tackle on the fabrication of micro-actuators, which has been mainly accomplished by direct laser writing by two-photon polymerization of stimuli-responsive materials. This technique has one main challenge: the swelling of the polymerized network by unreacted monomers which reduces the resolution of the micro-object. This arises from the fact that this class of materials are based on low crosslink density networks. **Chapter 2** reports a new LC photoresist suitable for DLW-TPP that results in a highly crosslink networks that overcomes such obstacle. A series of 3D micro-actuators are fabricated that show reversible anisotropic shape and unique polarization coloration changes triggered by temperature. The results demonstrate that, while limited in magnitude (up to 26%), appealing actuation in LCN structures can be accomplished. **Chapter 3** presents a novel approach to fabricated photonic micro-actuators that show large shape deformations by incorporating into a LC photonic-photoresist supramolecular hydrogen bonded mesogens. These mesogens act as physical crosslink points during the DLW-TPP process that minimize the network swelling, facilitating sub-micron resolution. The supramolecular bonds can be cleaved, resulting in large humidity-triggered expansions (up to 42%). The photonic character is

obtained by employing a cholesteric alignment, which results in a built-in color sensor for a real time identification of the structures' status.

Secondly, the focus is put on the fabrication of centimeter sized 4D objects, which have been predominantly fabricated via direct ink writing. DIW of LC permits a great degree of control over the molecular director in all directions in 3D centimeter scale objects, a control that is hard to achieve with other techniques. Light as a stimulus is appealing for untethered 4D materials and devices as it can be rapidly and locally applied, however few attention to develop LC ink that respond to this stimulus has been made. To this end, in **Chapter 4** a LC ink suitable for DIW that result in a light-responsive network is developed. Interestingly the light-induced bending motion of the fabricated film shows a temperature-controlled directionality. As a result, the network shows three different deformations modes, bending in opposite direction in additions to anisotropic shape changes, by carefully combining light and temperature. The potential use of this ink to fabricate multi-functional devices is explored in **Chapter 5** by producing partially covered bilayer actuators via DIW. Surprisingly, the partial coverage of the passive layer does not significantly hinder the performance of the films and, in some cases, it can even improve it. By making use of the precise depositions of the LC material via DIW, discrete regions are created that can be triggered individually, resulting in twisting and bending in perpendicular directions by sequentially triggering the different regions and by combining light and temperature. Additionally, the partial coverage facilitates the combination of different materials in one device, such as photonic rubber, that brings multi-functional actuators one-step-closer to realization.

Finally, **Chapter 6** puts in context the future implications of the advances presented in this thesis. In addition, the current challenges of DLW-TPP and DIW of LC are addressed and future opportunities examined. The discussion offers a "roadmap" for the field of 4D printing of LC, across different lengths scale, for the realization of multi-functional, untethered devices and their future widespread use; from the perspective of material development, device's design, and additive manufacturing equipment.

1.7 References

1 S. C. Ligon, R. Liska, J. Stampfl, M. Gurr and R. Mülhaupt, *Chem. Rev.*, 2017, **117**, 10212–10290.
2 F. Bos, R. Wolfs, Z. Ahmed and T. Salet, *Virtual Phys. Prototyp.*, 2016, **11**, 209–225.
3 A. J. Gross and K. Bertoldi, *Small*, 2019, **15**, 1902370.
4 H. Klippstein, A. Diaz De Cerio Sanchez, H. Hassanin, Y. Zweiri and L. Seneviratne, *Adv. Eng. Mater.*, 2018, **20**, 1700552.
5 F. Froes and R. Boyer, Eds., *Additive Manufacturing for the Aerospace Industry*, Elsevier, 2019.
6 D. J. Wu, C. V. C. Bouten and P. Y. W. Dankers, *Curr. Opin. Biomed. Eng.*, 2017, **2**, 43–48.
7 S. Ostrovidov, S. Salehi, M. Costantini, K. Suthiwanich, M. Ebrahimi, R. B. Sadeghian, T. Fujie, X. Shi, S. Cannata, C. Gargioli, A. Tamayol, M. R. Dokmeci, G. Orive, W. Swieszkowski and A. Khademhosseini, *Small*, 2019, **15**, 1805530.
8 S. V. Murphy and A. Atala, *Nat. Biotechnol.*, 2014, **32**, 773–785.
9 R. Karyappa and M. Hashimoto, *Sci. Rep.*, 2019, **9**, 14178.
10 J. I. Lipton, M. Cutler, F. Nigl, D. Cohen and H. Lipson, *Trends Food Sci. Technol.*, 2015, **43**, 114–123.
11 M. Moini, J. Olek, J. P. Youngblood, B. Magee and P. D. Zavattieri, *Adv. Mater.*, 2018, **30**, 1802123.
12 A. Paolini, S. Kollmannsberger and E. Rank, *Addit. Manuf.*, 2019, **30**, 100894.
13 J. S. Lee, *J. Fash. Bus.*, 2020, **24**, 130–143.
14 M. R. Hartings and Z. Ahmed, *Nat. Rev. Chem.*, 2019, **3**, 305–314.
15 F. Kotz, P. Risch, D. Helmer and B. E. Rapp, *Adv. Mater.*, 2019, **31**, 1805982.
16 M. R. Chowdhury, J. Steffes, B. D. Huey and J. R. McCutcheon, *Science (80-.)*, 2018, **361**, 682–686.
17 S. H. Park, R. Su, J. Jeong, S.-Z. Guo, K. Qiu, D. Joung, F. Meng and M. C. McAlpine, *Adv. Mater.*, 2018, **30**, 1803980.
18 S.-Z. Guo, K. Qiu, F. Meng, S. H. Park and M. C. McAlpine, *Adv. Mater.*, 2017, **29**, 1701218.
19 X.-Q. Wang, K. H. Chan, Y. Cheng, T. Ding, T. Li, S. Achavananthadith, S. Ahmet, J. S. Ho and G. W. Ho, *Adv. Mater.*, 2020, **32**, 2000351.
20 M. Sitti, *Nat. Rev. Mater.*, 2018, **3**, 74–75.
21 D. Rus and M. T. Tolley, *Nature*, 2015, **521**, 467–475.
22 J. del Barrio and C. Sánchez‑Somolinos, *Adv. Opt. Mater.*, 2019, **7**, 1900598.
23 C. A. Spiegel, M. Hippler, A. Münchinger, M. Bastmeyer, C. Barner‑Kowollik, M. Wegener and E. Blasco, *Adv. Funct. Mater.*, 2020, **30**, 1907615.
24 D. J. Broer, C. W. M. Bastiaansen, M. G. Debije and A. P. H. J. Schenning, *Angew. Chemie Int. Ed.*, 2012, **51**, 7102–7109.
25 J. M. McCracken, B. R. Donovan and T. J. White, *Adv. Mater.*, 2020, **32**, 1906564.
26 M. Pilz da Cunha, M. G. Debije and A. P. H. J. Schenning, *Chem. Soc. Rev.*, 2020, **49**, 6568–6578.
27 T. J. White, M. E. McConney and T. J. Bunning, *J. Mater. Chem.*, 2010, **20**, 9832.
28 D. J. Mulder, A. P. H. J. Schenning and C. W. M. Bastiaansen, *J. Mater. Chem. C*, 2014, **2**, 6695–6705.
29 T. J. White and D. J. Broer, *Nat. Mater.*, 2015, **14**, 1087–1098.
30 J. A. H. P. Sol, G. H. Timmermans, A. J. van Breugel, A. P. H. J. Schenning and M. G. Debije, *Adv. Energy Mater.*, 2018, **8**, 1702922.
31 F. L. L. Visschers, M. Hendrikx, Y. Zhan and D. Liu, *Soft Matter*, 2018, **14**, 4898–4912.
32 C. L. Gonzalez, C. W. M. Bastiaansen, J. Lub, J. Loos, K. Lu, H. J. Wondergem and D. J. Broer, *Adv. Mater.*, 2008, **20**, 1246–1252.
33 H. Zeng, P. Wasylczyk, C. Parmeggiani, D. Martella, M. Burresi and D. S. Wiersma, *Adv. Mater.*, 2015, **27**, 3883–3887.
34 A. Kotikian, C. McMahan, E. C. Davidson, J. M. Muhammad, R. D. Weeks, C. Daraio and J. A. Lewis, *Sci. Robot.*, 2019, **4**, eaax7044.
35 H. Yoshida, C. H. Lee, Y. Matsuhisa, A. Fujii and M. Ozaki, *Adv. Mater.*, 2007, **19**, 1187–1190.
36 E. C. Davidson, A. Kotikian, S. Li, J. Aizenberg and J. A. Lewis, *Adv. Mater.*, 2020, **32**, 1905682.
37 M. del Pozo, C. Delaney, C. W. M. Bastiaansen, D. Diamond, A. P. H. J. Schenning and L. Florea, *ACS Nano*, 2020, **14**, 9832–9839.
38 L. Ceamanos, Z. Kahveci, M. López‑Valdeolivas, D. Liu, D. J. Broer and C. Sánchez‑Somolinos, *ACS Appl. Mater. Interfaces*, 2020, **12**, 44195–44204.
39 M. López‑Valdeolivas, D. Liu, D. J. Broer and C. Sánchez‑Somolinos, *Macromol. Rapid Commun.*, 2018, **39**, 1700710.
40 C. C. Tartan, J. J. Sandford O'Neill, P. S. Salter, J. Aplinc, M. J. Booth, M. Ravnik, S. M. Morris and S. J. Elston, *Adv. Opt. Mater.*, 2018, **6**, 1800515.
41 Y. Guo, H. Shahsavan and M. Sitti, *Adv. Mater.*, 2020, **32**, 2002753.

42   M. Javed, S. Tasmim, M. K. Abdelrahman, C. P. Ambulo and T. H. Ware, *Crystals*, 2020, **10**, 420.

43   R. H. Volpe, D. Mistry, V. V. Patel, R. R. Patel and C. M. Yakacki, *Adv. Healthc. Mater.*, 2020, **9**, 1901136.

44   US4575330A, *US Pat. 4,575,330A*, 1986, 1–16.

45   US5121329, 1989.

46   A. Kotikian, R. L. Truby, J. W. Boley, T. J. White and J. A. Lewis, *Adv. Mater.*, 2018, **30**, 1706164.

47   C. Zhang, X. Lu, G. Fei, Z. Wang, H. Xia and Y. Zhao, *ACS Appl. Mater. Interfaces*, 2019, **11**, 44774–44782.

48   M. Tabrizi, T. H. Ware and M. R. Shankar, *ACS Appl. Mater. Interfaces*, 2019, **11**, 28236–28245.

49   S. Gantenbein, K. Masania, W. Woigk, J. P. W. Sesseg, T. A. Tervoort and A. R. Studart, *Nature*, 2018, **561**, 226–230.

50   L. Chen, Y. Dong, C.-Y. Tang, L. Zhong, W.-C. Law, G. C. P. Tsui, Y. Yang and X. Xie, *ACS Appl. Mater. Interfaces*, 2019, **11**, 19541–19553.

51   D. Martella, S. Nocentini, D. Nuzhdin, C. Parmeggiani and D. S. Wiersma, *Adv. Mater.*, 2017, **29**, 1704047.

52   M. del Pozo, J. A. H. P. Sol, A. P. H. J. Schenning and M. G. Debije, *Adv. Mater.*, 2021, 2104390.

53   J. Planer, *Justus Liebigs Ann. Chem.*, 1861, **118**, 25–27.

54   F. Reinitzer, *Monatshefte für Chemie*, 1888, **9**, 421–441.

55   O. Lehmann, *Zeitschrift für Phys. Chemie*, 1889, **4**, 462–472.

56   G. W. Gray, K. J. Harrison and J. A. Nash, *Electron. Lett.*, 1973, **9**, 130.

57   G. H. Brown and W. G. Shaw, *Chem. Rev.*, 1957, **57**, 1049–1157.

58   O. Francescangeli, F. Vita and E. T. Samulski, *Soft Matter*, 2014, **10**, 7685–7691.

59   D. Liu and D. J. Broer, *Langmuir*, 2014, **30**, 13499–13509.

60   T. J. White, *J. Polym. Sci. Part B Polym. Phys.*, 2018, **56**, 695–705.

61   A. J. Leadbetter and P. G. Wrighton, *Le J. Phys. Colloq.*, 1979, **40**, C3-234-C3-242.

62   P. P. C. Verbunt, T. M. de Jong, D. K. G. de Boer, D. J. Broer and M. G. Debije, *Eur. Phys. J. Appl. Phys.*, 2014, **67**, 10201.

63   D. M. Agra-Kooijman, M. R. Fisch and S. Kumar, *Liq. Cryst.*, 2018, **45**, 680–686.

64   Y. Zhan, A. P. H. J. Schenning, D. J. Broer, G. Zhou and D. Liu, *Adv. Funct. Mater.*, 2018, **28**, 1707436.

65   H. Zeng, P. Wasylczyk, G. Cerretti, D. Martella, C. Parmeggiani and D. S. Wiersma, *Appl. Phys. Lett.*, 2015, **106**, 111902.

66   D. J. Broer, *Adv. Mater.*, 2020, **32**, 1905144.

67   C. P. Ambulo, J. J. Burroughs, J. M. Boothby, H. Kim, M. R. Shankar and T. H. Ware, *ACS Appl. Mater. Interfaces*, 2017, **9**, 37332–37339.

68   D. J. Roach, X. Kuang, C. Yuan, K. Chen and H. J. Qi, *Smart Mater. Struct.*, 2018, **27**, 125011.

69   P. G. de Gennes, *Comptes Rendus l'Académie des Sci. Paris B*, 1975, **281**, 101–103.

70   D. J. Broer and G. N. Mol, *Polym. Eng. Sci.*, 1991, **31**, 625–631.

71   L. T. de Haan, J. M. N. Verjans, D. J. Broer, C. W. M. Bastiaansen and A. P. H. J. Schenning, *J. Am. Chem. Soc.*, 2014, **136**, 10585–10588.

72   F. Mondiot, X. Wang, J. J. de Pablo and N. L. Abbott, *J. Am. Chem. Soc.*, 2013, **135**, 9972–9975.

73   V. S. R. Jampani, R. H. Volpe, K. Reguengo de Sousa, J. Ferreira Machado, C. M. Yakacki and J. P. F. Lagerwall, *Sci. Adv.*, 2019, **5**, eaaw2476.

74   L. B. Braun, T. Hessberger and R. Zentel, *J. Mater. Chem. C*, 2016, **4**, 8670–8678.

75   C. Ohm, C. Serra and R. Zentel, *Adv. Mater.*, 2009, **21**, 4859–4862.

76   X. Liu, M. G. Debije, J. P. A. Heuts and A. P. H. J. Schenning, *Chem. – A Eur. J.*, 2021, **27**, 14168–14178.

77   L. T. de Haan, V. Gimenez-Pinto, A. Konya, T.-S. Nguyen, J. M. N. Verjans, C. Sánchez-Somolinos, J. V. Selinger, R. L. B. Selinger, D. J. Broer and A. P. H. J. Schenning, *Adv. Funct. Mater.*, 2014, **24**, 1251–1258.

78   C. D. Modes and M. Warner, *Phys. Rev. E*, 2011, **84**, 021711.

79   L. T. de Haan, C. Sánchez-Somolinos, C. W. M. Bastiaansen, A. P. H. J. Schenning and D. J. Broer, *Angew. Chemie - Int. Ed.*, 2012, **51**, 12469–12472.

80   T. H. Ware, M. E. McConney, J. J. Wie, V. P. Tondiglia and T. J. White, *Science (80-.)*, 2015, **347**, 982–984.

81   S. Ahn, T. H. Ware, K. M. Lee, V. P. Tondiglia and T. J. White, *Adv. Funct. Mater.*, 2016, **26**, 5819–5826.

82   S. J. Aßhoff, F. Lancia, S. Iamsaard, B. Matt, T. Kudernac, S. P. Fletcher and N. Katsonis, *Angew. Chemie Int. Ed.*, 2017, **56**, 3261–3265.

83   J. A. H. P. Sol, A. R. Peeketi, N. Vyas, A. P. H. J. Schenning, R. K. Annabattula and M. G. Debije, *Chem. Commun.*, 2019, **55**, 1726–1729.

84   O. M. Wani, H. Zeng and A. Priimagi, *Nat. Commun.*, 2017, **8**, 15546.

85   O. M. Wani, R. Verpaalen, H. Zeng, A. Priimagi and A. P. H. J. Schenning, *Adv. Mater.*, 2019, **31**, 1805985.

86   M. Pilz da Cunha, S. Ambergen, M. G. Debije, E. F. G. A. Homburg, J. M. J. den Toonder and A. P. H. J. Schenning, *Adv. Sci.*, 2020, **7**, 1902842.

87   M. Pilz da Cunha, H. S. Kandail, J. M. J. den Toonder and A. P. H. J. Schenning, *Proc. Natl. Acad. Sci.*, 2020, **117**,

17571-17577.

88 C. D. Modes, M. Warner, C. Sánchez-Somolinos, L. T. de Haan and D. Broer, *Proc. R. Soc. A Math. Phys. Eng. Sci.*, 2013, **469**, 20120631.

89 S. Timoshenko, *J. Opt. Soc. Am.*, 1925, **11**, 233.

90 J. M. Boothby and T. H. Ware, *Soft Matter*, 2017, **13**, 4349–4356.

91 H. K. Bisoyi and Q. Li, *Chem. Rev.*, 2016, **116**, 15089–15166.

92 M. Pilz da Cunha, E. A. J. van Thoor, M. G. Debije, D. J. Broer and A. P. H. J. Schenning, *J. Mater. Chem. C*, 2019, **7**, 13502–13509.

93 A. H. Torbati and P. T. Mather, *J. Polym. Sci. Part B Polym. Phys.*, 2016, **54**, 38–52.

94 K. Kim, Y. Guo, J. Bae, S. Choi, H. Y. Song, S. Park, K. Hyun and S. Ahn, *Small*, 2021, **17**, 2100910.

95 M. J. Ford, C. P. Ambulo, T. A. Kent, E. J. Markvicka, C. Pan, J. Malen, T. H. Ware and C. Majidi, *Proc. Natl. Acad. Sci.*, 2019, **116**, 21438–21444.

96 M. J. Ford, M. Palaniswamy, C. P. Ambulo, T. H. Ware and C. Majidi, *Soft Matter*, 2020, **16**, 5878–5885.

97 C. P. Ambulo, M. J. Ford, K. Searles, C. Majidi and T. H. Ware, *ACS Appl. Mater. Interfaces*, 2021, **13**, 12805–12813.

98 M. Pilz da Cunha, Y. Foelen, T. A. P. Engels, K. Papamichou, M. Hagenbeek, M. G. Debije and A. P. H. J. Schenning, *Adv. Opt. Mater.*, 2019, **7**, 1801604.

99 M. Pilz da Cunha, Y. Foelen, R. J. H. Raak, J. N. Murphy, T. A. P. Engels, M. G. Debije and A. P. H. J. Schenning, *Adv. Opt. Mater.*, 2019, **7**, 1801643.

100 H. Ding, Q. Zhang, H. Gu, X. Liu, L. Sun, M. Gu and Z. Gu, *Adv. Funct. Mater.*, 2020, **30**, 1901760.

101 H. Xia, J. Wang, Y. Tian, Q.-D. Chen, X.-B. Du, Y.-L. Zhang, Y. He and H.-B. Sun, *Adv. Mater.*, 2010, **22**, 3204–3207.

102 R. K. K. Jayne, T. J. J. Stark, J. B. B. Reeves, D. J. J. Bishop and A. E. E. White, *Adv. Mater. Technol.*, 2018, **3**, 1–6.

103 J. K. K. Gansel, M. Thiel, M. S. S. Rill, M. Decker, K. Bade, V. Saile, G. Von Freymann, S. Linden and M. Wegener, *Science (80-.).*, 2009, **325**, 1513–1515.

104 K. Sugioka, J. Xu, D. Wu, Y. Hanada, Z. Wang, Y. Cheng and K. Midorikawa, *Lab Chip*, 2014, **14**, 3447–3458.

105 Z. He, Y.-H. Lee, D. Chanda and S.-T. Wu, *Opt. Express*, 2018, **26**, 21184.

106 M. Rumi, S. Barlow, J. Wang, J. W. Perry and S. R. Marder, *Adv. Polym. Sci.*, 2008, 213, 1–95.

107 X. Zhou, Y. Hou and J. Lin, *AIP Adv.*, 2015, **5**, 30701.

108 R. J. DeVoe, H. W. Kalweit, C. A. Leatherdale and T. R. Williams, in *Multiphoton Absorption and Nonlinear Transmission Processes: Materials, Theory, and Applications*, SPIE, 2003, **4797**, 310.

109 Y. L. Zhang, Q. D. Chen, H. Xia and H. B. Sun, *Nano Today*, 2010, **5**, 435–448.

110 A. Selimis, V. Mironov and M. Farsari, *Microelectron. Eng.*, 2014, **132**, 83–89.

111 J. M. McCracken, V. P. Tondiglia, A. D. Auguste, N. P. Godman, B. R. Donovan, B. N. Bagnall, H. E. Fowler, C. M. Baxter, V. Matavulj, J. D. Berrigan and T. J. White, *Adv. Funct. Mater.*, 2019, **29**, 1903761.

112 I. De Bellis, S. Nocentini, M. G. Delli Santi, D. Martella, C. Parmeggiani, S. Zanotto and D. S. Wiersma, *Laser Photon. Rev.*, 2021, **15**, 2100090.

113 H. Zeng, D. Martella, P. Wasylczyk, G. Cerretti, J.-C. C. G. Lavocat, C.-H. H. Ho, C. Parmeggiani and D. S. Wiersma, *Adv. Mater.*, 2014, **26**, 2319–2322.

114 S. Nocentini, D. Martella, C. Parmeggiani and D. Wiersma, *Materials (Basel).*, 2016, **9**, 525.

115 A. Tudor, C. Delaney, H. Zhang, A. J. Thompson, V. F. Curto, G. Z. Yang, M. J. Higgins, D. Diamond and L. Florea, *Mater. Today*, 2018, **21**, 807–816.

116 D. C. Hoekstra, A. P. H. J. Schenning and M. G. Debije, *Soft Matter*, 2020, **16**, 5106–5119.

117 D. Martella, D. Antonioli, S. Nocentini, D. S. Wiersma, G. Galli, M. Laus and C. Parmeggiani, *RSC Adv.*, 2017, **7**, 19940–19947.

118 S. Nocentini, D. Martella, C. Parmeggiani, S. Zanotto and D. S. Wiersma, *Adv. Opt. Mater.*, 2018, **6**, 1800167.

119 H. Yoshida, C. H. Lee, A. Fujii and M. Ozaki, *Appl. Phys. Lett.*, 2006, **89**, 231913.

120 H. Yoshida, Y. Miura, K. Tokuoka, S. Suzuki, A. Fujii and M. Ozaki, *Opt. Express*, 2008, **16**, 19034.

121 C. C. Tartan, P. S. Salter, M. J. Booth, S. M. Morris and S. J. Elston, *J. Appl. Phys.*, 2016, **119**, 183106.

122 C. C. Tartan, P. S. Salter, T. D. Wilkinson, M. J. Booth, S. M. Morris and S. J. Elston, *RSC Adv.*, 2017, **7**, 507–511.

123 J. J. Sandford O'Neill, P. S. Salter, M. J. Booth, S. J. Elston and S. M. Morris, *Nat. Commun.*, 2020, **11**, 2203.

124 Y. Guo, H. Shahsavan and M. Sitti, *Adv. Opt. Mater.*, 2020, **8**, 1902098.

125 Z. He, G. Tan, D. Chanda and S.-T. Wu, *Opt. Express*, 2019, **27**, 11472.

126 M. Fleisch, S. Gao, D. Bošnjaković, X. Zhang, R. A. A. Rupp and I. Drevenšek-Olenik, *Liq. Cryst.*, 2019, **46**, 1–10.

127 Z. He, Y.-H. Lee, F. Gou, D. Franklin, D. Chanda and S.-T. Wu, *Opt. Express*, 2017, **25**, 33688.

128 J. Cesarano Ⅲ, R. Segalman and P. Calvert, *Ceram. Ind.*, 1998, 94.

129 J. A. Lewis, *Adv. Funct. Mater.*, 2006, **16**, 2193–2204.

130 L. Li, Q. Lin, M. Tang, A. J. E. Duncan and C. Ke, *Chem. – A Eur. J.*, 2019, **25**, 10768–10781.

131 T. H. Ware and T. J. White, *Polym. Chem.*, 2015, **6**, 4835–4844.

132 C. M. Yakacki, M. Saed, D. P. Nair, T. Gong, S. M. Reed and C. N. Bowman, *RSC Adv.*, 2015, **5**, 18997–19001.

133 J. A. H. P. Sol, H. Sentjens, L. Yang, N. Grossiord, A. P. H. J. Schenning and M. G. Debije, *Adv. Mater.*, 2021, **33**, 2103309.

134 M. del Pozo, L. Liu, M. Pilz da Cunha, D. J. Broer and A. P. H. J. Schenning, *Adv. Funct. Mater.*, 2020, **30**, 2005560.

135 C. Yuan, D. J. Roach, C. K. Dunn, Q. Mu, X. Kuang, C. M. Yakacki, T. J. Wang, K. Yu and H. J. Qi, *Soft Matter*, 2017, **13**, 5558–5568.

136 M. O. Saed, C. P. Ambulo, H. Kim, R. De, V. Raval, K. Searles, D. A. Siddiqui, J. M. O. Cue, M. C. Stefan, M. R. Shankar and T. H. Ware, *Adv. Funct. Mater.*, 2019, **29**, 1806412.

137 D. J. Roach, C. Yuan, X. Kuang, V. C.-F. Li, P. Blake, M. L. Romero, I. Hammel, K. Yu and H. J. Qi, *ACS Appl. Mater. Interfaces*, 2019, **11**, 19514–19521.

138 J. D. W. Madden, N. A. Vandesteeg, P. A. Anquetil, P. G. A. Madden, A. Takshi, R. Z. Pytel, S. R. Lafontaine, P. A. Wieringa and I. W. Hunter, *IEEE J. Ocean. Eng.*, 2004, **29**, 706–728.

139 L. L. Ren, B. Li, Y. He, Z. Song, X. Zhou, Q. Liu and L. L. Ren, *ACS Appl. Mater. Interfaces*, 2020, **12**, 15562–15572.

140 L. Liu, M. del Pozo, F. Mohseninejad, M. G. Debije, D. J. Broer and A. P. H. J. Schenning, *Adv. Opt. Mater.*, 2020, **8**, 2000732.

141 A. H. Gelebart, M. K. McBride, A. P. H. J. Schenning, C. N. Bowman and D. J. Broer, *Adv. Funct. Mater.*, 2016, **26**, 5322–5327.

142 X. Lu, C. P. Ambulo, S. Wang, L. K. Rivera-Tarazona, H. Kim, K. Searles and T. H. Ware, *Angew. Chemie Int. Ed.*, 2021, **60**, 5536–5543.

Chapter 2

Direct Laser Writing of Temperature-Responsive Highly Crosslinked Micro-Actuator
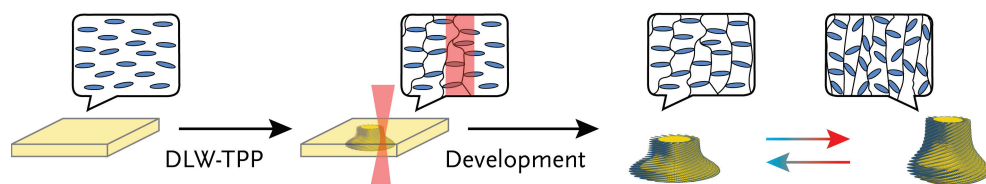
Abstract

Over the past decade, progress in direct laser writing by two-photon polymerization of stimuli-responsive materials has made considerable inroads into the realization of micro-actuators. With the focus on performing complex tasks such as walking, grasping, or delivering drugs, these actuators require a controlled pre-programmed actuation. Liquid crystalline enable such pro-grammed movement when the mesogenic alignment can be successfully controlled. To date, this has necessitated low crosslink density networks, which are not readily conducive to the fabrication of 3D geometries. This chapter reports a liquid crystalline-based photoresist that results in a highly crosslinked network that permits fabrication of 4D micro-actuators in which the molecular alignment is determined by the alignment layers in the cell construct.

2.1 Introduction

Additive manufacturing of stimuli-responsive materials has found exciting application in the generation of micro-actuators. [1–14] Direct laser writing by two-photon polymerization (DLW-TPP), in particular, has proven suitable for inducing locally selective polymerization in various stimuli-responsive materials.[7,10,13–19] This technique offers outstanding resolution and a high degree of freedom in structural design,[13,20,21] which has been used to generate micro-actuators which can perform advanced tasks such as walking, grasping, swimming, and delivering drugs among others.[10,12,14,15,17,22–24] Among the available stimuli-responsive materials, liquid crystals (LC) have attracted special attention for the fabrication of micro-actuators via DLW-TPP as they can deliver rapid, reversible, pre-programmed anisotropic shape deformations in both dry and wet environments. [10,12,17,18,23,25–30] In an LC-based micro-actuator, control over the mesogenic alignment is key to pre-programming the actuation of the microstructure.[31–33] To truly exploit the potential of highly functional 3D liquid crystalline micro-actuators, we must first improve our understanding of the effect fabrication method and structure geometry play in mesogens alignment, and consequently, in actuator response.

This chapter reports a LC photoresist suitable for DLW-TPP fabrication of temperature responsive 4D micro-actuators with a highly crosslinked network. A series of uniaxially aligned 3D structures is presented which demonstrates that mesogenic alignment is dictated by the alignment layer in the cell construct and not by the DLW-TPP parameters, allowing fabrication of microstructures with pre-programmed shape changes. Furthermore, owed to monolithic alignment, a characteristic and unique polarization color is observed that can be used to identify and differentiate the structures. The fabricated 3D microstructures are responsive to temperature variations which trigger anisotropic shape changes of different amplitudes, depending on the structure's geometry. Full structural and optical characterizations of the 3D constructs at different temperatures are presented. The results embody the advantages and limitations of using densely crosslinked liquid crystalline networks (LCN) to fabricate micro-actuators via DLW-TPP.

2.2 Results and Discussion

Liquid Crystal Photoresist

The LC photoresist used in this work consists of two classes of reactive mesogens: **1-3** are difunctional mesogenic acrylates (58.4 mol%) acting as crosslinkers, and **4** is a monofunctional mesogenic acrylate (40.0 mol%) that brings flexibility to the network, **Figure 2.1a**. This LC mixture has
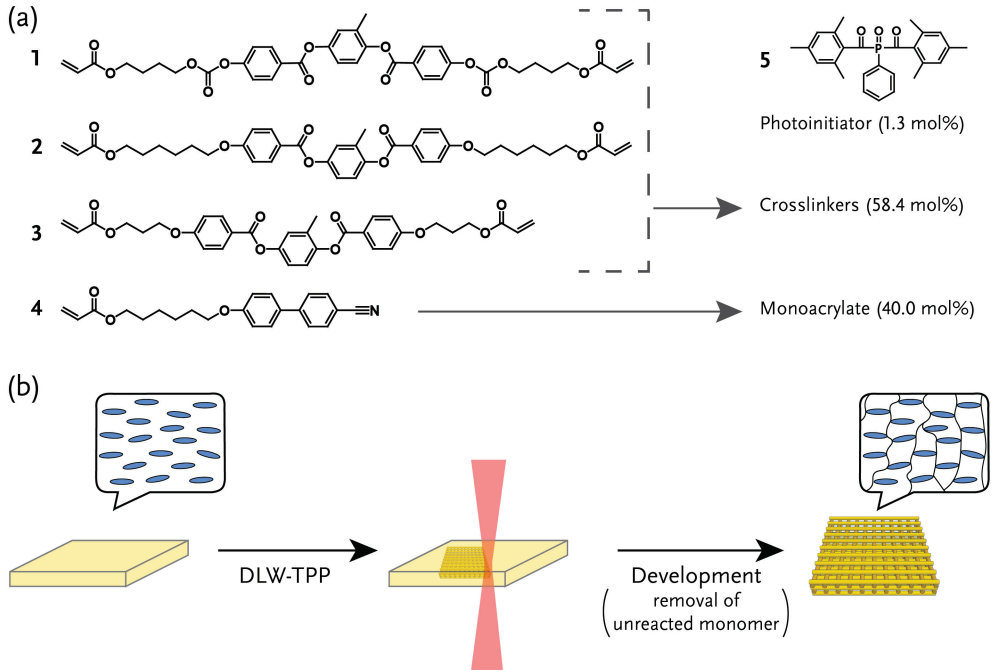
Figure 2.1 (a) Overview of reactive mesogens and photoinitiator used to prepare the LC-photoresist. (b) Schematic representation of the fabrication process for temperature responsive uniaxially aligned 3D microstructures. The blue rods represent the mesogens, which align along the longitudinal axis of the cell construct.

an isotropic to nematic temperature ($T_{I/N}$) at ~100 °C with the nematic LC phase at room temperature without any signs of crystallization after at least 8h.[34] To enable two-photon polymerization (TPP), 1.3 mol% of **5**, a photoinitiator, was added. The photoinitiator chosen has been employed previously to induce DLW-TPP in acrylate-based resists.[17,24,35–37]

By fabricating a polymer film using the LC-photoresist, the glass transition temperature (T_g) of the material was found to be ~69 °C and its degradation temperature ($T_{degradation}$) ~363 °C.[34] Above T_g, the network is in its softer, rubbery state,[38] and a higher temperature response is expected. In contrast, $T_{degradation}$ represents the temperature at which the polymer starts to irreversibly degrade, and so actuation of the structures was conducted well below this temperature.

Fabrication of Uniaxially Aligned 3D Micro-Actuators

The fabrication process of uniaxially aligned 3D microstructures via DLW-TPP comprises several steps which are depicted in **Figure 2.1b**. Firstly, a cell (consisting of two glass plates held together by a 50 µm double-sided tape) prepared with alignment layers was filled with the LC photoresist at 105 °C using capillary forces. After filling, the cell was slowly cooled to room temperature, where the mixture exists in the more ordered nematic phase. The DLW-TPP process was then carried out to create 3D structures (hexagonal plates of 3 µm height and 20 µm width). The optimal writing speed was found to be 10 mm s^{-1}, with laser (λ = 780 nm) powers from 20-25 mW. After completion, a development step took place, consisting of submerging the cell in warm
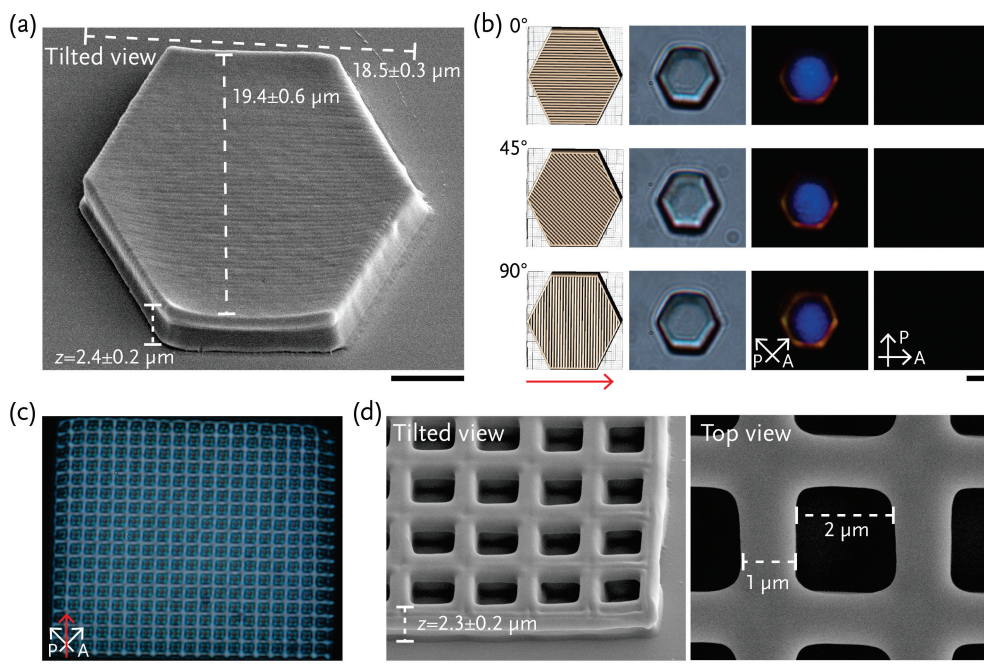
Figure 2.2 (a) Electron micrograph of a hexagonal plate. The sample was tilted at 40° to visualize and characterize its 3D dimensions. (b) On the left, the CAD designs of hexagonal plates of 9 × 9 × 4 µm³ in which the predetermined path of the laser is indicated in the drawings. The rectilinear paths are 0°, 45°, or 90° shifted with respect to the alignment of the mesogens in the cell, which is indicated by the red arrow. On the right, a series of optical micrographs of the fabricated hexagonal plates without and with crossed polarizers. (c) Polarized optical micrograph of the grid. In (b) and (c) the white arrows indicate the direction of the polarizer (P) and analyzer (A). (d) Electron micrographs of the grid shown in (c). The micrograph offering a tilted view was taken with the sample tilted 40°. All scale bars represent 4 µm. Error bars represent standard deviations for N = 3 measurements

isopropanol to dissolve unreacted monomers. Fabrication of the structures was started –0.5 μm from the glass/photoresist interface to improve the adhesion of the structures to the substrate. This served to avoid delamination, and any minor mismatch between the computer aided design (CAD) and the structure's height can be attributed to this offset. After development, complete polymerization was confirmed via confocal Raman spectroscopy by verifying the disappearance of the peak corresponding to the double-bond stretch of the acrylate group at 1635 cm^{-1} and 1725 cm^{-1}.

The dimensions and shape of the hexagonal plates were characterized via scanning electron microscopy (SEM), **Figure 2.2a**. The structures consist of an average 18.5±0.3 × 19.4±0.6 μm^2 hexagons with an average height of 2.4±0.2 μm. One dimension of the plates was remarkably close to the CAD design while the other dimension was ~8% shorter. 5-10% polymerization shrinkage is normal in acrylic samples,[39] and it occurs anisotropically in uniaxially aligned LC samples,[40] with the majority of the shrinkage along the axis parallel to the alignment, as was observed here. Further shrinkage could also be attributed to the removal of unreacted monomer from the network during the development step; however, we expect this to be minimal due to the high crosslink density of the network and the complete polymerization as verified by confocal Raman spectroscopy. Horizontal lines depicting the laser writing path are clearly visible in the electron micrograph: the lines effectively exhibit the polymerization voxel with a width of ~245 nm when DLW was performed at a 10 mm s^{-1} with 25 mW laser power. Overall, the plates showed a good resemblance to the CAD design, indicating a good performance of the LC photoresist with the DLW-TPP process.

The influence of the laser path during fabrication on the mesogenic alignment was investigated in the hexagonal plates (10 × 10 μm^2). Three different plates were explored, **Figure 2.2b**. The first plate was fabricated by scanning the laser parallel to the alignment (0°). For the second and third samples, the scanning paths were rotated 45° and 90° to the alignment, respectively. In all three cases, the fabricated plates showed similar dimensions and geometries (**Figure 2.2b**), indicating that the path chosen to fabricate the plate did not have a significant influence on the shape. The mesogenic alignment was characterized by polarized optical microscopy (POM). Regardless of the path chosen, all plates appeared darker when the cell alignment was parallel to the polarizer or analyzer and showed a stronger blue polarization color when aligned at 45° to the polarizer or analyzer due to the anisotropic optical property of LCs (*vide infra*). Such dark–bright states are associated with the presence of uniaxial alignment.[33,41,42] Thus, the mesogenic

alignment of these microstructures is determined by the alignment layer in the cell construct and not by the printing parameters or the scanning direction of the laser. This allows for facile pre-programmed determination of the alignment in the structures prior to fabrication by selection of appropriate alignment layers.

A grid in which the horizontal lines were printed with scans parallel to the alignment while the vertical lines were fabricated with scans perpendicular to the alignment layer direction was then fabricated (**Figure 2.2c-d**). Both vertical and horizontal lines showed the same monolithic alignment, reinforcing the finding that the scanning direction does not disturb the alignment in the cell. The grid had uniaxially aligned lines of ~1 μm in width with a periodicity of ~2 μm, and a height of 2.3±0.2 μm.

The potential of the presented LC photoresist with the DLW-TPP process was explored by fabricating more complex geometries, **Figure 2.3**. To this end, we printed an interwoven fabric, a woodpile, and a spiral disk. The interwoven fabric embodies a flat geometry that has interconnected features. The woodpile shows the possibility of fabricating a 3D photonic crystal, and the spiral disk demonstrates the capability of making structures that constantly change dimensions in all three planes. In all three cases, the structures showed good fidelity to the CAD design. Upon investigating the molecular alignment by POM, we verified that the microstructures exhibited monolithic alignment. Furthermore, the microstructures displayed distinct polarization colors: the interwoven fabric and woodpile structures displayed a yellow color, while the spiral disk exhibited a range of different colors. These colors arise from the anisotropic optical property of LCs,
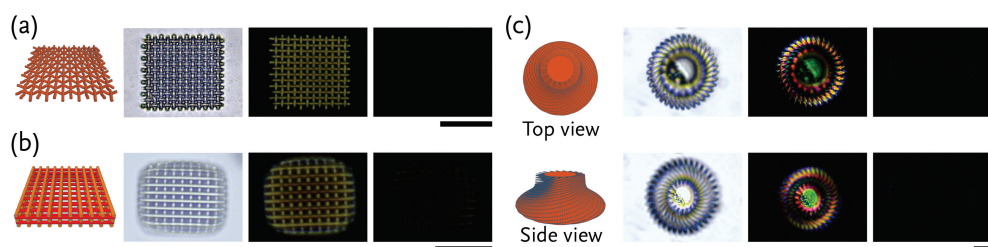
Figure 2.3 Uniaxially aligned 3D microstructures. (a) An interwoven fabric structure, (b) a woodpile, and (c) a spiral disk. From left to right, the CAD designs and optical and crossed polarized micrographs, respectively, with the polarizer and analyzer at 45° and 0° with respect to the direction of the alignment, which is vertical. For (c) the top row shows the spiral disk when the focus is located at the bottom of the structure and the bottom row when it is located at the top. All scale bars represent 20 μm.

defined as the difference between the extraordinary (n_e) and ordinary (n_o) refractive indices, also known as birefringence ($\Delta n = n_e - n_o$).[33,41] When light travels through a uniaxially aligned LC sample with a specific thickness (d), it encounters an optical path difference (OPD $= d\,\Delta n$) between transmitted extraordinary and ordinary rays that results in a polarization color when observed between crossed polarizers. Thus, the colors are dependent on the structure's height and geometry. This supports the presence of multiple colors observed for the spiral disk, and one single color in the "flat" interwoven fabric structure, for example. This unique and characteristic polarization color facilitates the object's identification, a characteristic much desired in the micro realm.[17,43]

Temperature Response

The temperature response of a row of hexagonal plates ($18.5\pm0.3 \times 19.4\pm0.6 \times 4.1\pm0.1$ µm³) was characterized using an optical profiling system. Upon heating from 20 °C to 220 °C, the plates showed an anisotropic shape change, contracting along the side parallel to the alignment direction (x) and expanding along the perpendicular side (y), with an increase in height (z); see **Figure 2.4a**. The anisotropic temperature response observed in the x and y directions is characteristic of uniaxially aligned networks. Such response comes from the increased molecular disorder induced by temperature that results in a contraction in the direction parallel to the alignment and in an expansion perpendicular to it.[10,25,33] A more detailed analysis of the temperature induced change of the plates' dimensions revealed that temperature response starts above 60 °C, **Figure 2.4b**. This onset temperature is close to the T_g, ~69 °C, of the network. Above the T_g the network is less stiff, resulting in the observed anisotropic shape change. At 220 °C, a contraction of 4.2±0.1% was observed in the x direction, with an expansion of 4.3±0.1% and 10.2±0.1%, seen in the y and z orientations, respectively, compared to their dimensions at 20 °C. The larger shape change observed in the z direction (~10%) with respect to the other orientations (~4%) could be attributed to the strong adherence of these structures to the glass substrate. We have previously characterized the swelling of micron sized structures fabricated using DLW-TPP.[19] Adhesion can play significant role in limitation of axial swelling, thereby focusing the possible swelling into the direction perpendicular to the substrate. Here a similar limitation could be occurring, explaining the bigger shape change in the z orientation. Additionally, the height changes between 30 °C to 220 °C over ten heating/cooling cycles were measured, and the results displayed in **Figure 2.4c**. The data show a reversible shape change with no indication of fatigue despite the actuation being at elevated temperatures.
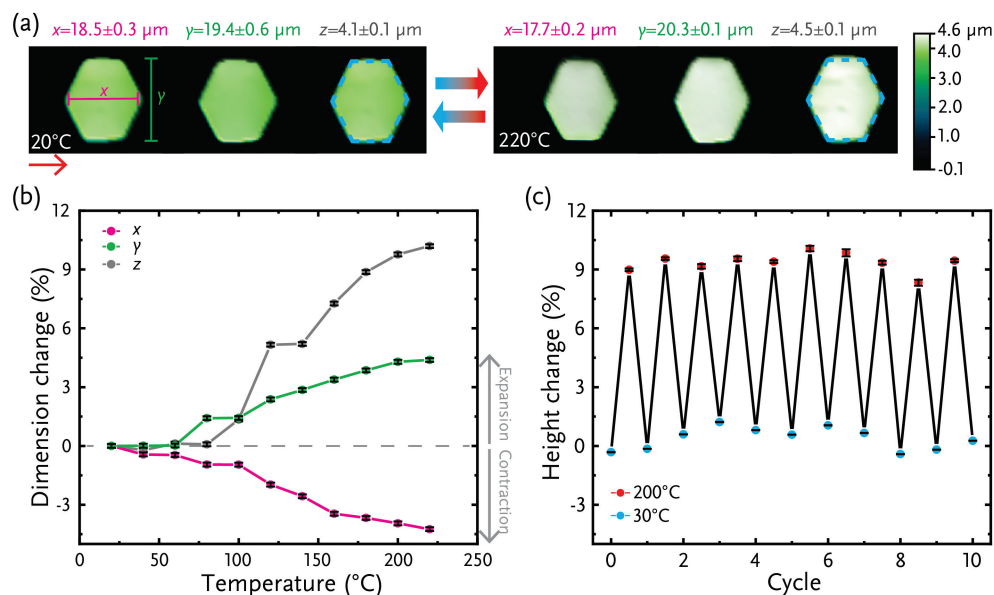
Figure 2.4 (a) 3D profiles of an array of hexagonal plates at 20 °C and 220 °C. The red arrow indicates the direction of the alignment of the mesogens. The blue dashed lines represent the contour of a plate at 20 °C. (b) Dimension change of the plates over a range of different temperatures. The dimensions *x* (in pink) and *y* (in green) are indicated in (a). (c) Height variation of the hexagonal plates over ten heating and cooling cycles, from 30 °C to 200 °C. For both (b) and (c), the fractional change is determined by comparing the current dimension of the plate with its value at 20 °C. For all measurements, the temperature was held for 5 min before recording the dimension. Error bars represent standard deviations for N = 3 measurements.

Finally, the temperature responses of a woodpile and a spiral disk were also investigated. In this case, the woodpile structure studied was composed of more stacks than depicted in **Figure 2.3** and therefore its birefringence color appeared blue instead of yellow, **Figure 2.5**. Upon heating to 200 °C, the structures showed an anisotropic shape change like those observed in the hexagonal plates (**Figure 2.4**). The woodpile reduced its dimensions 7% parallel to the mesogenic alignment and increased 6.5% perpendicular to it. Remarkably, the spiral disk expanded around 26% perpendicular to the alignment while it contracted only 5.5% in the parallel direction. When cooling to 30 °C, the structures recovered their initial shapes and dimensions. The enhanced performance of both structures in the *xy*-plane, which for the spiral disk is also significantly asymmetrical, in comparison with the plates can be explained by the difference in geometries that bring higher degrees of freedom when actuating, which can directly affect the actuation of the
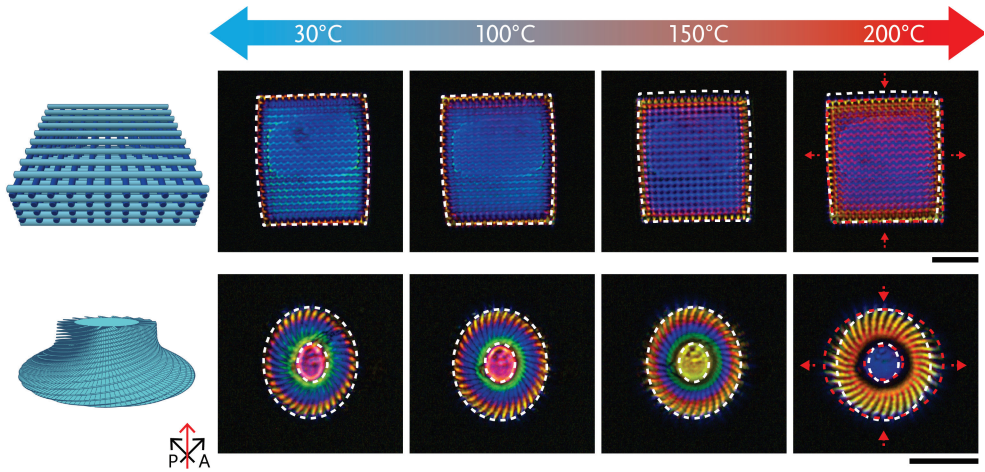
Figure 2.5 Temperature response of the 3D woodpile (top) and spiral disk (bottom) microstructures. From left to right: the CAD design and sets of crossed polarized optical micrographs recorded at different temperatures. The white and red dashed lines illustrate the contour of the structure at 30 °C and 200 °C, respectively. The red dashed arrows mark the direction of the shape change that occurs upon heating. The black arrows indicate the direction of the polarizer (P) and analyzer (A). The solid red arrow represents the direction of the alignment. The scale bars represent 20 μm.

microstructure. It has been shown before that by changing the geometry[23] or by making the structure free-standing,[44,45] larger actuation could be obtained. However, this is the first time that non-freestanding structures made from the same LC network show different percentages of shape changes when their response is triggered by an external stimulus; elucidating on the importance of choosing the optimal shape of the micro-actuator and not only on the most suitable material to fabricate it. Furthermore, temperature also had an influence on the polarization color of the structures. Upon an increment on temperature, both the structures thickness, *d,* and its birefringence, Δ*n,* change and with them the OPD, which is responsible for the polarization color (*vide supra*).[33,41] As a result, this inherent color can act as both an identifier and sensor for the microstructures.

2.3 Conclusions

Through the development of a LC photoresist, high-resolution 4D micro-actuators were fabricated via direct laser writing by two-photon polymerization. The mesogenic alignment of the structures was dictated by the one imposed by the alignment layers in the cell construct: the scanning

direction of the laser had no influence on alignment. As a result, a series of uniaxially aligned LC 3D microstructures were successfully fabricated displaying good fidelity to the CAD design. The structures showed reversible, anisotropic shape changes triggered by temperature that resulted in expansions between 10-26% at 200 °C, depending on the structure's geometry. The anisotropic shape change is attributed to the increased disorder that the mesogens undergo upon a temperature increase and can be easily controlled by controlling the direction of the mesogenic alignment. Furthermore, thanks to the monolithic alignment, the structures have unique and responsive polarization colors that makes them easy to identify and differentiate while permitting a facile verification of their status.

The results discussed in this chapter demonstrate the benefit of using highly crosslinked LCNs to fabricate micro-actuators via DLW-TPP, which reduces the swelling of the network from the unreacted monomer immediately after polymerization that otherwise hampers resolution. However, this comes at the expense of the micro-actuator's response which could only be achieved at elevated temperatures, which limit their implementation. Additionally, the results show the appeal of having unique and responsive, coloration in micro-actuator as it allows an *in situ* readability of their performance. The next chapter will focus on developing an LC photoresist to obtain response at lower temperature while maintaining high resolution and that result in micro-actuators that have structural coloration to enable real-time tracking of their status.

2.4 Experimental Details

Materials and Reagents

2-methyl-1,4-phenylene bis(4-(((4-(acryloyloxy)butoxy)carbonyl)oxy)benzoate) (**1**) was purchased from BASF. 1,4-di(4-(6-acryloyloxyhexyloxy)benzoyloxy)-2-methylbenzene (**2**), 1,4-di(4-(3-acryloyloxypropyloxy)benzoyloxy)-2-methylbenzene (**3**), and 4-(4-(6-acryloyloxyhexyloxy)benzoyloxy)benzonitrile (**4**) were supplied by Merck. The photoinitiator bis(2,4,6-trimethylbenzoyl)phenylphosphine oxide was purchased from Ciba Specialty and the thermal inhibitor 2-tert-butylbenzene-1,4-diol from Sigma-Aldrich. The polyamide AL 1051 was obtained from JSR Micro. All solvents were purchased from Biosolve.

LC Photoresist Preparation and Characterization

The LC photoresist consisted of 33.3 mol% **1**, 11.7 mol% **2**, 13.4 mol% **3**, 40.0 mol% **4**, 1.3 mol% photoinitiator. To avoid temperature-induced polymerization during the filling of the cell, a small quantity of polymerization inhibitor, 0.3 mol%, was incorporated. As a result, the LC photoresist

can be maintained at 105 °C for up to 8h without polymerizing. All components were dissolved in dichloromethane. The solvent was removed at 60 °C overnight under magnetic stirring.

Cell Preparation

High-precision microscope cover glasses (22×22 mm^2, thickness 170 ± 5 µm; from Marienfeld) were cleaned by sonication for 20 min in acetone and subsequently treated in a UV-ozone photo-reactor (Ultra Violet Products, PR-100) for 20 min to activate the surface. Polyamide AL 1051 was immediately spin coated on the glass (step 1: 800 rpm for 5 s; step 2: 5000 rpm for 40 s; both with an acceleration of 500 rpm s^{-1}) followed by a curing step of 180 min at 180 °C. The polyimide layer was then uniaxially rubbed with a velvet cloth, and the cell assembly made using a 50 µm thick double adhesive tape spacer in which the rubbed polyimide layer, acting as an alignment layers, were on the inside of the cell.

Computer Design of the Structures

All structures were fabricated based on a computer aided design. The designs of the hexagonal plates, grids, and woodpiles were custom made by the authors using the website www.tinker-cad.com. The spiral disk and the fabric-like structure were adapted from files licensed under the Creative Commons Attribution 4.0 International license and available at www.thingiverse.com. The files were modified using DeScribe 2.4.4 software to choose the slicing (0.2–0.5 µm) and hatching (0.2 µm) values.

Direct Laser Writing

First, the cell assembly was filled using capillary action with the LC photoresist in its isotropic phase at 105 °C. After filling, the temperature was slowly lowered to room temperature. Below the $T_{I/N}$, the molecules aligned parallel to the rubbing direction,[33] which in this case resulted in a uniaxial alignment, confirmed *in situ* by observing the cell between crossed polarizers. After verification of the alignment, localized TTP was performed in a commercial DLW workstation (Photonic Professional, Nanoscribe GmbH) equipped with a 170 mW femtosecond solid-state laser (λ = 780 nm) that delivers 120 fs pulses with an 80 MHz $\pm$ 1 MHz repetition rate. At a power scaling of 1, the average laser output is 50 mW. The laser beam was focused with a 63× oil objective (NA = 1.4; WD = 190 µm; Zeiss; Plan Apochromat) into the filled cell. The sample movement was controlled by a piezo translation stage in the *z*-axis and by a galvo stage in the *x*- and *y*-axes. The fabrication of the 3D microstructures was performed with scan speeds of 10 mm s^{-1} and laser powers between 20–25 mW, depending on the structure's geometry, hatching, and slicing values.

The fabrication started 0.5 µm below the automatically detected glass/photonic photoresist interface. Finally, the cell was submerged in warm isopropanol to dissolve the unreacted monomer. The cell was then carefully opened, and the glass rinsed with isopropanol and then air-dried.

Characterization

Electron micrographs were recorded using a Quanta FEG 3D SEM in secondary electron mode, beam current of 5 kV. Prior to imaging, the structures were sputtered coated with an Au-Pd layer. Optical micrographs were recorded on a Leica DM2700 M polarized optical microscope equipped with a Leica MC170 HD camera. All structures were visualized both in bright field and in transmission modes. The 3D profiles of the structures were obtained using an optical profiling system (S Neox 3D Optical profiler, equipped with a ×50 objective). When characterizing the temperature response of the structures, both the microscope and the optical profiling system were equipped with a Linkam TMS 600 hot-stage.

2.5 References

1   S. Nocentini, D. Martella, C. Parmeggiani and D. S. Wiersma, *Adv. Opt. Mater.*, 2019, **7**, 1900156.

2   J. del Barrio and C. Sánchez-Somolinos, *Adv. Opt. Mater.*, 2019, **7**, 1900598.

3   Y. W. Lee, H. Ceylan, I. C. Yasa, U. Kilic and M. Sitti, *ACS Appl. Mater. Interfaces*, 2021, 13, 12759–12766.

4   C. Yang, B. Wu, J. Ruan, P. Zhao, L. Chen, D. Chen and F. Ye, *Adv. Mater.*, 2021,**33**, 2006361.

5   Q. Chen, P. Lv, J. Huang, T.-Y. Huang and H. Duan, *Research*, 2021, **2021**, 1–16.

6   M. Tabrizi, T. H. Ware and M. R. Shankar, *ACS Appl. Mater. Interfaces*, 2019, **11**, 28236–28245.

7   C. A. Spiegel, M. Hippler, A. Münchinger, M. Bastmeyer, C. Barner-Kowollik, M. Wegener and E. Blasco, *Adv. Funct. Mater.*, 2020, **30**, 1907615.

8   Y. Yang, X. Song, X. Li, Z. Chen, C. Zhou, Q. Zhou and Y. Chen, *Adv. Mater.*, 2018, 30, 1706539.

9   S. Miao, N. Castro, M. Nowicki, L. Xia, H. Cui, X. Zhou, W. Zhu, S. jun Lee, K. Sarkar, G. Vozzi, Y. Tabata, J. Fisher and L. G. Zhang, *Mater. Today*, 2017, **20**, 577–591.

10   H. Zeng, P. Wasylczyk, C. Parmeggiani, D. Martella, M. Burresi and D. S. Wiersma, *Adv. Mater.*, 2015, **27**, 3883–3887.

11   M. Hippler, E. Blasco, J. Qu, M. Tanaka, C. Barner-Kowollik, M. Wegener and M. Bastmeyer, *Nat. Commun.*, 2019, **10**, 232.

12   D. Martella, S. Nocentini, D. Nuzhdin, C. Parmeggiani and D. S. Wiersma, *Adv. Mater.*, 2017, **29**, 1704047.

13   A. K. Nguyen and R. J. Narayan, *Mater. Today*, 2017, **20**, 314–322.

14   D. Jin, Q. Chen, T. Y. Huang, J. Huang, L. Zhang and H. Duan, *Mater. Today*, 2019, **32**, 19–25.

15   M. Dong, X. Wang, X. Z. Chen, F. Mushtaq, S. Deng, C. Zhu, H. Torlakcik, A. Terzopoulou, X. H. Qin, X. Xiao, J. Puigmartí-Luis, H. Choi, A. P. Pêgo, Q. D. Shen, B. J. Nelson and S. Pané, *Adv. Funct. Mater.*, 2020, **30**, 1910323.

16   Y. Hu, Z. Wang, D. Jin, C. Zhang, R. Sun, Z. Li, K. Hu, J. Ni, Z. Cai, D. Pan, X. Wang, W. Zhu, J. Li, D. Wu, L. Zhang and J. Chu, *Adv. Funct. Mater.*, 2020, **30**, 1907377.

17   M. del Pozo, C. Delaney, C. W. M. Bastiaansen, D. Diamond, A. P. H. J. Schenning and L. Florea, *ACS Nano*, 2020, **14**, 9832–9839.

18   C. C. Tartan, J. J. Sandford O'Neill, P. S. Salter, J. Aplinc, M. J. Booth, M. Ravnik, S. M. Morris and S. J. Elston, *Adv. Opt. Mater.*, 2018, **6**, 1800515.

19   A. Tudor, C. Delaney, H. Zhang, A. J. Thompson, V. F. Curto, G. Z. Yang, M. J. Higgins, D. Diamond and L. Florea, *Mater. Today*, 2018, **21**, 807–816.

20   F. Rajabasadi, L. Schwarz, M. Medina-Sánchez and O. G. Schmidt, *Prog. Mater. Sci.*, 2021, **120**, 100808.

21   G. Adam, A. Benouhiba, K. Rabenorosoa, C. Clévy and D. J. Cappelleri, *Adv. Intell. Syst.*, 2021, **3**, 2000216.

22   L. Chen, Y. Dong, C.-Y. Tang, L. Zhong, W.-C. Law, G. C. P. Tsui, Y. Yang and X. Xie, *ACS Appl. Mater. Interfaces*, 2019, **11**, 19541–19553.

23   S. Nocentini, D. Martella, C. Parmeggiani, S. Zanotto and D. S. Wiersma, *Adv. Opt. Mater.*, 2018, **6**, 1800167.

24   C. C. Tartan, P. S. Salter, T. D. Wilkinson, M. J. Booth, S. M. Morris and S. J. Elston, *RSC Adv.*, 2017, **7**, 507–511.

25   M. del Pozo, J. A. H. P. Sol, A. P. H. J. Schenning and M. G. Debije, *Adv. Mater.*, 2021, 2104390.

26   Y. Guo, H. Shahsavan and M. Sitti, *Adv. Mater.*, 2020, **32**, 2002753.

27   S. Zanotto, F. Sgrignuoli, S. Nocentini, D. Martella, C. Parmeggiani and D. S. Wiersma, *Appl. Phys. Lett.*, 2019, **114**, 201103.

28   S. Nocentini, F. Riboli, M. Burresi, D. Martella, C. Parmeggiani and D. S. Wiersma, *ACS Photonics*, 2018, **5**, 3222–3230.

29   V. S. R. Jampani, D. J. Mulder, K. R. De Sousa, A.-H. Gélébart, J. P. F. Lagerwall and A. P. H. J. Schenning, *Adv. Funct. Mater.*, 2018, **28**, 1801209.

30   H. Yoshida, C. H. Lee, Y. Matsuhisa, A. Fujii and M. Ozaki, *Adv. Mater.*, 2007, **19**, 1187–1190.

31   L. T. de Haan, J. M. N. Verjans, D. J. Broer, C. W. M. Bastiaansen and A. P. H. J. Schenning, *J. Am. Chem. Soc.*, 2014, **136**, 10585–10588.

32   L. T. de Haan, C. Sánchez-Somolinos, C. W. M. Bastiaansen, A. P. H. J. Schenning and D. J. Broer, *Angew. Chemie - Int. Ed.*, 2012, **51**, 12469–12472.

33   D. Liu and D. J. Broer, *Langmuir*, 2014, **30**, 13499–13509.

34   M. del Pozo, C. Delaney, M. Pilz da Cunha, M. G. Debije, L. Florea and A. P. H. J. Schenning, *Small Struct.*, 2021, 2100158.

35   C. P. Jisha, K.-C. Hsu, Y. Lin, J.-H. Lin, C.-C. Jeng and R.-K. Lee, *Opt. Lett.*, 2012, **37**, 4931.

36   C. C. Tartan, P. S. Salter, M. J. Booth, S. M. Morris and S. J. Elston, *J. Appl. Phys.*, 2016, **119**, 183106.

37   K. J. J. Schafer, J. M. M. Hales, M. Balu, K. D. D. Belfield, E. W. W. Van Stryland and D. J. J. Hagan, *J. Photochem. Photobiol. A Chem.*, 2004, **162**, 497–502.

38   D. C. Hoekstra, P. P. M. Visser, S. J. A. Houben, J. Lub, M. G. Debije and A. P. H. J. Schenning, *J. Appl. Phys.*,

2

2021, **129**, 75101.

39   M. H. Bland and N. A. Peppas, *Biomaterials*, 1996, **17**, 1109–1114.

40   R. A. M. Hikmet, B. H. Zwerver and D. J. Broer, *Polymer (Guildf).*, 1992, **33**, 89–95.

41   Y. Guo, H. Shahsavan and M. Sitti, *Adv. Opt. Mater.*, 2020, **8**, 1902098.

42   H. Zeng, D. Martella, P. Wasylczyk, G. Cerretti, J.-C. C. G. Lavocat, C.-H. H. Ho, C. Parmeggiani and D. S. Wiersma, *Adv. Mater.*, 2014, **26**, 2319–2322.

43   C. A. Koepele, M. Guix, C. Bi, G. Adam and D. J. Cappelleri, *Adv. Intell. Syst.*, 2020, **2**, 1900147.

44   S. Nocentini, D. Martella, C. Parmeggiani and D. Wiersma, *Materials (Basel).*, 2016, **9**, 525.

45   D. Martella, D. Antonioli, S. Nocentini, D. S. Wiersma, G. Galli, M. Laus and C. Parmeggiani, *RSC Adv.*, 2017, **7**, 19940–19947.

Chapter 3

Direct Laser Writing of 4D Structural Color Micro-Actuator Using a Photonic-Photoresist
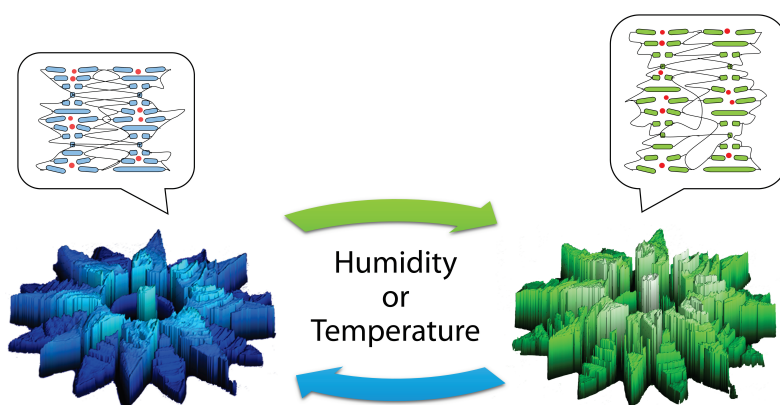
Abstract

Developing stimuli-responsive photonic-photoresists suitable for direct laser writing using two-photon polymerization for creating 4D microstructures remains a challenge. This chapter presents a supramolecular cholesteric liquid crystalline photonic-photoresist for the fabrication of 4D photonic micro-actuators, such as pillars, flowers, and butterflies, with sub-micron resolution. These micron-sized features display structural color and shape changes triggered by variation of humidity or temperature. These findings serve as a roadmap for the design and creation of high-resolution 4D photonic micro-actuators.

3.1 Introduction

Micro-actuators that respond to external stimuli have been fabricated using direct laser writing by two-photon polymerization (DLW-TPP) from low crosslinking density materials such as hydrogels,[1–4] polymerizable ionic liquids,[5] and liquid crystals (LC)[6–9] photoresists. In **Chapter 2**, we saw that highly crosslinked liquid crystal networks reduce swelling and improve resolution, but this comes at the cost of the structures' performance. The design of new LC photoresists is necessary to overcome this obstacle. **Chapter 2** also showed the benefit of having a responsive coloration in micro-actuators for tracking performance *in situ*. This could be appealing for microfluidics,[10] microelectromechanical systems (MEMS),[11] biotechnology,[12,13] surface modification,[14,15] and microrobots [16,17] as they would sense an external stimuli such as temperature, light, or other environmental stimuli and act by changing their color and shape in response.[18] Thus a photonic-photoresist that facilitates such 4D photonic micro-actuators is appealing, but it remains challenging to produce.

This chapter reports a photonic-photoresist based on supramolecular cholesteric liquid crystals (CLC) for the generation of stimuli-responsive photonic micro-actuators with sub-micron resolution via DLW-TPP. CLC networks exhibit a self-organized helical photonic structure that can selectively reflect light (**Figure 3.1**).[19] These networks can respond to a stimulus which triggers a shift in the reflection band, as a result of an anisotropic shape change of the helix.[20,21] To date, CLCs have been used in combination with DLW-TPP to investigate the effect of the surrounding monomer on the pitch of the polymerized CLC network[22–24] or to fabricate a stable uniform lying helix state,[25] but have not yet been explored for the fabrication of 4D photonic micro-actuators, despite CLCs being an ideal candidate for this purpose. This chapter demonstrates that the marriage of stimuli-responsive self-ordering materials with DLW-TPP enables the fabrication of a range of dual-responsive 3D microstructures, which can respond to variations in humidity and temperature through modulation of their shape and color.

3.2 Results and Discussion

Liquid Crystal Photonic-Photoresist

The photonic-photoresist reported here is based on a hydrogen bonded CLC mixture which can be polymerized into coatings to demonstrate structural color and shape changes.[21,26] Optimization of the photonic-photoresist composition, to enable room temperature fabrication, yielded a LC mixture comprising the compounds in **Figure 3.1a**. The optimized photonic-photoresist has

an isotropic to chiral nematic phase at ~48 °C that is stable at room temperature for several hours without crystallizing. The di-functional mesogenic acrylates **1-2** act as chemical crosslinkers to ensure that a network is obtained during the DLW-TPP fabrication process. The mono-functional mesogenic acrylates **3-4** add flexibility to the network. The mono-functional mesogenic carboxylic acids **5-8** act as supramolecular hydrogen bonded crosslinkers during the DLW-TPP fabrication. After polymerization, the hydrogen bonds can be cleaved via base treatment, by exposing the structures to 1M KOH for 1 minute. This gives flexibility and humidity-responsiveness to the
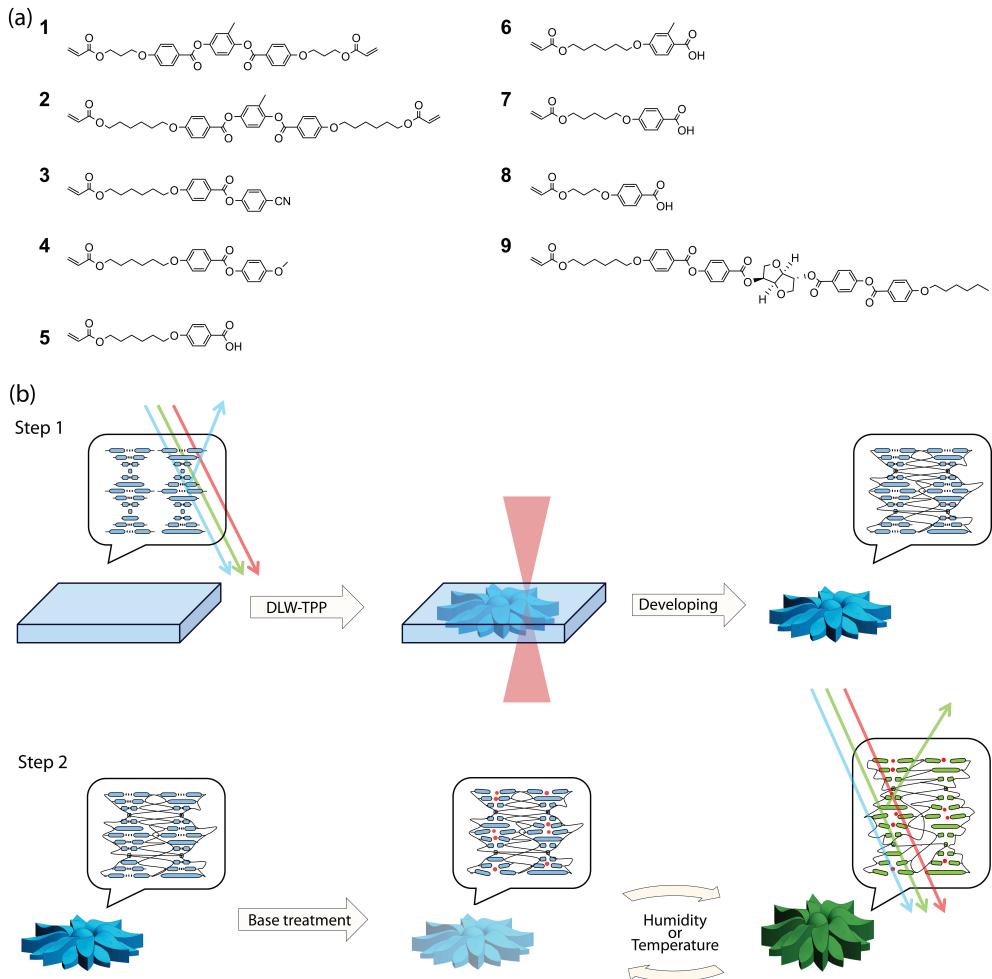

Figure 3.1. (a) Overview of the reactive mesogenic monomers used to prepare the photonic-photoresist. (b) Schematic of the fabrication (Step 1) and structure activation (Step 2), to obtain 4D photonic micro-actuators. Red spheres represent the potassium cations present after base treatment and the blue and green rods represent the mesogens.

network due to the creation of a charged, hygroscopic polymer. The chiral dopant **9** (optimized at 2.3 mol%) induces a helical organization in the nematic LC mixture to achieve a photonic-photoresist, with a reflection band centered at 400 nm.[27] Lastly, 0.8 mol% of Irgacure 819 photoinitiator was added. This photoinitiator has been previously employed as a two-photon free-radical initiator for acrylate-based resins in DLW-TPP.[28–32] To ensure covalent attachment of the microstructures to the substrate, the glass surface was treated with 3-(trimethoxysilyl)propyl acrylate. The fabrication of photonic micro-actuators via DLW-TPP and subsequent activation are depicted in **Figure 3.1b**.

Fabrication of 3D Photonic Micro-Actuators

To initially test and optimize the DLW set-up, arrays of micron-sized square pillars were fabricated, **Figure 3.2**. Optimized printing parameters yielded writing speeds between 5000 µm·s^{-1} – 10000 µm·s^{-1}, with laser powers between 20 – 22.5 mW. To ensure complete attachment to the functionalized surface, fabrication of the structures started at -0.5 µm from the glass/photonic-photoresist interface and any minor mismatch between the structure height and computer assisted design (CAD) can be attributed to this. After removing the unreacted monomer, the pillars show a blue reflection which confirms the preservation of cholesteric alignment, as shown in

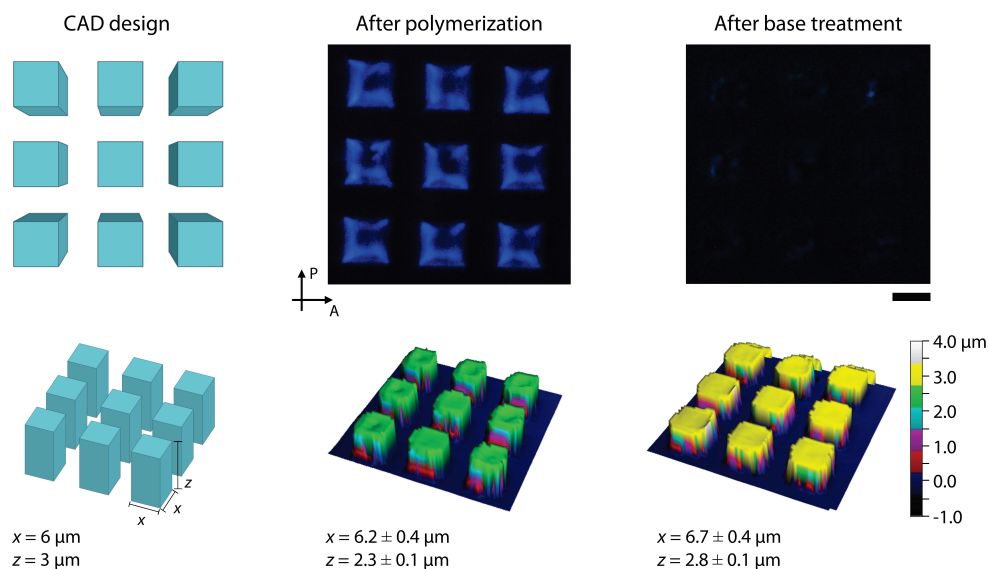| CAD design	After polymerization	After base treatment
$x = 6$ µm $z = 3$ µm	$x = 6.2 \pm 0.4$ µm $z = 2.3 \pm 0.1$ µm	$x = 6.7 \pm 0.4$ µm $z = 2.8 \pm 0.1$ µm

Figure 3.2. Structural and optical characterization of an array of pillars after polymerization and after base treatment. Top-crossed polarized micrographs; bottom-3D profiles of the array of pillars. The scale bar represents 10 µm.

Figure 3.2. Visualization of the photonic character of the objects is enhanced through the use of crossed linear polarizers.[27] Polymerization was confirmed via confocal Raman spectroscopy, by observing the reduction of the peak corresponding to the double bond stretch of the acrylate group at 1635 cm^{-1}.[27] The shape of the pillars was characterized using an optical profiling system. The CAD design comprised pillars of 6 μm width and a height of 3 μm in a square lattice. The fabricated pillars showed an average width of 6.2±0.4 μm, and an average height of 2.3±0.1 μm. Such high fidelity between the fabricated object and design file indicates that only minimal swelling occurred during the DLW-TPP process; most likely due to the highly effective supramolecular crosslinking density achieved during fabrication.

Subsequent base treatment of the pillars served to cleave the hydrogen bonds between molecules **5-8**; as verified via confocal Raman spectroscopy by observing the reduction of the carboxylic acid peaks at 1647 cm^{-1} and 1280 cm^{-1} and the appearance of the carboxylic salt peak at 1395 cm^{-1}.[27] This treatment results in a charged hygroscopic photonic polymer which is sensitive to changes in humidity and temperature.[26,33] **Figure 3.2** shows the pillars before (middle) and after the base treatment (right). Firstly, the micrograph indicates that the activation step has reduced the intensity of the reflection band, which is a phenomenon also observed in a homogeneous coatings made with the same photonic-photoresist that is attributed to the loss of molecular order due to the cleavage of the hydrogens bonds.[26,33] Secondly, the dimensions of the pillars appear to be slightly bigger than prior to the activation step, showing an average width of 6.7±0.4 μm with an average height of 2.8±0.1 μm. This difference can be explained due to the fact that the structures are now responsive to humidity changes (*vide infra*).

Photonic micro-structures were then fabricated to explore the possibilities of making high resolution photonic 3D constructs (**Figure 3.3**). A flower (**Figure 3.3a**), a butterfly (**Figure 3.3b**) and the pattern of the wing of the *Papilio paris* butterfly (**Figure 3.3c**) were fabricated. In the micrograph of the flower, the tiered layers of the structure can be easily observed. In this instance, a slice thickness of 0.5 μm was used to fabricate the 6 μm tall flower. In the other structures such layers are not clearly visible due to their geometry and decreased slice thickness. In all cases, the structures displayed a blue color after fabrication, confirming preservation of the photonic structure within the polymer and showing good fidelity to the computer design, even after base treatment. The biomimetic pattern, shown in **Figure 3.3c**, serves to demonstrate the capabilities of the photonic-photoresist, when used with DLW-TPP, to produce high-resolution nanometer

features. Additional fabrication studies confirm that feature sizes below 200 nm can be reproducibly fabricated using the methods outlined herein.[27]

It is worth noting that for the butterfly, shown in **Figure 3.3b**, the amount of light reflected is notably less than other structures owed to the small height of features. To efficiently reflect light, a minimum height needs to be achieved, which can be calculated using the following equation:

$$\lambda = n \cdot P \cdot \cos (\theta) \qquad\qquad (1)$$

in which λ is the center of the reflection band, n is the refractive index, P is the pitch size, which represents a full rotation of the molecules, and θ is the incident angle.[19] Taking the center of the reflection band to be at 400 nm, an incident angle of 90° and a refractive index of 1.5, the calculated pitch size is 266 nm. As at least ten pitches are required to efficiently reflect light, the minimum feature height to reflect light is 2.66 µm. For this reason, reflected color of features with heights in this range can only be observed between polarizers, as seen in **Figure 3.3b** (inset).

Humidity and Temperature Response

The response of CLC networks, outlined in **Equation 1**, shows that a change in pitch results in a shift of the reflection band, with an increase in pitch resulting in a relative red shift, and a decrease resulting in a blue shift. A detailed characterization of the flower shown in **Figure 3.3** was conducted by an optical profiling system, to characterize shape change (**Figure 3.4**) and by an optical microscope to quantify color change (**Figure 3.5**). **Figure 3.4a** shows the height increase of the flower across a range of temperatures and humidity values. The control of humidity was achieved through the use of a custom-built humidity chamber which encased the sample and the microscope objective. At 75 percent relative humidity (%RH), as the temperature of the structure reached the dew point (18 °C), the height increased dramatically and reached an increase of 42 % at 19 °C. This trend was also observed for the 60 %RH measurements showing a maximum height increase of 22 % at 19 °C. However, at 15 %RH the increment was less steep, owed to a larger temperature deviation from the calculated dew point (-5 °C). Upon heating, water was removed from the flower, which resulted in a decrease in height. At 70 °C, regardless of the humidity, the structure showed no discernible change in height. **Figure 3.4b** demonstrates the reversibility of the response at 75 %RH, over ten cycles, between 25 °C (12-18 % expansion) and 20 °C (25-30 % expansion). It is known that the shape change of the structures is related to the charged hygroscopic polymer network obtained after base treatment which, in the presence of water vapors, results in a significant uniform expansion of the polymer network,[19,26] which occurs perpendicular

to the glass substrate. **Figure 3.4c** shows the dynamic response in the flower's height when changes in humidity or in temperature occur. When the relative humidity is varied, the amount of water vapor in air changes and accordingly the flower expands or contracts. This may also be achieved by modulating the temperature of the structure. As temperature dictates the rate of water evaporation, increasing temperature results in contraction of the structure. Conversely, decreasing temperature close to the dew point results in expansion. This enables actuation of the structures directly (via humidity changes) and indirectly (via temperature changes). The controlled expansion of the micro-actuators via temperature or humidity triggers changes in the pitch of the ordered CLC, thereby leading to variations in the reflection band (**Figure 3.5a**). **Figure 3.5b** shows

(a) (b) (c)

3

20 µm   10 µm

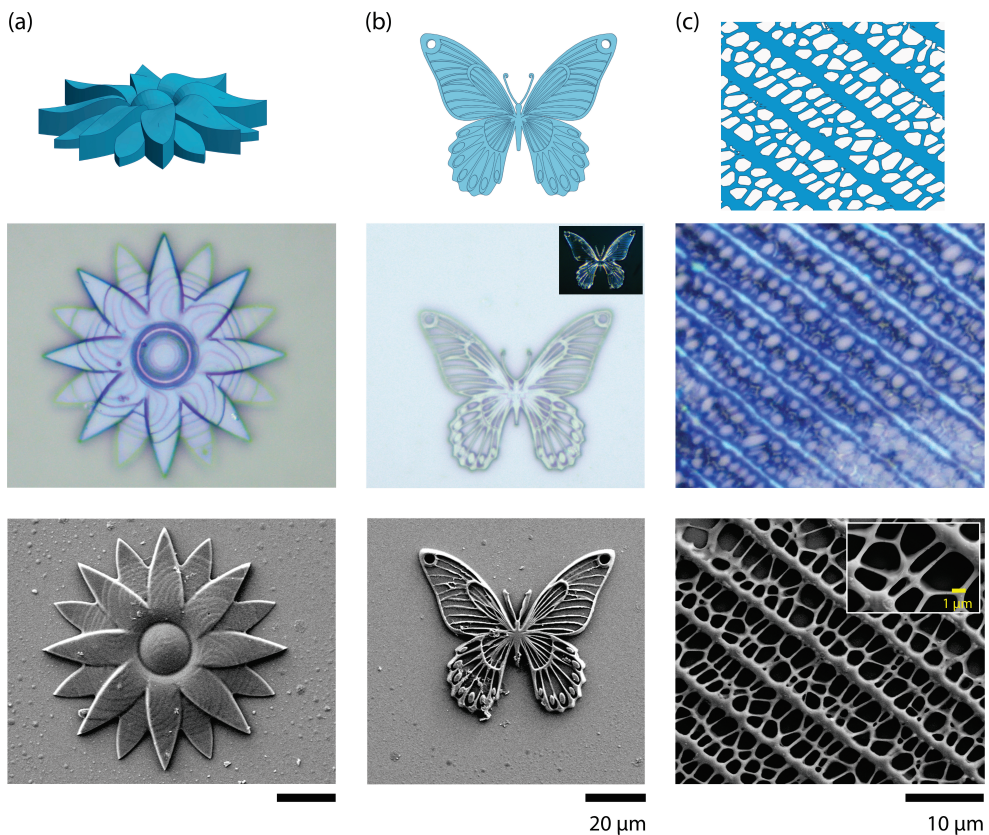**Figure 3.3**. Photonic 3D microstructures. From top to bottom, the CAD designs of the structures, optical microscopy and scanning electron microscopy (SEM) images before base treatment of (a) a flower, (b) a butterfly, and (c) the pattern of the wing of the *Papilio paris* butterfly. The inset in (b) is a crossed linear polarized micrograph of the butterfly, used to enhance observation of the reflected color.
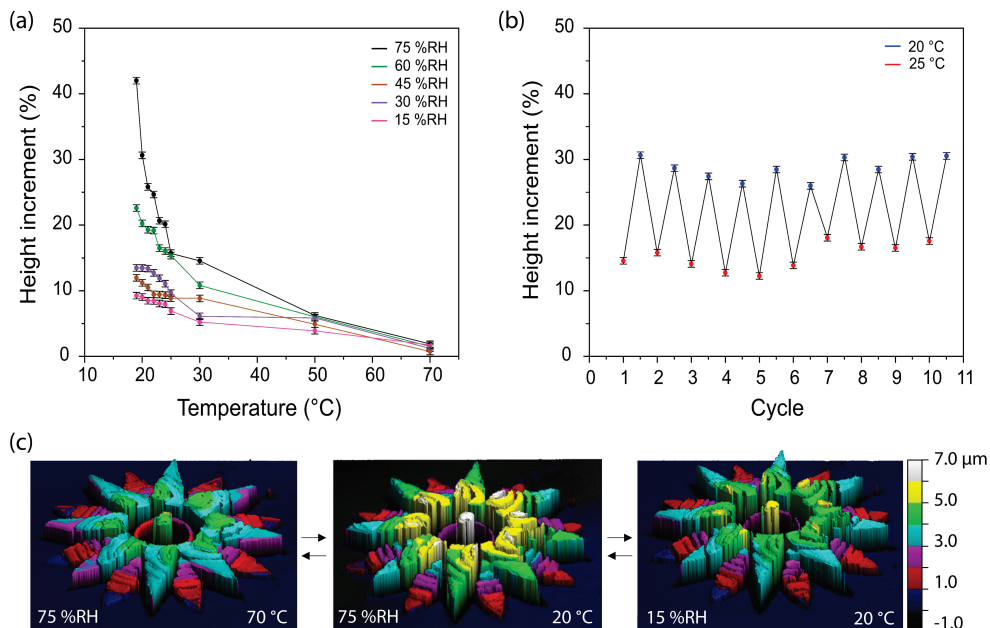
Figure 3.4 Characterization of the actuation of a flower at different atmospheric conditions and temperatures. (a) Height changes of the flower over a range of different temperature and humidity values. (b) Increment of the flower height over ten cycles, going from 25 °C to 20 °C, at 75±2 %RH. For both (a) and (b), the percentage of height increment is obtained by averaging the values of the top of the flower and comparing them to the height of the flower before base treatment. For all measurements, the flower was held for 5 min after reaching the desired conditions before recording its height. Error bars represent standard deviations for N=3 measurements. (c) 3D profiles of the flower which depict direct (triggered by humidity) or indirect (triggered by temperature) actuation.

the color change of the structure achieved by varying temperature at constant 75 %RH. The data points were obtained from the corresponding polarized micrographs following a previously reported procedure.[34] Upon decreasing the temperature, a gradual and linear response of color change from colorless to light blue was observed. However, it was not until below the dew point (18 °C), that the flower showed its most spectacular color change, from light blue to bright green, corresponding to the increased water absorption of the network.[26]

The dual-response of this type of 4D photonic micro-actuators can be seen in **Figure 3.5c**. When breathing on top of the flower, it displayed the same response as observed in **Figure 3. 5b**, but this time much faster and stronger due to the steeper and higher change in humidity. As a
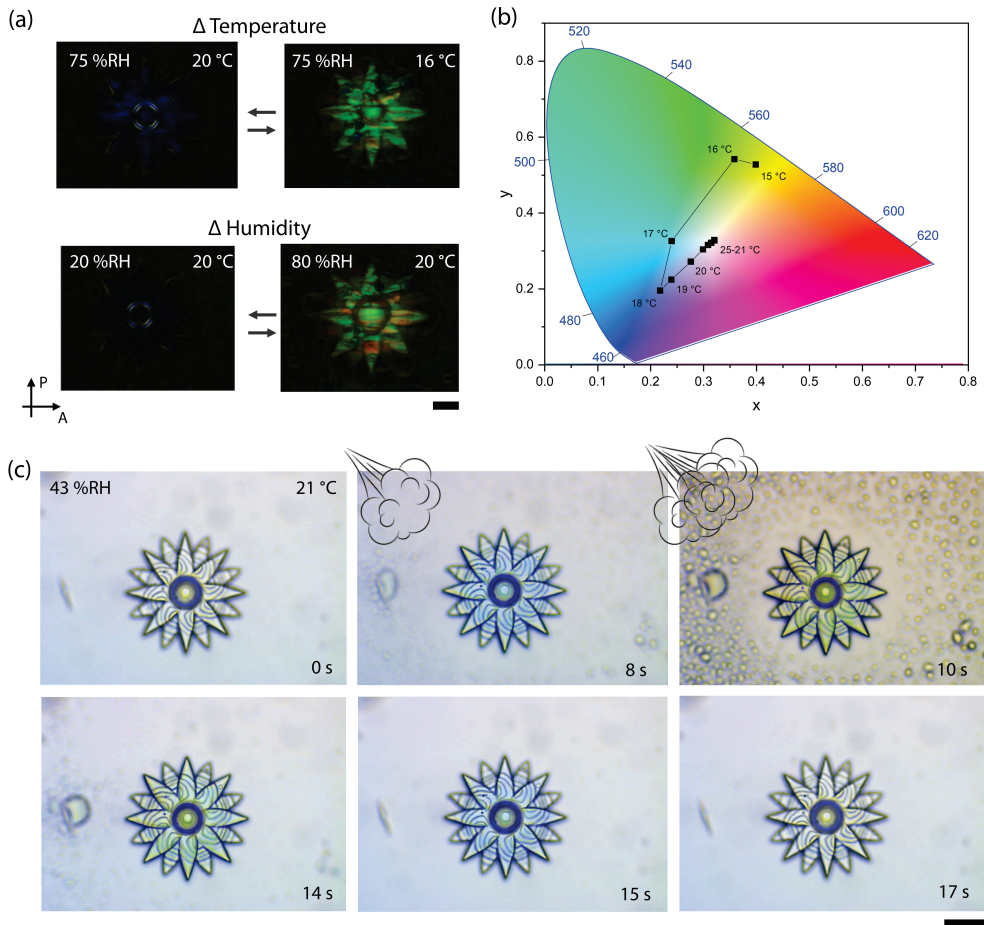
Figure 3.5 Characterization of the optical response of the microflower. (a) Crossed polarized micrographs of the flower showing the direct (triggered by humidity), or indirect (triggered by temperature), induced color changes. (b) Chromaticity diagram (standard CIE 1931) showing the color changes of the flower over a range of temperatures, at a constant 75 %RH. The data points are obtained from the corresponding crossed polarized micrographs that can be found in the supporting information. (c) A sequence of micrographs that display the optical response of the flower upon exposure to breath (top row) and after (bottom row). All scale bars represent 20 μm.

result, the flower changes from transparent to blue in ~8 s and from blue to green within ~4 s and then recovers its initial state within ~3 s. This demonstrates the ability to exploit a fast visual response, which can be attributed to the miniaturization of the system when compared with analogous macro-sized systems.[21,26] This behavior shows how, for example, the system presented herein is attractive for the fabrication of 4D photonic micro-actuators in which the synergistic

photonic response can act as a visual probe for shape change or for the generation of fast response anti-counterfeiting features. Furthermore, the incorporation of structural color in micro-structures can be used to enhance their visualization and enable real-time interrogation, as recently shown for microrobots.[35]

3.3 Conclusions

In conclusion, through the development of a supramolecular photonic-photoresist, high resolution 4D photonic micro-actuators were fabricated via DLW-TPP. These structures showed a dual-response to changes in humidity (directly) and temperature (indirectly). The shape change, up to 42 % at 75 %RH, is attributed to the hygroscopic character of the polymer network, after activation. The controlled expansion of the micro-actuators at different temperature and humidity values results in a corresponding structural color change, owed to modulation of the nanoscale CLC pitch in the ordered network. As a result, the presented supramolecular LC photonic-photoresist overcomes the challenges that low crosslink density network suffer in the DLW-TPP process while offering a facile real-time verification of their status, which is appealing to fields such as microrobots.

In **Chapter 2** and **Chapter 3** we have developed two LC photoresists that have been used to fabricate 4D micro-actuators. The next chapters will focus on centimeter sized 4D actuators, that will be fabricated via direct ink writing of liquid crystals elastomers. Light responsive actuators will be produced having atypical deformation modes.

3.4 Experimental Details
Materials and Reagents

2-methyl-1,4-phenylene bis(4-(3-(acryloyloxy)propoxy)benzoate) (**1**), 2-methyl-1,4-phenylene bis(4-((6-(acryloyloxy)hexyl)oxy)benzoate) (**2**), 4-cyanophenyl 4-((6-(acryloyloxy)hexyl)oxy)benzoate (**3**), and 4-methoxyphenyl 4-((6-(acryloyloxy)hexyl)oxy)benzoate (**4**) were purchased from Merck. 4-((6-(acryloyloxy)hexyl)oxy)benzoic acid (**5**) was supplied by Ambeed. 4-((6-(acryloyloxy)hexyl)oxy)-2-methylbenzoic acid (**6**), 4-((5-(acryloyloxy)pentyl)oxy)benzoic acid (**7**), and 4-(3-(acryloyloxy)propoxy)benzoic acid (**8**) were provided by Synthon. (3R,3aS,6S,6aS)-6-((4-((4-((6-(acryloyloxy)hexyl)oxy)benzoyl)oxy)benzoyl)oxy)hexahydrofuro[3,2-b]furan-3-yl 4-((4-(hexyloxy)benzoyl)oxy)benzoate (**9**) was synthesized as previously reported.[36] Irgacure 819 was purchased from

Ciba Specialty and 3-(trimethoxysilyl)propyl methacrylate from Sigma Aldrich. Potassium hydroxide pellets (85 %) was obtained from Alfa Aesar. All solvents were purchased from Biosolve.

Photonic-Photoresist Preparation

The CLC monomer mixture consisted of 3.4 mol % **1**, 3.1 mol % **2**, 12.4 mol % **3**, 11.0 mol % **4**, 15.3 mol % **5**, 29.2 mol % **6**, 10.7 mol % **7**, 11.9 mol % **8**, 2.3 mol % **9**, and 0.8 mol % Irgacure 819. All components were dissolved in tetrahydrofuran. Solvent was removed at 80 °C overnight. Characterization of the resulting CLC mixture can be found in the Supplementary Information.

Cell Preparation

High precision microscope cover glasses (22 × 22 mm², thickness 170±5 µm; from Marienfeld) were cleaned by sonication for 20 min in acetone. For functionalization, slides were treated in a UV-ozone photoreactor (Ultra Violet Products, PR-100) for 20 min to activate the surface and were immediately functionalized with methacrylate groups by spin coating (3000 rpm, 45 s) a 3-(trimethoxysilyl)propyl methacrylate solution (1 vol.% solution in a 1:1 water-isopropanol mixture) followed by a curing step of 10 min at 100 °C. Following this, the functionalized slide was attached to a second, unfunctionalized slide, using a 50 µm thick double adhesive tape spacer, to form a simple cell assembly.

Computer Design of the Structures

All structures were fabricated based on a computer design. The design of the structures was custom-made by the authors using SketchUp or adapted from files licensed under the Creative Commons Attribution 4.0 International license and available at www.thingiverse.com. These can be downloaded from the creators at the respective links: www.thingiverse.com/thing:2500769 for the flower and www.thingiverse.com/thing:816098/files for the butterfly. The files were modified using DeScribe 2.4.4 software to choose the slicing (0.2-0.5 µm) and hatching (0.2 µm) values.

Direct Laser Writing

The cell was filled by capillarity with the CLC mixture at room temperature. The filling resulted in an aligned CLC. Localized TTP was conducted in a commercial DLW workstation (Photonic Professional, Nanoscribe GmbH) equipped with a 170-mW femtosecond solid-state laser (λ = 780 nm) that delivers 120-fs pulses with an 80±1 MHz repetition rate. The laser beam was focused with a 63x oil objective (NA = 1.4; WD = 190 µm; Zeiss; Plan Apochromat) into the filled cell. The sample movement was controlled by a piezo translation stage in the z-axis and by a galvo stage in the x- and y-axis. The fabrication of the 3D microstructures was performed at different laser

3

powers (20 – 25 mW) and scan speeds (5000 µm s^{-1} – 10000 µm s^{-1}) depending on the structure's geometry, and hatching, and slicing values. Structure fabrication was initiated 0.5 µm below the automatically detected glass/photonic-photoresist interface. After DLW-TPP, the structures were washed in warm isopropanol until all the unreacted monomer had dissolved. The cell was then opened and the functionalized glass rinsed with isopropanol and air-dried. The activation of the structures was performed by placing a drop of 1M KOH solution on top of the structures for 1 min. The basic solution was rinsed with water and the structures were then dried by heating at 70 °C for 10 min using a hot plate.

Characterization

Micrographs were recorded on a Leica DM2700M polarized optical microscope equipped with a Leica MC170 HD camera. The video was recorded using OBS Studio software. All structures were visualized in bright field and in reflection mode. The 3D profiles of the structures were obtained using an optical profiling system (Zoomsurf 3D; Fogale nanotech). To measure the height and color changes at different humidity and temperature, both the microscope and the profiling system were equipped with a transparent custom-built humidity chamber in which the internal humidity and air temperature were controlled manually and monitored with a sensor (SHT3x, Sensirion) and the temperature of substrate controlled with a Linkam TMS 600 hot-stage. The specific humidity values, corresponding to the different relative humidity values and air temperatures, can be found in the literature.[27] Electron micrographs were recorded using a Zeiss ULTRA Plus Scanning Electron Microscope. The structures were coated, prior to imaging, with a 10 nm Au-Pd layer using a Cressington Sputter Coater 208HR and a 57 × 0.1 mm Au-Pd target (TED PELLA INC.).

Image Analysis

The crossed polarized micrographs of microflower at different temperatures and constant humidity were acquired by keeping constant the camera acquisition settings to avoid false color change. The images were analyzed without any modification. First, the average RGB values from the images were obtained using Image J software. Then, the RGB values were transformed to (x,y) values to be plotted in a chromaticity diagram (standard CIE 1931) as previously reported.[43]

3.5 References

1 M. Hippler, E. D. Lemma, S. Bertels, E. Blasco, C. Barner-Kowollik, M. Wegener and M. Bastmeyer, *Adv. Mater.*, 2019, **31**, 1808110.
2 M. Hippler, E. Blasco, J. Qu, M. Tanaka, C. Barner-Kowollik, M. Wegener and M. Bastmeyer, *Nat. Commun.*, 2019, **10**, 232.
3 D. Jin, Q. Chen, T. Y. Huang, J. Huang, L. Zhang and H. Duan, *Mater. Today*, 2019, **32**, 19–25.
4 H. Ceylan, I. C. Yasa, O. Yasa, A. F. Tabak, J. Giltinan and M. Sitti, *ACS Nano*, 2019, **13**, 3353–3362.
5 A. Tudor, C. Delaney, H. Zhang, A. J. Thompson, V. F. Curto, G. Z. Yang, M. J. Higgins, D. Diamond and L. Florea, *Mater. Today*, 2018, **21**, 807–816.
6 H. Zeng, P. Wasylczyk, C. Parmeggiani, D. Martella, M. Burresi and D. S. Wiersma, *Adv. Mater.*, 2015, **27**, 3883–3887.
7 A. M. Flatae, M. Burresi, H. Zeng, S. Nocentini, S. Wiegele, C. Parmeggiani, H. Kalt and D. Wiersma, *Light Sci. Appl.*, 2015, **4**, 2–6.
8 L. Chen, Y. Dong, C. Y. Tang, L. Zhong, W. C. Law, G. C. P. Tsui, Y. Yang and X. Xie, *ACS Appl. Mater. Interfaces*, 2019, **11**, 19541–19553.
9 S. Zanotto, F. Sgrignuoli, S. Nocentini, D. Martella, C. Parmeggiani and D. S. Wiersma, *Appl. Phys. Lett.*, 2019, **114**, 201103.
10 K. Sugioka, J. Xu, D. Wu, Y. Hanada, Z. Wang, Y. Cheng and K. Midorikawa, *Lab Chip*, 2014, **14**, 3447–3458.
11 R. K. Jayne, T. J. Stark, J. B. Reeves, D. J. Bishop and A. E. White, *Adv. Mater. Technol.*, 2018, **3**, 1–6.
12 A. Marino, A. Desii, M. Pellegrino, M. Pellegrini, C. Filippeschi, B. Mazzolai, V. Mattoli and G. Ciofani, *ACS Nano*, 2014, **8**, 11869–11882.
13 A. Marino, J. Barsotti, G. De Vito, C. Filippeschi, B. Mazzolai, V. Piazza, M. Labardi, V. Mattoli and G. Ciofani, *ACS Appl. Mater. Interfaces*, 2015, **7**, 25574–25579.
14 X. Liu, H. Gu, M. Wang, X. Du, B. Gao, A. Elbaz, L. Sun, J. Liao, P. Xiao and Z. Gu, *Adv. Mater.*, 2018, **30**, 1800103.
15 Y. Lin, R. Zhou and J. Xu, *Adv. Mater. Interfaces*, 2018, **5**, 1–8.
16 A. Servant, F. Qiu, M. Mazza, K. Kostarelos and B. J. Nelson, *Adv. Mater.*, 2015, **27**, 2981–2988.
17 U. Bozuyuk, O. Yasa, I. C. Yasa, H. Ceylan, S. Kizilel and M. Sitti, *ACS Nano*, 2018, **12**, 9617–9625.
18 M. Carlotti and V. Mattoli, *Small*, 2019, **15**, 1902687.
19 D. J. Mulder, A. P. H. J. Schenning and C. W. M. Bastiaansen, *J. Mater. Chem. C*, 2014, **2**, 6695–6705.
20 J. E. Stumpel, D. J. Broer, C. W. M. Bastiaansen and A. P. H. J. Schenning, in *Organic Photonics VI*, 2014, vol. 9137, p. 91370U.
21 M. Moirangthem and A. P. H. J. Schenning, *ACS Appl. Mater. Interfaces*, 2018, **10**, 4168–4172.
22 H. Yoshida, C. H. Lee, A. Fujii and M. Ozaki, *Appl. Phys. Lett.*, 2006, **89**, 231913.
23 H. Yoshida, C. H. Lee, Y. Matsuhisa, A. Fujii and M. Ozaki, *Adv. Mater.*, 2007, **19**, 1187–1190.
24 H. Yoshida, *Liq. Cryst. Today*, 2012, **21**, 3–19.
25 C. C. Tartan, P. S. Salter, M. J. Booth, S. M. Morris, S. J. Elston, C. C. Tartan, P. S. Salter, M. J. Booth, S. M. Morris and S. J. Elston, *J. Appl. Phys.*, 2016, **119**, 183106.
26 E. P. A. A. Van Heeswijk, J. J. H. H. Kloos, N. Grossiord and A. P. H. J. H. J. Schenning, *J. Mater. Chem. A*, 2019, **7**, 6113–6119.
27 M. del Pozo, C. Delaney, C. W. M. Bastiaansen, D. Diamond, A. P. H. J. Schenning and L. Florea, *ACS Nano*, 2020, **14**, 9832–9839.
28 C. Plamadeala, F. Hischen, R. Friesenecker, R. Wollhofen, J. Jacak, G. Buchberger, E. Heiss, T. A. Klar, W. Baumgartner and J. Heitz, *R. Soc. Open Sci.*, 2017, **4**, 160849.
29 C. P. Jisha, K. C. Hsu, Y. Lin, J. H. Lin, C. C. Jeng and R. K. Lee, *Pacific Rim Conf. Lasers Electro-Optics, CLEO - Tech. Dig.*, 2013, 1–2.
30 T. Sherwood, C. Young, J. Takayesu, A. K. Jen, L. Dalton and A. Chen, in *Organic Photonic Materials and Devices VII*, eds. J. G. Grote, T. Kaino and F. Kajzar, SPIE, 2005, vol. 5724, p. 356.
31 C. C. Tartan, J. J. Sandford O'Neill, P. S. Salter, J. Aplinc, M. J. Booth, M. Ravnik, S. M. Morris and S. J. Elston, *Adv. Opt. Mater.*, 2018, **6**, 1800515.
32 K. J. Schafer, J. M. Hales, M. Balu, K. D. Belfield, E. W. Van Stryland and D. J. Hagan, *J. Photochem. Photobiol. A Chem.*, 2004, **162**, 497–502.
33 H. P. C. van Kuringen, Z. J. W. A. Leijten, A. H. Gelebart, D. J. Mulder, G. Portale, D. J. Broer and A. P. H. J. Schenning, *Macromolecules*, 2015, **48**, 4073–4080.
34 B. Zuo, M. Wang, B.-P. P. Lin and H. Yang, *Chem. Mater.*, 2018, **30**, 8079–8088.
35 C. A. Koepele, M. Guix, C. Bi, G. Adam and D. J. Cappelleri, *Adv. Intell. Syst.*, 2020, **2**, 1900147.
36 Y. Foelen, D. A. C. Van Der Heijden, M. Del Pozo, J. Lub, C. W. M. Bastiaansen and A. P. H. J. Schenning, *ACS Appl. Mater. Interfaces*, 2020, **12**, 16896–16902.

3

Chapter 4

Direct Ink Writing of a Liquid Crystalline Ink to Fabricate Light-Responsive Actuators
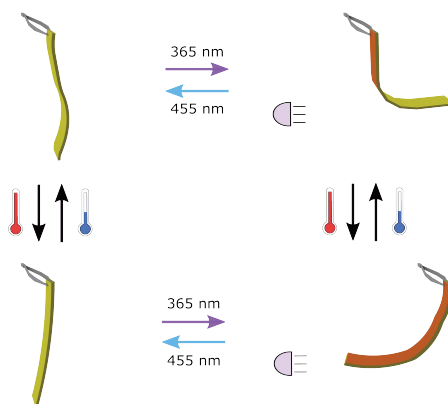
Abstract

Light-responsive liquid crystal (LC) polymers have been studied as promising materials for the fabrication of untethered soft actuators. Light is a versatile stimulus that can be rapidly and locally applied to trigger the desired response. This chapter describes a suitable LC ink for the fabrication of light-responsive amphibious LC-actuators via direct ink writing. The actuators present two deformation modes triggered by different stimuli. Temperature induces contraction/expansion and light induces bending/unbending. Unexpectedly, temperature can regulate the bending directionality, giving the material additional versatility to its deformation modes. These light-responsive actuators operate both in air and underwater.

4.1 Introduction

In recent years, the direct ink writing (DIW) of liquid crystal elastomer (LCE) has emerged as a promising approach to fabricate soft actuators in the centimeter scale that display distinct deformation modes.[1–10] To date, most LCE-based actuators fabricated via DIW have shown reversible temperature-triggered shape changes, but few example showed light-triggered motion.[11,12] Light is a versatile stimulus that can be rapidly and locally applied to control the movement of these actuators in an easy and rapid manner.[13,14] Light-responsive liquid crystals (LC) actuators have been previously obtained by introducing azobenzene photoswitches.[15,16] Although considerable progress has been achieved in photoactuation in air,[17–21] there are few examples of LC actuators that are responsive underwater.[22,23] Additionally, it has been shown that by utilizing humidity, the light response of a LC film can be enabled or disabled.[19] Furthermore, temperature can enhance the extent of motion[24] or reverse the directionality of the light-driven bending motion.[25] These examples demonstrate the potential of combining different stimuli-responses in a single material to increase the versatility and control of actuation. Thereto, it is interesting to explore and design new LC precursors to obtain light-fueled actuators active underwater and investigate the effect of other stimuli, such temperature, in their photoactuation.

In this chapter a LC-based ink for the fabrication of temperature- and light-responsive amphibious actuators via DIW is developed. The ink is first tested on fibers drawn from droplets on a glass surface, as this method has some similarities with respect to the DIW process. Photoactuation of the fibers showed an atypical bending away from the light source motion. We determined that the underlaying mechanism for this response is a smectic C (Sm C) to smectic A (Sm A) photoinduced phase transition. This LC ink was then used in a DIW equipment to fabricate a light-fueled underwater actuator. The planar aligned film contracted/expanded in response to temperature changes and bent away from the light source when illuminated at room temperature. Interestingly, when the film was photoactuated at ~60 °C in water, it bent towards the light source. This temperature-dependent directionality of the light-triggered bending motion is the result of the different LC phases obtained at different temperatures. As a result, a temperature-controlled light-induced bending of the film is achieved.

4.2 Results and Discussion

Light-Responsive Ink for Direct Ink Writing

A LC ink for the fabrication of amphibious light responsive actuators via DIW equipment needs to fulfill two critical parameters: (*1*) shear thinning to achieve control over the molecular alignment during printing[5,8] and (*2*) incorporation of a reactive azobenzene molecule as a crosslinker in order to get a photoresponse underwater,[23] preferably in the main chain oligomer since this enhances the extent of the photoactuation.[26] Taking these requirements into account, we modified an already reported ink for fiber drawing[24] by incorporating the azobenzene into the main chain LC oligomer (**Figure 4.1**). The chemical composition for the oligomer consists of reactive mesogens 1,4-bis-[4-(6-acryloyloxyhexyloxy) benzoyloxy]-2-methylbenzene (**1**), photoresponsive moiety 4,4'-bis(6-acryloyloxyhexyloxy) azobenzene (**2**), and isotropic chain extender 3,6-dioxa-1,8-octanedithiol (**3**). The acrylate-terminated main chain LC oligomer was synthesized via a base-catalyzed thiol-Michael addition reaction with a slight excess of acrylate versus thiol. After chain extension, the ^{1}H-NMR spectrum shows signals between 6.40-5.70 ppm, implying the presence of acrylate end groups. As evidenced in the gel permeation chromatography (GPC) spectrum, the characteristic absorption of *trans*-azobenzene peak at ~365 nm and the absorption of the other moieties at ~250 nm are at the same retention time, revealing that azobenzene molecules were indeed incorporated into the main chain oligomer. Based on GPC data, the weight average molecular weight was evaluated as ~18000 g mol^{-1}. Differential scanning calorimetry (DSC) traces and
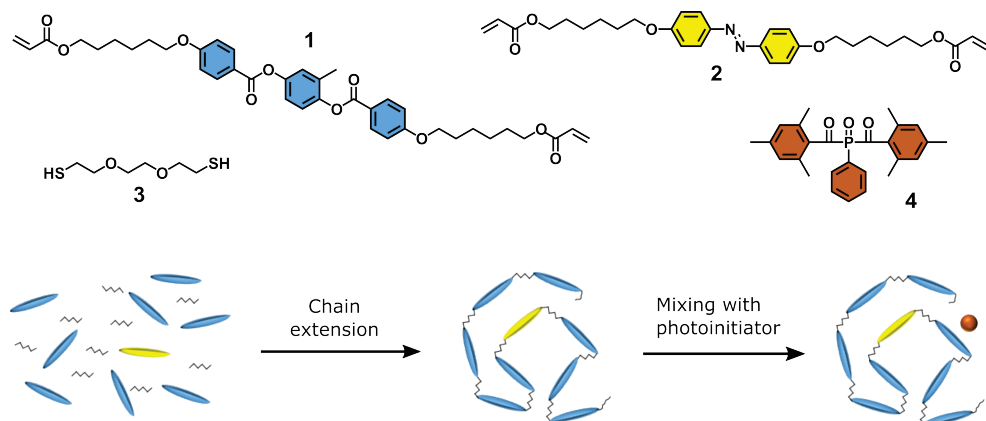

Figure 4.1. Preparation of ink and chemical composition used in the ink: the reactive mesogens (blue), azobenzene (yellow), di-thiol spacer (black) and photoinitiator (orange).
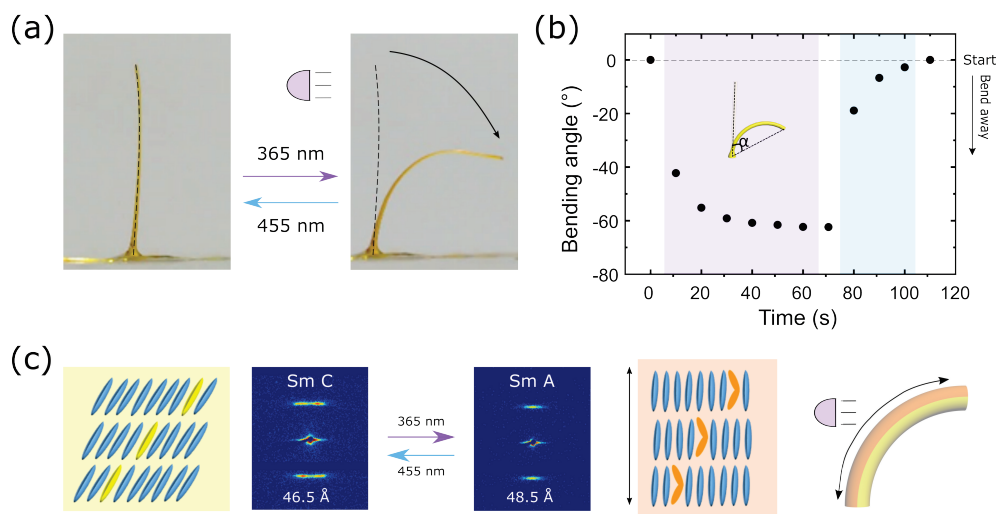
Figure 4.2. Photoactuation of a fiber. (a) Side views of bending and unbending behaviors after irradiation with 365 and 455 nm lights. (b) Bending angle as a function of irradiation time. Purple and blue regions indicate, respectively, the illumination with a 365 nm light and 455 nm light. The inset shows the definition of the bending angle used to characterize the motion of the standing fiber. (c) 2D-SAXS patterns and interpreted mesogen alignment of fibers at room temperature after illumination with 365 and 455 nm light.

crossed polarized microscopy showed a smectic to nematic phase transition temperature ($T_{Sm/N}$) centered at 49 °C and a nematic to isotropic phase transition temperature ($T_{N/I}$) at 81 °C.

Characterization of the photoactuation of the resulting LCE network was first performed by drawing fibers standing on a glass substrate using a previous reported procedure.[24] This fiber drawing method has many similarities with DIW (*vide infra*) with respect to precursor rheology, polymer properties after UV curing and response to light for actuation. The fibers had a diameter of ~120 μm and a length of ~9 mm. DSC traces of the fiber revealed a glass transition temperature (T_g) at ~ -16 °C and a broad $T_{N/I}$ centered at 74 °C. The photoactuation of the fibers was investigated in air, at room temperature, and under the illumination of both UV (365 nm, 75 mW cm^{-2}) and visible (455 nm, 30 mW cm^{-2}) lights. Unexpectedly, when exposed to UV light, the fibers bent away from the light source (**Figure 4.2a**). A maximum bending angle of ~ -62° was achieved within 60 s of UV irradiation (**Figure 4.2b**). Recovery to the unbent state was achieved by illuminating with visible light. These results show that here the effect of placing the azobenzene in the main chain oligomer does not only enhance the extent of the photoactuation at room temperature as

previously reported,[24] but it also revers the bending direction. This bending motion was reversible over 12 cycles of alternating UV and visible light exposures with no apparent signs of fatigue.[27]

LC actuators showing a directed motion away from the light source have been previously reported.[25,28] In one case, fibers presenting side-chain azobenzene photoswitches bent away from the light source as a result of a free-volume generation from the cis-isomer at the illuminated surface.[28] However, the current work employs the azobenzene as a crosslinker and this mechanism is therefore unlikely. In the other case, the uniaxial film that bent away from the light was the result of a photoinduced smectic (Sm) to nematic (N) transition that occurred at the illuminated surface.[25] A similar mechanism could be responsible for the hereto observed actuation directed away from the light source. Therefore, the mesogenic phase of a fiber under different illumination conditions was investigated by 2-dimensional small-angle X-ray scattering (2D-SAXS). As shown in **Figure 4.2c**, in the small angle region, we observed a typical Sm C pattern with four small lobes before irradiation. Upon illumination with UV light, the four diffraction arcs integrated into two diffraction arcs, revealing the formation of a Sm A phase. After light irradiation, the average layer spacing increased from 46.5 Å with a tilt angle of 13° to 48.5 Å with no tilt. Furthermore, the Sm C to Sm A phase transition was not visible in the temperature-dependent 2D-SAXS measurements, indicating that the phase transition was induced by the cis-azobenzene population formed by UV light illumination. The calculated ~4.3% layer spacing increase generated by the 2.0 Å increase in layer spacing photo-induced by the Sm C to Sm A phase transition is consistent with the macroscopic (roughly) 2.0% anisotropic length expansion observed by the illuminated surface, resulting in the observed bending motion. [27]

Direct Ink Writing of a Uniaxial Light-Responsive Polymer Film

The same LC ink was used for DIW to fabricate a uniaxial, light-responsive polymer film. The correlation between the alignment and the printing speed (2-13 mm s^{-1}) was investigated first**.** The printing temperature was set to 40 °C and the nozzle diameter was 335 µm. Lines printed at speeds < 6 mm s^{-1} displayed a non-variant brightness regardless of the orientation of the polarizer or analyzer, indicating different molecular orientations in the lines. Lines printed with speeds > 6 mm s^{-1} were darker when parallel to the polarizer or analyzer than when at 45°. Such dark-bright states are associated with an orientated LCE along the axis of the printed line, *i.e.* printing direction.[4,5] This was further confirmed by a supplementary optical characterization using the dichroism from the azobenzene. From this data, the optimal printing speed was set to 13 mm s^{-1}.

With the optimized printing parameters, we printed a single-layer film (5 x 20 mm²) on top of a glass substrate coated with polyvinylpyrrolidone (PVP) acting as sacrificial layer (**Figure 4.3a**). After photopolymerization at room temperature, the LCE-film between crossed polarizers was darker when the longitudinal axis of the film was parallel to the polarizer or analyzer than when the axis was at 45° (**Figure 4.3b**). This clearly indicated that the molecular orientation was achieved and successfully fixed, *i.e.* a planar LCE-film was fabricated via DIW. Using a contact profiling system, we determined the thickness of the film to be on average 78 µm. After optical and structural characterization, the film was detached from the glass substrate by dissolving the PVP layer to obtain a free-standing film. Finally, the DSC traces of the film showed a $T_{I/N}$ around 82 °C, a significantly broad $T_{N/Sm}$ centered at 44 °C and T_g at -25 °C, which is similar to the fibers.

Stimuli-Response of the Printed LCE-Film

Characterization in Air

We first investigated the temperature-triggered response of the film using an oven. As previously reported for planar LCE-films,[4,8] the film contracted along its long axis, parallel to the molecular director, and expanded perpendicular upon a temperature increase (**Figure 4.3c**). When plotting the longitudinal shrinkage ratio (L/L_0) as a function of temperature, different stages of the response were observed (**Figure 4.3d**). From 30 °C to ~40 °C, an increase of the film's length occurred due to the anisotropic thermal expansion. Then, a first actuation region was observed from ~40 °C until ~60 °C in which the film contracted because of the Sm C to N phase transition. A second actuation occurred from ~60 °C to ~80 °C, in which the film's length was further reduced due to the N to isotropic phase transition. The second one being steeper due to the reduced temperature range at which the N to isotropic transition occurs as seen in the DSC traces. At ~80 °C, the film was in its isotropic phase and reached its maximum contraction, being around 50 % of its initial length. From ~80 °C to 125 °C a slightly positive length increase was observed due to the thermal expansion of the network. When cooling to 30 °C the film recovered its initial length. The reversible temperature dependent anisotropic contraction/expansion further confirms a homogenous planar alignment and crosslink density through the thickness of the film.

To study the photoactuation, the printed LCE-film was clamped and hung on a stand. The film bent away from the light source as previously observed in the fibers (**Figure 4.4a**). Surprisingly, the response was obtained at lower light intensities; one order of magnitude smaller. We characterized the photoactuation by tracking the film's end-point displacement under different light intensities (**Figure 4.4b**) and over time **(Figure 4.4c)**. Increasing the light intensity increased the
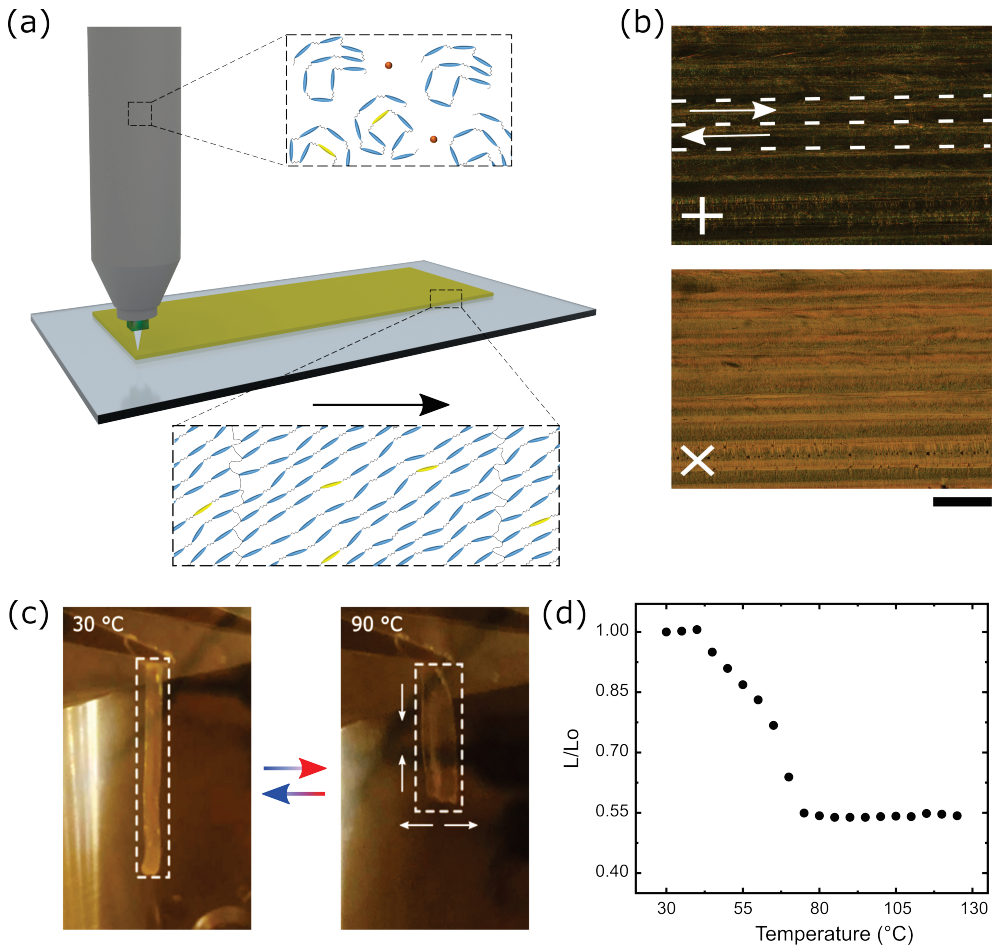
Figure 4.3. Overview of the fabrication and characterization of the printed LCE-film. (a) Scheme of the printed set-up showing the alignment of the molecules at each stage. (b) Polarized optical microscopy images of the printed film. The arrows indicate the printing direction and the dashed lines indicate the border of the lines that form the film. Scale bar represents 200 µm. (c) Front images of the film at 30 °C and at 90 °C showing the anisotropic response of the film, contracting along its long axis and expanding along its width. (d) Longitudinal shrinkage ratio (L/L_0) as a function of temperature. L represents the length of the film at a given temperature and L_0 the length at 30 °C.

maximum bending angle until a plateau was reached. The maximum bending angle was attained after 5 min of 365 nm light (1.1 mW cm^{-2}) illumination. We recorded the film's surface temperature with a high-speed thermal camera. No significant increase on temperature was observed during photoactuation, which indicates that the bending motion is mostly governed by photomechanical

effects. When the light was turned off, the film remained in the bent state due to the long lifetime of the *cis*-azobenzene moieties at room temperature.[23] Hence, different metastable bending angles could be obtained at different low light intensities. Reversion to the initial shape, through 455 nm light (0.8 mW cm^{-2}) irradiation, took around 1 min. It is worth mentioning that when the film was exposed from the other side, it still bent away from the light source. The actuation rate of the film was slower than the photoactuation in the fiber. We speculate that the difference arises from the different geometries, objects sizes, and the lower light intensity used to actuate the film. Finally, the reversibility of the photoactuation is demonstrated in **Figure 4.4d** in which after 10 cycles of alternating UV and visible light the films showed no signs of fatigue, similar to that
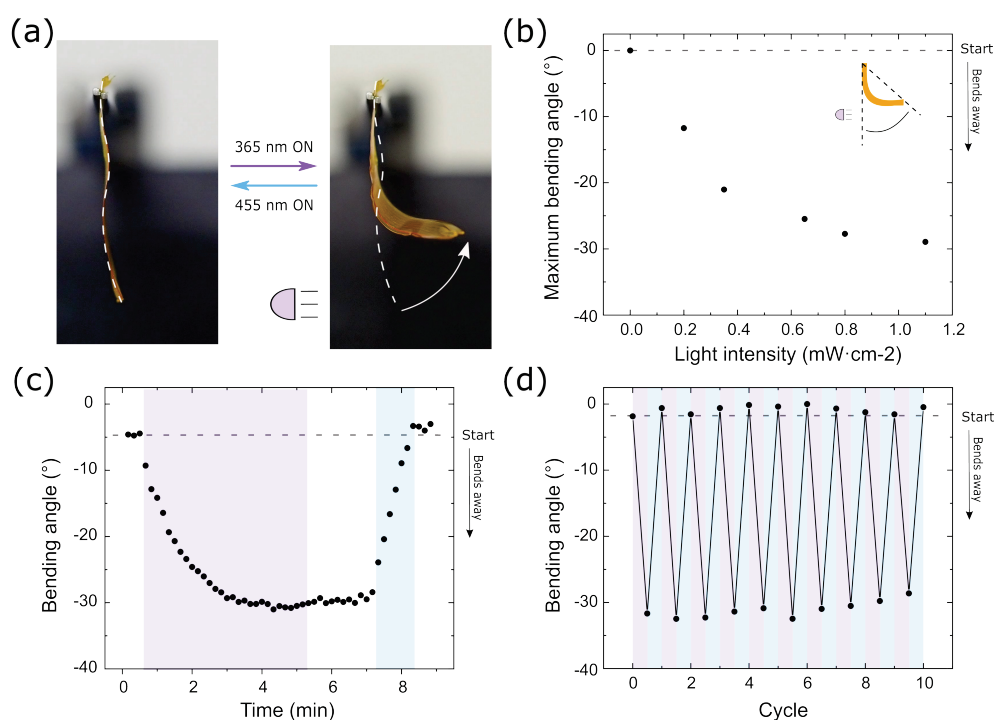
Figure 4.4. Photoactuation of the printed LCE-film in air. (a) Edge-on images showing the bending motion from the light of the film upon 365 nm or 455 nm light irradiation from the left. (b) Maximum bending angle obtained after 5 min of illumination with a 365 nm light at different intensities. The inset shows the definition of the bending angle used to characterize the motion of the film. (c) Bending angle as a function of time when illuminated with a 365 nm and 455 nm light. (d) Maximum bending angle of the film over ten successive cycles alternating illumination with 365 nm and 455 nm lights. For both (c) and (d), the purple and blue regions indicate, respectively, the illumination with a 365 nm light (1.1 mW cm^{-2}) and 455 nm light (0.8 mW cm^{-2}).

previously observed for the fibers. These results show that the printed LCE-film displays two different responses triggered by two distinct stimuli: light induces bending/unbending and temperature induces contraction/expansion.

Temperature-Dependent Phototactuation in Water

The underwater photoactuation was first studied by placing the hanging film in water at 20 °C, at which the polymer is in its Sm C phase (**Figure 4.5a**). Upon illumination with a 365 nm light (1.1 mW cm⁻²), the film bent away from the light source (**Figure 4b**). When the light was turned off, the film remained mostly bent, and slightly returned to its initial shape. Only when illuminated with 455 nm illumination (0.8 mW cm⁻²) did the film bend back to its initial state. The photoresponse in water at 20 °C showed a similar motion as in air while having a larger amplitude of actuation. If the thermal contribution to the back isomerization of the azobenzene moieties (*cis-trans*) is absent, as water acts as a heat sink, this might result in an overall higher *cis*-isomer population, hence in a larger actuation upon irradiation underwater in comparison with air.[22,36,37] Drag forces in water were not observed to have a negative influence on the actuation amplitude.

Furthermore, we investigated the photoresponse of the polymer network in its N phase by heating the water to 60 °C. Upon illumination with 365 nm light the film bent towards the light (**Figure 4.5b**). After turning the light off, the film slowly returned to its initial state unlike in the experiment at 20 °C where the film remained stationary. In this case, the elevated temperature most likely reduces the lifetime of the *cis*-isomers.[31] This reveals that it is difficult to keep the metastable state at higher temperature. Upon exposing the film to a 455 nm light, the film recovered faster to the unbent state which a reduced period between the illumination with 365 nm and 455 nm lights was used. In contrast to what occurs at room temperature (*vide supra*), at 60 °C the LCE-film is in its N phase and so isomerization of the azobenzene led to an increase of disorder in the network resulting in a contraction along the molecular axis and expansion perpendicular in the illuminated surface resulting in a bending motion towards the light motion.[32] It should be noted that the temperature dependent photoactuation was also observed for the drawn fibers showing that the atypical response is related to the light responsive ink.

The temperature-dependent photoactuation of the films was further tracked by cooling the water from 60 °C to 20 °C while maintaining a constant UV light illumination (**Figure 4.5c**). At 60 °C, the film bent towards the light source. While decreasing the temperature from 60 °C to ~47 °C the film maintained a constant deformation. Upon further cooling from ~47 °C to 30 °C,

4
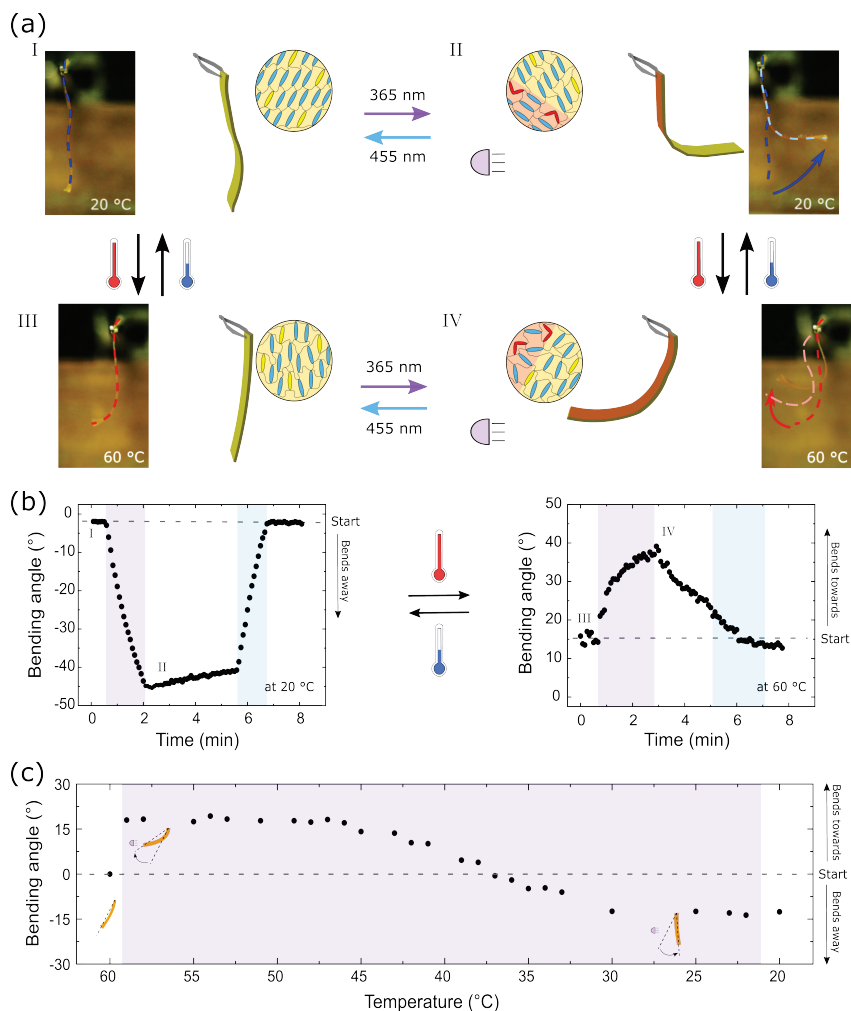
Figure 4.5. Temperature-dependent photoactuation of the printed LCE-film in water. (a) Schematic representation and side-on images of the film during actuation as a response of two different stimuli: light and temperature. Temperature changes the LC phase of the film, from Sm C to nematic or vice versa. In the Sm C phase at low temperature, the film bends away from the light source. At high temperatures, in the nematic phase, the film bends towards the light source. Also, at elevated temperature the presence of convection flow, from right to left, changes slightly the initial shape of the film. (b) Bending angle as a function of irradiation time for a film at 20 °C (left) and 60 °C (right). The bending angle is defined in the inset in **Figure 4.4b**. (c) Photoactuation of the film in water at various temperatures while under continual 365 nm light exposure. In this case the starting position is set as the zero for the bent state, as shown in the left inset drawing. The other two schemes show the bend of the film at different temperatures with respect to the starting position. For both (b) and (c), the purple and blue regions indicate, respectively, the illumination with a 365 nm light (1.1 mW cm^{-2}) and 455 nm light (0.8 mW cm^{-2}).

the LCE network underwent a gradual phase transition from N to Sm, resulting in an expansion along the long axis of the illuminated part of the film. Consequently, during this temperature range the film bent away from the light source. Below 30 °C, the film maintained a constant deformation, even when the light was turned off. As a result, the bending angle in the planar aligned film was reversed by decreasing the temperature from 60 °C to 20 °C. Recovery to the unbent state was achieved by illumination with 455 nm light at 20 °C. These results show that different mechanisms govern the photoactuation of the LCE network at different temperatures and so the light-driven bending direction of the film can be controlled by tuning the temperature at which it is illuminated.

4.3 Conclusions

This chapter describes the development of a LC oligomeric ink for the DIW fabrication of amphibious light-fueled actuators. Remarkably, the light-triggered bending directionality can be regulated by temperature. When illuminated at room temperature, the LCE actuators undergo a light-induced phase transition from Sm C to Sm A that results in a motion directed away from the light source. Whereas when illuminated at elevated temperatures (>45 °C), the same actuator actuates towards the light source. These results show a new approach to control the photoinduced deformations in light-fueled 3D actuators through additive manufacturing that operate both in air and underwater. In the next chapter, we will focus on actuators partially cover by the LC ink produced in this chapter. The actuators will be fabricated by direct ink writing and can be made multi-functional.

4.4 Experimental Details

Materials and Regeants

1,4-Bis-[4-(6-acryloyloxyhexyloxy) benzoyloxy]-2-methylbenzene (**1**) was purchased from Merck. 4,4'-Bis(6-acryloyloxyhexyloxy) azobenzene (**2**) was purchased from Synthon. 3,6-dioxa-1,8-octanedithiol (**3**, DODT) and 1,8-Diazabicyclo[5.4.0]undec-7-ene (DBU) were obtained from Sigma Aldrich. Base catalyst triethylamine (TEA) was obtained from Acros. Photoinitiator Irgacure 819, was purchased from Ciba. Polyvinylpyrrolidone with an average molecular weight of 40000 g/mol was purchased from Sigma Aldrich. Solvent, dichloromethane (DCM) was obtained from Biosolve.

Characterization

^{1}H-NMR spectra were collected on a 400 MHz Bruker Advance III HD spectrometer with chloroform as solvent. GPC with was performed to evaluate the number average molecular weight (M_n), weight average molecular weight (M_w), and polydispersity index (PDI) of oligomers. Shimadzu apparatus was used for the GPC measurements using and the reference was polystyrene (PS) with an average M_w of 350,000 g mol^{-1}. DSC measurement was employed to determine the transition temperature of oligomers and fibers in a TA Instruments DSC Q1000. 2D-SAXS measurements were conducted on a Ganesha lab instrument with a GeniX-Cu ultralow divergence source producing X-ray photons equipped with a wavelength of 1.54 Å and a flux of 1×10^8 photons/s. A Pilatus 300 K silicon pixel detector with 478×619 pixels, each 172 µm^2 in size was utilized to collect scattering patterns. All microscopy images were taken from a Leica DM 2700M equipped with two polarizers that were operated either crossed or parallel, and a Linkam TMS 600 hotstage. The thickness of the film was determined via a contact profile system, DektakXT from Bruker.

Preparation of the Ink

The oligomer was synthesized via a base-catalyzed thiol-acrylate Michael addition reaction. First, diacrylate mesogen **1**, diacrylate azobenzene **2**, and dithiol chain extender **3** were added in a flask and dissolved in DCM. After mixing, TEA was slowly added to the solution. For large scale reactions, DBU was used instead of TEA.[27] The mixture was reacted at 38 °C overnight. Then, DCM was added to the flask to dilute the mixture and washed with 1M HCl (2 x) and saturated brine (1 x) to remove the existing TEA. The organic phase was collected and dried with MgSO$_4$. Subsequently, most of solvent was removed by a rotary evaporator in filtrate. The removal of the residual solvent was conducted in a vacuum oven at room temperature. Finally, the oligomer (98 wt%) was mixed with the photoinitiator (2 wt%) in DCM. The ink was obtained after removing the solvent at room temperature under vacuum.

Fabrication of Standing Fibers

In general, the fibers were fabricated via a drop casting/drawing technique as previously reported.[24] The ink was dissolved in DCM (270 mg mL^{-1}) at room temperature. Droplets with 10 µL solution were cast on a glass substrate (3×3 cm^2) and heated at 60 °C for 30 min to remove the solvent. After that, the substrate supporting the droplets was gently contacted by another glass plate from above. Fibers were obtained from the viscous droplets after two glass plates were pulled apart 1.25 cm. The randomly oriented mesogens were uniaxially aligned along the

longitudinal direction due to the elongational flow of the drawing process. The homogeneously oriented mesogens were subsequently photocrosslinked under nitrogen atmosphere with an Exfo Omnicure S2000 light source in which 57% of the light intensity has a wavelength of 395-445 nm and 43% of 320-390 nm. A light filter was utilized to block wavelengths below 405 nm, limiting the formation of *cis*-isomerized azobenzene. After photocrosslinking for 1 h, standing fibers on the glass substrate were achieved after cutting the fiber tops with a scissor and removing the top glass plate.

Direct Ink Writing

The printing process was performed using a commercial 3D printer (EHR, Hyrel 3D). The ink was loaded into the stainless-steel reservoir at room temperature and extruded using a nozzle diameter of 335 μm at 40 °C. The printing speed ranged between 2-13 mm s^{-1}, being 13 mm s^{-1} the optimal one. A film (5 × 20 mm²) was printed on top of a PVP coated glass. The printing path was controlled by a G-code generated by the printer software. After printing, photopolymerization was induced using an Exfo Omnicure S2000 light source in which 57% of the light intensity has a wavelength of 395-445 nm and 43% of 320-390 nm. A light filter was utilized to block wavelengths below 405 nm, limiting the formation of *cis*-isomerized azobenzene. After exposure for 2 h, in which the sample was flipped every 30 min, the film's thickness and birefringence was characterized via a profiling system and a microscope respectively. To obtain a free-standing film, the PVP layer was dissolved by immersing the sample in water at room temperature and subsequently dried at room temperature overnight.

Photoactuation of the Fibers and the Film

Fibers and film, either standing or hanging, were placed at 21.0 cm distance from collimated UV light (365 nm, Thorlabs M365L2) and visible light (455 nm, Thorlabs M455L3-C2). A controller (ThorLabs DC4104) was used to tune the intensity of the lights. All objects were illuminated with the 455 nm light before performing the photoactuation to ensure that all azobenzene molecules were in the *trans*-isomer. We used a camera (Nikon D7200, Olympus OM-D E-M10 Mk III) to record the light-driven deformation. The temperature of the surface of the film was controlled using a Gobi camera from Xenics. Underwater actuation was conducted inside a transparent container with flat sides that was filled with water either at 20 °C or at 60 °C. The temperature of the water was controlled using a digital thermometer.

4

4.5 References

1   M. O. Saed, C. P. Ambulo, H. Kim, R. De, V. Raval, K. Searles, D. A. Siddiqui, J. M. O. Cue, M. C. Stefan, M. R. Shankar and T. H. Ware, *Adv. Funct. Mater.*, 2019, **29**, 1806412.

2   D. J. Roach, X. Kuang, C. Yuan, K. Chen and H. J. Qi, *Smart Mater. Struct.*, 2018, **27**, 125011.

3   Y. Zhang, L. Huang, H. Song, C. Ni, J. Wu, Q. Zhao and T. Xie, *ACS Appl. Mater. Interfaces*, 2019, **11**, 32408–32413.

4   M. López-Valdeolivas, D. Liu, D. J. Broer and C. Sánchez-Somolinos, *Macromol. Rapid Commun.*, 2018, **39**, 1700710.

5   C. P. Ambulo, J. J. Burroughs, J. M. Boothby, H. Kim, M. R. Shankar and T. H. Ware, *ACS Appl. Mater. Interfaces*, 2017, **9**, 37332–37339.

6   A. Kotikian, C. McMahan, E. C. Davidson, J. M. Muhammad, R. D. Weeks, C. Daraio and J. A. Lewis, *Sci. Robot.*, 2019, **4**, eaax7044.

7   G.-Z. Yang, R. J. Full, N. Jacobstein, P. Fischer, J. Bellingham, H. Choset, H. Christensen, P. Dario, B. J. Nelson and R. Taylor, *Sci. Robot.*, 2019, **4**, eaaw1826.

8   A. Kotikian, R. L. Truby, J. W. Boley, T. J. White and J. A. Lewis, *Adv. Mater.*, 2018, **30**, 1706164.

9   C. Zhang, X. Lu, G. Fei, Z. Wang, H. Xia and Y. Zhao, *ACS Appl. Mater. Interfaces*, 2019, **11**, acsami.9b18037.

10 J. del Barrio and C. Sánchez-Somolinos, *Adv. Opt. Mater.*, 2019, **7**,1900598.

11 L. Ceamanos, Z. Kahveci, M. López-Valdeolivas, D. Liu, D. J. Broer and C. Sánchez-Somolinos, *ACS Appl. Mater. Interfaces*, 2020, **12**, 44195–44204.

12 X. Lu, C. P. Ambulo, S. Wang, L. K. Rivera-Tarazona, H. Kim, K. Searles and T. H. Ware, *Angew. Chemie Int. Ed.*, 2021, **60**, 5536–5543.

13 H. K. Bisoyi and Q. Li, *Chem. Rev.*, 2016, **116**, 15089–15166.

14 M. Pilz da Cunha, S. Ambergen, M. G. Debije, E. F. G. A. Homburg, J. M. J. den Toonder and A. P. H. J. Schenning, *Adv. Sci.*, 2020, **7**, 1902842.

15 T. J. White, *J. Polym. Sci. Part B Polym. Phys.*, 2018, **56**, 695–705.

16 H. Yu and T. Ikeda, *Adv. Mater.*, 2011, **23**, 2149–2180.

17 R. C. P. Verpaalen, S. Varghese, A. Froyen, M. Pilz da Cunha, M. J. Pouderoijen, J. R. Severn, M. R. Bhatti, T. Peijs, C. W. M. Bastiaansen, M. G. Debije, T. A. P. Engels and A. P. H. J. Schenning, *Matter*, 2020, **2**, 1522–1534.

18 M. Pilz da Cunha, Y. Foelen, R. J. H. van Raak, J. N. Murphy, T. A. P. Engels, M. G. Debije and A. P. H. J. Schenning, *Adv. Opt. Mater.*, 2019, 1801643.

19 O. M. Wani, R. Verpaalen, H. Zeng, A. Priimagi and A. P. H. J. Schenning, *Adv. Mater.*, 2018, **1805985**, 1805985.

20 O. M. Wani, H. Zeng and A. Priimagi, *Nat. Commun.*, 2017, **8**, 1–7.

21 A. H. Gelebart, D. Jan Mulder, M. Varga, A. Konya, G. Vantomme, E. W. Meijer, R. L. B. Selinger and D. J. Broer, *Nature*, 2017, **546**, 632–636.

22 H. Shahsavan, A. Aghakhani, H. Zeng, Y. Guo, Z. S. Davidson, A. Priimagi and M. Sitti, *Proc. Natl. Acad. Sci. U. S. A.*, 2020, **117**, 5125–5133.

23 M. Pilz da Cunha, E. A. J. van Thoor, M. G. Debije, D. J. Broer and A. P. H. J. Schenning, *J. Mater. Chem. C*, 2019, **7**, 13502–13509.

24 A. H. Gelebart, M. Mc Bride, A. P. H. J. Schenning, C. N. Bowman and D. J. Broer, *Adv. Funct. Mater.*, 2016, **26**, 5322–5327.

25 Y. Zhang, J. Xu, F. Cheng, R. Yin, C. C. Yen and Y. Yu, *J. Mater. Chem.*, 2010, **20**, 7123–7130.

26 L. Liu, M. Pozo, F. Mohseninejad, M. G. Debije, D. J. Broer and A. P. H. J. Schenning, *Adv. Opt. Mater.*, 2020, 2000732.

27 M. del Pozo, L. Liu, M. Pilz da Cunha, D. J. Broer and A. P. H. J. Schenning, *Adv. Funct. Mater.*, 2020, **30**, 2005560.

28 Z. Cheng, S. Ma, Y. Zhang, S. Huang, Y. Chen and H. Yu, *Macromolecules*, 2017, **50**, 8317–8324.

29 M. Pilz da Cunha, H. S. Kandail, J. M. J. den Toonder and A. P. H. J. Schenning, *Proc. Natl. Acad. Sci.*, 2020, 202004748.

30 R. C. P. Verpaalen, M. Pilz da Cunha, T. A. P. Engels, M. G. Debije and A. P. H. J. Schenning, *Angew. Chemie Int. Ed.*, 2020, **59**, 4532–4536.

31 A. H. Gelebart, D. J. Mulder, M. Varga, A. Konya, G. Vantomme, E. W. Meijer, R. L. B. Selinger and D. J. Broer, *Nature*, 2017, **546**, 632–636.

32 C. L. van Oosten, K. D. Harris, C. W. M. Bastiaansen and D. J. Broer, *Eur. Phys. J. E*, 2007, **23**, 329–336.

Chapter 5

Direct Ink Writing of Soft Actuators Partially Covered with Liquid Crystal Elastomers
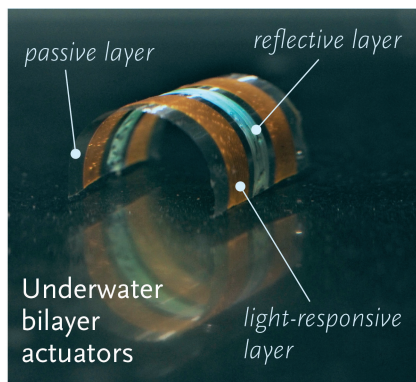
Abstract

Direct ink writing (DIW) of liquid crystal polymers has resulted in actuators capable of performing complex shape changes. Multi-functional soft actuators, however, despite being much desired remains challenging. This chapter elucidates on the usage of DIW as a fabrication method for soft actuators that have additional functionalities and that perform atypical reversible shape deformations. The key is to use DIW to partially cover the passive layer and create discrete responsive regions. As a result, by individually and sequentially illuminating active layers, left and right twisting and bending in perpendicular directions can be generated in a single film. Furthermore, the partial coverage also allows for the combination of different functional materials in one object, as shown by fabricating a light-responsive green reflective actuator. These results serve as a toolbox for the design and fabrication of untethered functional soft actuators with multi-tasking capabilities.

5.1 Introduction

Over the past decade, the advent the additive manufacturing (AM) of stimuli-responsive materials has made substantial contributions towards realizing untethered 3D centimeter-scale actuators.[1–4] Direct ink writing (DIW) of liquid crystals elastomers (LCEs) has brought unprecedented control over the molecular director within the body of the actuator resulting in devices that may perform complex tasks including self-propulsion,[5] sequential folding,[6] weight lifting,[7,8] grasping,[9] formation of dynamic Braille patterns,[10] and controlled focus of a lens.[11] However, these LC actuators are mostly monofunctional and programmed to execute a single task.[1] Multitasking, which is ubiquitous in nature, would be much preferred and bring untethered soft actuators one step closer to widespread use.[12–16] For a single actuator to perform multitasking, it should be able to display various distinctive deformations on-demand.[5,10,17,18] Realizing this in LC actuators has been accomplished by sequentially activating individual parts of the body[5,6,10] or triggering different deformations using various stimuli.[9,10,12,19] Following these approaches, film assemblies have been reported that can transport cargos[17] or that can attract and catch floating droplets underwater.[16] While these constructs show great potential at multitasking, they rely on assembling different parts to build a functional object, typically requiring several steps. A fabrication method that could produce actuators that can multitask in one go would be much preferred.

In this chapter, we present light-responsive underwater bilayers actuators fabricated via DIW that display several controlled deformations modes on-demand. Using the LC ink described in **Chapter 4**, a bilayer film with only partial coverage of its passive layer by LCE is first presented and characterized. Interestingly, large deformations in opposing directions were triggered by light and temperature. This finding was used to fabricate actuators displaying different reversible and controlled shape deformations upon specific illumination of the different discrete light-responsive regions spread across the passive layer. The partial coverage of a passive substrate with active material gives the potential benefits of partial transparency for DIW deposition of additional layers, for example photonic reflectors. In this latter case, we present an actuator capable of performing two tasks: multidimensional movement and selective reflection of green light.

5.2 Results and Discussion

Generating Light-Responsive Soft Actuators Partially Covered

The partially covered light-responsive liquid crystals actuators were prepared by DIW. The possibility of depositing the liquid crystals via DIW facilitates control of the alignment of the
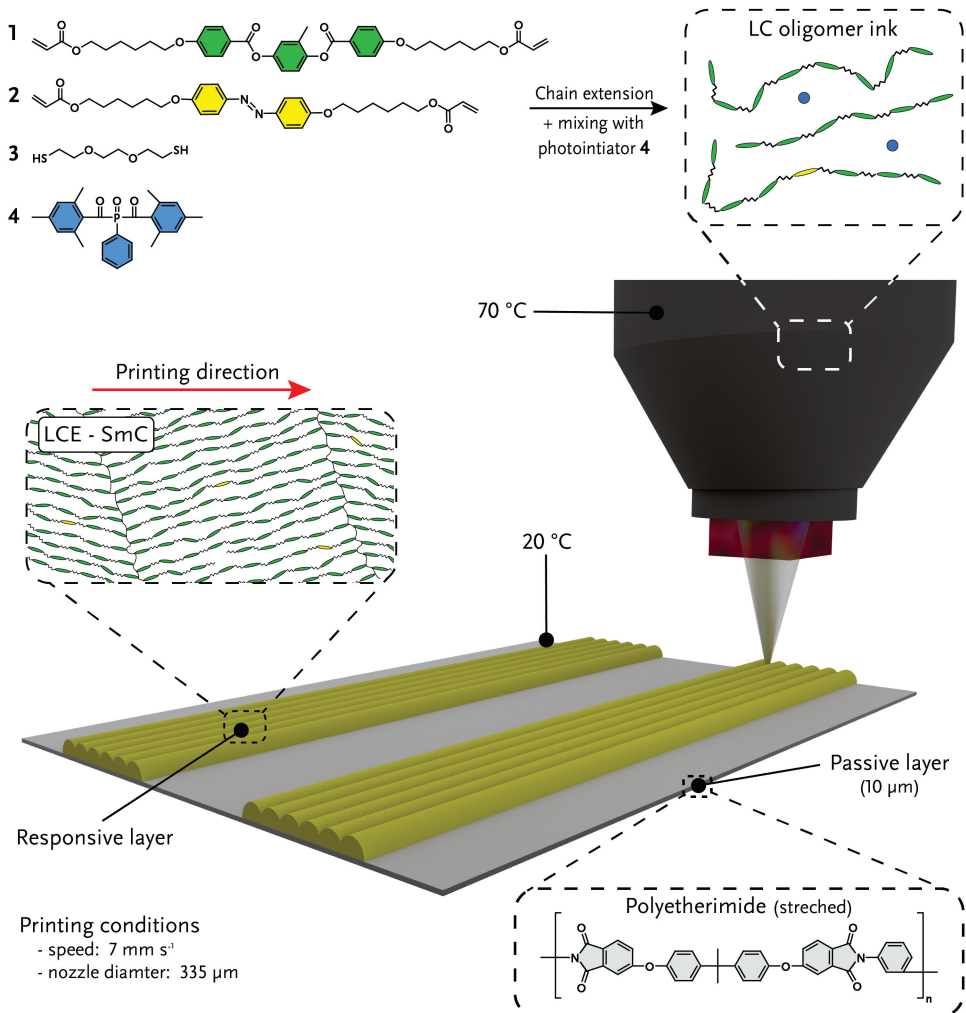

Figure 5.1 Scheme depicting the synthesis of the LC ink (top) and the fabrication process of LC-based bilayer via DIW (bottom). The LC-oligomer used to prepare the ink is the result of the chain extension, via a Michael-thiol addition, of molecules **1-2** using **3** as a spacer. The insets show the molecular alignment at each stage.
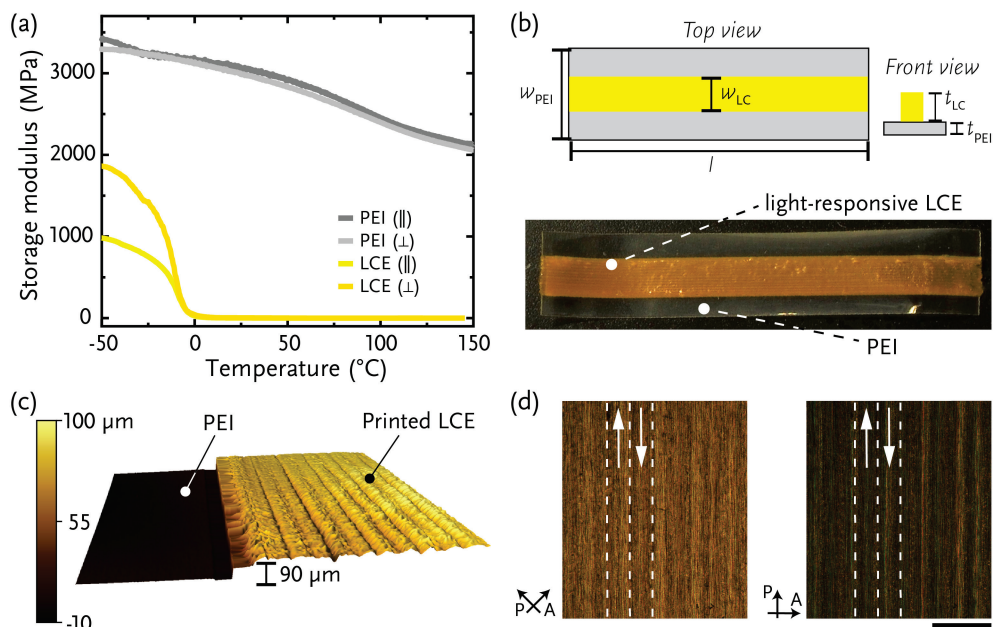
Figure 5.2 Characterization of the bilayer film prepared via DIW. (a) Storage modulus as a function of temperature of the two layers separately. The modulus was investigated parallel (‖) and perpendicular (⊥) to the alignment direction of the LC and to the stretching direction of the PEI foil. (b) A schematic representation of a bilayer film in which the different tunable design parameters are defined (top). Yellow and light grey represents the LCE and the PEI respectively. (Bottom) an image of a fabricated film, 5 × 25 mm^2 with a 40% coverage. (c) 3D profile of the edge of the printed LCE. (d) Crossed polarized light micrographs of the printed LCE on the foil. The black arrows represent the direction of the polarizer (P) and analyzer (A). The white dashed lines indicate the borders of the printed lines. The white arrows indicate the direction of printing. The scale bar represents 500 µm.

mesogens,[8,11] key to pre-programming the actuator's performance (**Figure 5.1**).[1] This fabrication approach reduces the coverage area of active material, permitting the creation of discrete, responsive regions that can be independently triggered.[11] We selected a 10 µm thick polyetherimide (PEI) foil as the passive layer. The PEI foil is uniaxially stretched and has nanogrooves, although there is no indication that stretched PEI acts as an alignment layer for mesogens (*vide infra*). PEI is transparent to blue light, but not to UV-light. Most importantly, it is very thin, 10 µm, with a storage modulus at 20 °C (~3000MPa, **Figure 5.2a**) on the same order of magnitude as polydimethylsiloxane (PDMS) and poly(ethylene terephthalate) (PET),[20–22] used previously to make light-responsive bilayer actuators. The LC ink suitable for the DIW process was prepared as described in **Chapter 4** by mixing LC-oligomers (98wt.%) containing azobenzene moieties with a photoinitiator

(2 wt.% **4**) (**Figure 5.1**). In this chapter, a new batch of the LC-oligomer was synthesized as previously reported in **Chapter 4** via the base-catalyzed thiol-Michael of molecules **1-2** using **3** as a spacer. The synthesized oligomer had a number average molecular weight (M_n) of 7756.6 g mol^{-1} based on the ^{1}H-NMR spectrum with a polydispersity index (PDI) of 2.4 as determined by gel permeation chromatography (GPC). The LC-oligomer showed isotropic to nematic phase transitions ($T_{I/N}$) at 80 °C and nematic to smectic C phase transitions ($T_{N/SmC}$) at 42 °C, as indicated by the differential scanning calorimetry (DSC) traces and crossed polarized light micrographs.

Before fabricating actuators via DIW that are partially covered with the light-responsive LC inks, the printing process on PEI foils was optimized. The influence of the printing direction, either parallel or perpendicular to the stretching direction of the PEI, on the eventual mesogenic alignment was investigated first. The reservoir was set to 70 °C and the printing bed to 20 °C. At these temperatures, printing with a speed of 7 mm s^{-1} with a 335 μm diameter nozzle invariably resulted in uniaxially aligned lines, independent of the underlying PEI stretching direction. These results verify the PEI foil is not acting as an alignment layer, and the mesogenic alignment is determined solely by the DIW process. After printing, formation of the LCE network was accomplished using high intensity UV-light at room temperature under N$_2$. Sol/gel fraction experiments revealed an average 85% gel fraction. Copolymerization of acrylate groups generally results in higher fractional network formations, but the high viscosity and long oligomeric chains (~9 units) of this system reduce the mobility of the radicals and lower the crosslink density, respectively, resulting in a lower fraction of gel.

With printing parameters optimized, we deposited a single 2 × 35 mm^2 LCE stripe on a PEI foil (10 × 10 × 0.001 cm^3). After photopolymerization, a laser cutter was employed to obtain a 5 × 25 mm^2 film with the LCE rectangle situated along the center of the PEI (**Figure 5.2b**). As a result, the PEI film had 40% of its area covered by the LCE. The thickness of the LCE was on average 90 μm as determined by an optical profiling system (**Figure 5.2c**). Across the 3D profile, the active area shows a wave-like topography; each "wave" representing one of the deposited filaments that constitute the LCE stripe. The birefringence of the active layer was then observed between crossed polarizers (**Figure 5.2d**). The film appeared darker when oriented parallel to the polarizers or analyzer than when at 45°. This dark-bright state is linked with uniaxially orientated LCE:[1] in this case, the mesogenic alignment was parallel to the longitudinal axis.

5

Temperature and Light Response

The response of the 5 × 25 mm[2], 40% covered, 90 μm LCE film (**Figure 5.2b**) to different stimuli was characterized. First, the temperature response was evaluated (**Figure 5.3a**). Upon increasing temperature from 25 °C to 80 °C, the film initially bent, and then tightly rolled up between 80°C - 110 °C, with the LCE inside the curvature. Such a response is not surprising because uniaxially aligned LCEs are known to display large, anisotropic shape deformations (∼Δ50 %), contracting along and expanding perpendicular to the alignment direction.[1,23] The temperature-response arises from increasing disordering of the mesogenic groups with increasing temperature as the network undergoes several phase transitions, as seen in the temperature response of the printed LCE film in **Chapter 4**. Bare PEI itself does not show any shape changes within the evaluated temperature range. Hence, as previously observed for bilayers, when one of the layers experiences a contraction or expansion along the longitudinal axis the system bends parallel or perpendicular to it, respectively.[24] Thanks to the large contraction of LCEs, the film's final configuration is a tight roll. In comparison, liquid crystalline networks (LCN) bilayer films (LCNs characteristically having a greater crosslink densities than LCEs and 10% contraction)[1,23] typically only bend up to a full rotation,[25] and generally do not tightly roll up unless they have a wedged geometry.[26]

Photoactuation of a bilayer can be characterized either in air or underwater, since the chosen LCE performs in either of these mediums, as demonstrated in **Chapter 4**. In air, both photome-chanical and photothermal effects influence the actuation of LC networks, while underwater only the photomechanical influences the motions.[27] Here, since the LCE has a temperature-dependent directionality of the light-driven bending motion, systematic studies of the photoactuation in air can be difficult. Therefore, photoactuation was investigated underwater where only photomechan-ical effects occur. The 5 × 25 mm[2], 40% covered, 90 μm LCE bilayer film (**Figure 5.2b**) was sus-pended in 19°C water: at this temperature the polymer is in its SmC phase. When irradiated with 365 nm light (80 mW cm^{-2}) the illuminated region underwent a photoinduced SmC to SmA phase transition, resulting in a ∼4.3% expansion along the longitudinal axis (see **Chapter 4**) and conse-quent bending of the film away from the light source (**Figure 5.3b**). A stationary state was reached after 10 min of illumination, at which that point the light was switch off. Due to the photomechan-ical nature of the response, the deformation was only reversed when illuminated with a 455 nm
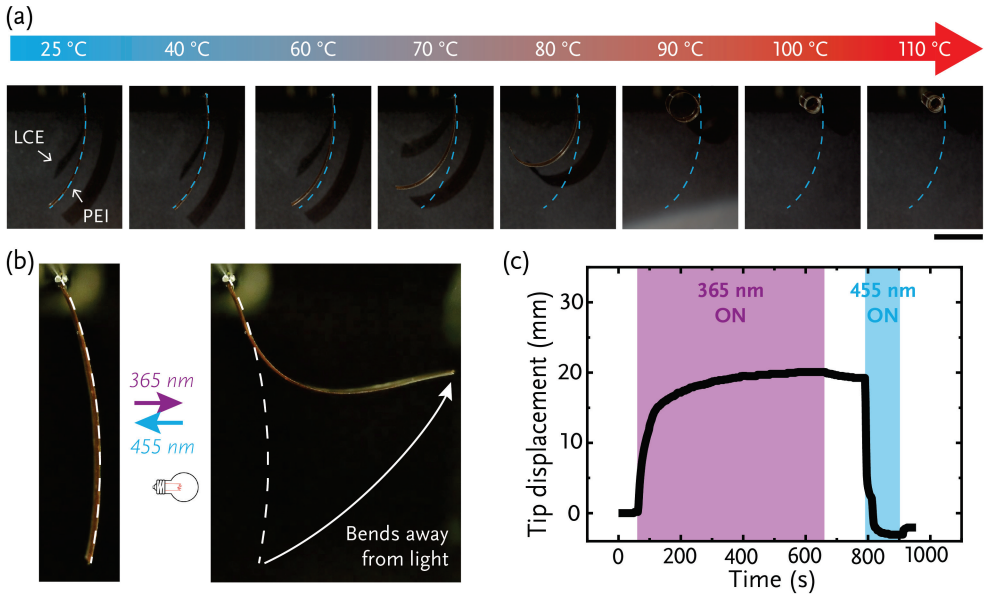
Figure 5.3 Stimuli response of a bilayer actuator (5×25 mm², 40% coverage, 90 μm of LCE on PEI, **Figure 5.2b**). (a) Edge-on images of the film at different temperatures. The blue dashed lines represent the shape of the film at 25°C. Scale bar represents 1 mm. (b) Edge-on images displaying the light-driven bending motion of the bilayer film to 365 nm (80 mW cm⁻²) and 455 nm light (145 mW cm⁻²). (c) Tip displacement as a function of time. Positive values mean that the tip bent away from its starting position, *i.e.* from the light source, and negative when bent towards the light.

light (145 mW cm⁻²), which induced the back isomerization from *cis* to *trans* (**Figure 5.3c**). This bending motion was reversible for at least 12 cycles with no apparent signs of fatigue. The film, despite being only 40% covered with the active material, showed a large light-driven deformation, with maximum tip displacement of 25 mm. A similar performance was observed for a film that had the stretching direction of the PEI foil perpendicular to the printing direction rather than parallel. The observed tip displacement is comparable to those previously reported for non- and bilayer films having similar dimensions with 100% surface area coverage by active material where the maximum light-driven deformation ranged from 18-26 mm.[16,20–22,27] This result suggests that large deformation can be obtained without fulling covering the passive layer with active material, inspiring new designs of actuators to unlock their full potential.

5

Influence of Thickness, Shape, and Coverage on the Photoactuation

There are three tunable parameters in the bilayer actuator: the thickness of the active LCE (t_{LC}), the fractional coverage of the passive PEI, and the aspect ratio of the film. The effect of each of variable on the maximum tip displacement was systematically studied. We observed that in some cases the films showed a pre-bend when suspended. The pre-bend could be caused by a gradient on the crosslink density of the LCE, but free-standing films of the LCE polymerized under the same conditions did not show such pre-bends, as seen in **Chapter 4**, and so we reject this possibility. We hypothesize that the pre-bend is a consequence of the high temperature achieved during the laser cutting, since bare laser cut PEI films having the same dimensions also showed pre-bends: a linear relationship between pre-bend and laser intensity was observed.

The influence of the thickness, t_{LC}, of the active LCE layer on photoactuation was investigated in a series of films in which the dimensions (5 × 25 mm²) and fractional coverage (40%) of the passive PEI layer were kept constant. Upon increasing t_{LC} from 50 μm to 150 μm, the maximum tip displacement recorded after 10 min of illumination with a 365 nm light increased consistently until it reached a maximum value at a thickness of 95 μm, at which point it decreased. Effectively, when the LCE layer is illuminated, two regions are formed through the depth of the LCE layer: the exposed region at the surface expands along the longitudinal axis and the non-exposed regions

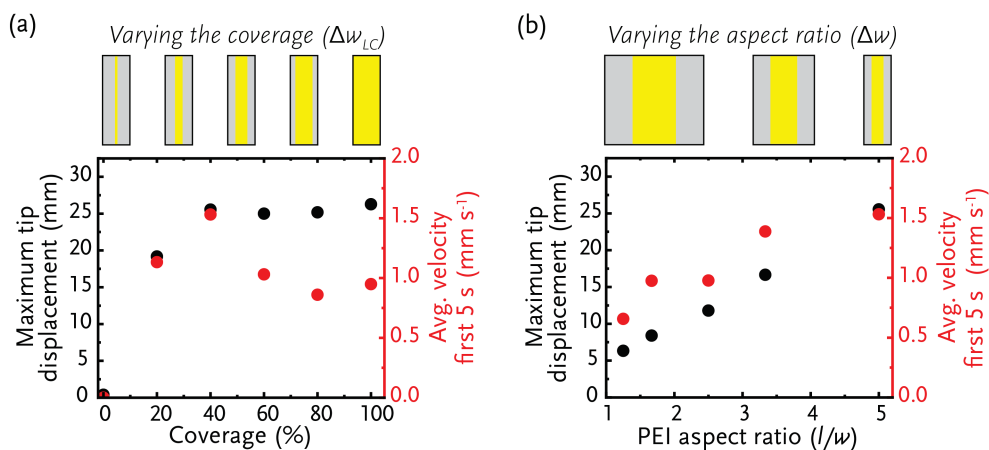**Figure 5.4** Maximum tip displacement and average velocity after 5s of illumination as a function of the percentage of (a) LCE coverage and (b) PEI aspect ratio of films with 40% LCE coverage respectively. In both cases the illumination time with 365 nm (80 mW cm⁻²) was 10 min. Above the plots, schematics representation of some of the films used for the studies. Yellow indicates the LCE and light grey represent the PEI.

that are deeper remains passive. The extent of the expanding region depends on several factors (such as the illumination time, light intensity and azobenzene concentration, among others). Thin LCE layers mean that its entire depth is exposed and the whole LCE expands in its entirety. Further increasing t_{LC}, increments the dark region within the LCE layer which in turns augments the bending stiffness of the actuator too, reducing the maximum tip displacement as it is inversible correlated with the thickness of the passive layer to the third power.[21] The resulting optimal thickness of LCE for maximum tip displacement is determined for our specific illumination conditions.

We investigated the effect of fractional coverage in the photoactuation in a series of films having identical dimensions (5×25 mm^2) and deposited LCE thicknesses (90 μm) (**Figure 5.4a**). By increasing coverage from 0 to 100%, the maximum tip displacement plateaued at ~40% coverage. The rate of actuation during the initial 5 seconds was roughly linear, and appears to peak at 40% coverage, decreasing to a roughly constant value at higher coverages. This suggests a minimum coverage is required to initiate rapid, extensive actuation: the degree of coverage required will be affected by the physical characteristics of the passive and active layers and well as the illumination conditions, the illuminated region expanding perpendicular to the alignment (~4.3%; see **Chapter 4)**, and contracting perpendicular (~2%). When increasing the fraction of LCE, the width of the line increases, resulting in increasingly significant perpendicular expansion and generation of orthogonal stresses that opposes tip displacement, contributing to the plateau formation for displacement and decay on the absolute velocity. Thus, ~40% covered soft actuator outperforms 100 % covered actuators with respect to speed while the maximum tip displacement is same.

Finally, the effect of the aspect ratio of the 40% covered films on photoactuation was evaluated. The widths (W_{PEI}) of the films were increased while maintaining 25 mm length, fractional coverage (40%), and thickness (90 μm) (**Figure 5.4b**). By increasing the aspect ratio from 1.3 to 5, the maximum tip displacement and the average speed for the first 5 s of illumination increased linearly. When increasing the aspect ratio, the width of the LCE layer (W_{LCE}) is proportionally reduced. As a result, the 2% contraction that occurs along W_{LCE} that result in bending opposing the tip displacement is minimized, but the expansion (~4.3%) along the longitudinal axis responsible for the bending is kept constant, as the length is not altered. Thus, increasing the aspect ratio result in larger and faster actuations as the opposing bending motions are reduced.

5

Actuators with Multiple Deformation Modes

The previous section showed it is not necessary to fully cover the passive layer to obtain large light-driven deformations, paving the way to fabricate actuators in which discrete regions may be independently triggered. To explore this possibility, a 20 × 25 mm² film topped by two 4 × 25 mm² stripes of LCE separated by 4 mm was fabricated (**Figure 5.5a**). The film has 40% of the PEI foil covered by the LCE and an aspect ratio of 1.3. Thanks to the space between the two active layers, each can be individually triggered. Triggering one or the other LCE stripes by continual exposure up and down the stripe results in a twisting motion in either counterclockwise or clockwise directions, depending in which stripe is activated. When both lines are irradiated simultaneously, the film bends with the bend significantly greater than for a film having the same aspect ratio and total coverage fraction (40%) but with active region concentrated as a single line in the center. Such performance enhancement suggests how the active layer is distributed should also be considered when designing the bilayer actuator. We hypothesize that this increased amplitude response is the result of reducing the aspect ratio of the active layer, minimizing the countering effects of LCE stripe perpendicular expansion.

As demonstrated in **Chapter 4**, the LCE network is known to have a temperature-controlled directionality of light-driven bending. We thus investigated the possibilities to induce additional shape changes in fabricated film (20 × 25 mm², 40% coverage, 90 μm of LCE, **Figure 5.5a**) by combining light and temperature (**Figure 5.5b**). Rather than being suspended underwater, the film was left lying on the floor of the container with the LCE side facing upwards. Upon light illumination from the top at 19 °C, the film bent, and consequently ended up standing. The light was switched off and the temperature was gradually increased from 19 °C to 28 °C. Initially, the film started to unbend towards its initial flat state. This phenomenon was expected as temperature induces a phase transition in the polymer network from smectic to nematic, resulting in a gradual contraction of the illuminated LCE.[19] But from 30 °C to 50 °C, the film started to bend perpendicular to the longitudinal axis, increasing its curvature with temperature. Illumination with blue light had no effect on this deformation. Sudden removal from the water and placement on a 20 °C surface resulted in recovery of its initial bent state along the longitudinal axis. Placed again in water at 50 °C, the film immediately switched its bending to opposite to longitudinal axis instead of along it. We believe this atypical perpendicular bending is the result of the temperature induced LCE expansion occurring opposite to the alignment direction. Thus, combination of light and
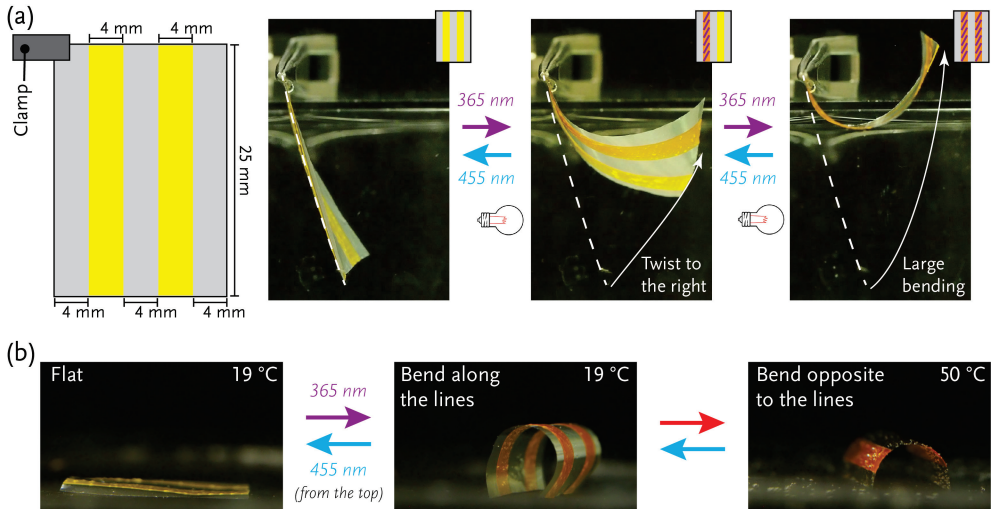
Figure 5.5 Underwater performance of an actuator when two different stimuli, light and temperature, are combined. (a) On the left a schematic drawing of the actuator. Yellow indicates the LCE and light grey represents the PEI. The thickness of the LCE was found to be 90 µm. On the right, edge-on images of the actuator showing the different deformations accomplished when illuminated, partially or completely, with a 365 nm (80 mW cm^{-2}). The insets show which region of the actuator is illuminated in each case; the active part has been patterned with purple lines and colored in orange. (b) A series of images showing the deformations that the actuator from (a) undergoes when no constrains are applied and light (from the top) and temperature are used to trigger different stresses and induce phase changes on the active layer that result in bending in opposite directions.

temperature led to a film that reversibly switches from flat, to bent along the longitudinal axis to bending opposite to it; a shape change difficult to achieve in other ways.

A Light-Responsive Photonic Actuator

The actuator presented in the previous section (20 × 25 mm², 40% coverage, 90 µm of LCE, **Figure 5.5a**) left a significant fraction of the PEI foil uncovered. This allows for deposition of additional functional materials to the blank regions. We opted to print a material with a different functionality. Recently, a cholesteric liquid crystalline (CLC)-ink suitable for DIW that results in a photonic polymer network with helical arrangement of the molecules, in which the pitch is the distance of a full rotation of a molecule was developed.[28] This CLC ink was used to print a 3 × 24 mm² line between the previously deposited light-responsive LCE stripes, **Figure 5.6a**. Optical and structural characterization of the additional, reflective layer shows a broad reflection band centered at 564 nm and a thickness of 100 µm (**Figure 5.6b-c**). The edges of the layer are less defined

that those observed in **Figure 5.2c**, as the CLC ink has a lower viscosity than the LCE-ink, and so after extrusion it shows increased spreading before polymerization. The difference in viscosity between the inks also explain the de-wetting observed at the extremes of the reflective stripe. The film still displays large bending deformations triggered by light despite addition of an extra layer.
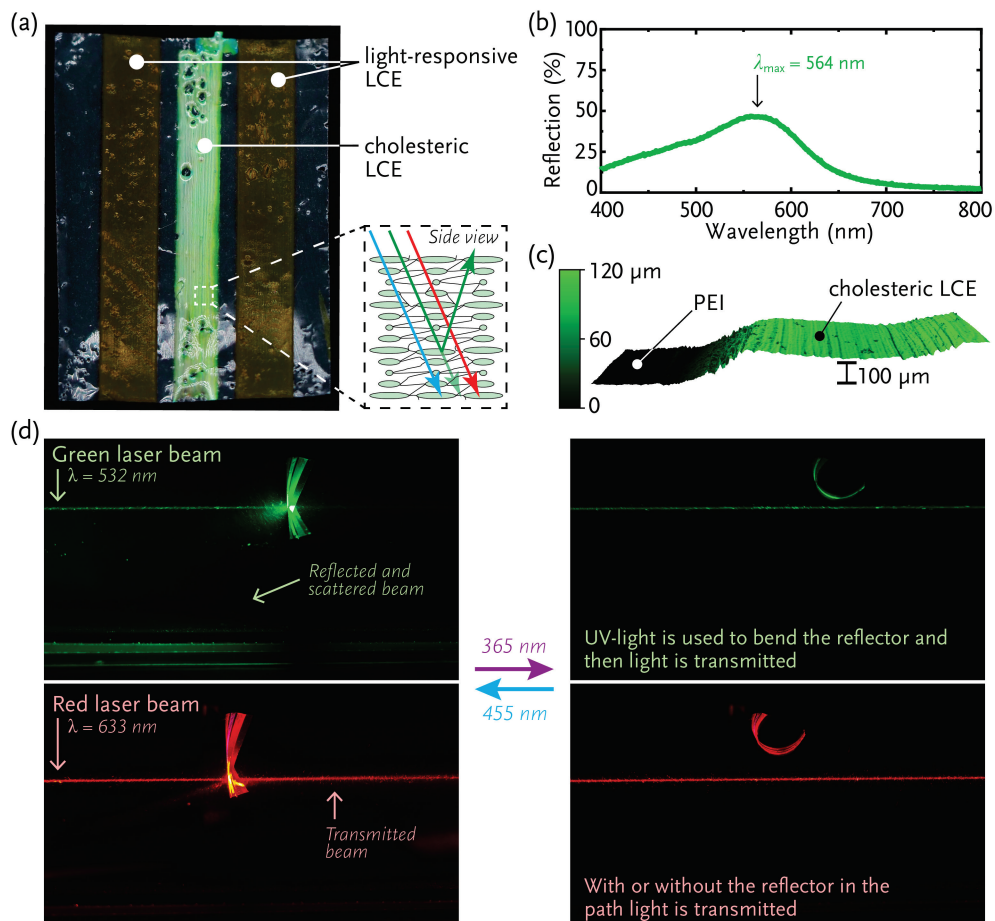
Figure 5.6 A light-responsive photonic actuator. (a) A front image of the fabricated light-responsive photonic actuator. The inset shows the molecular alignment of the cholesteric LCE line, which consist of a helix structure. Thanks to the periodicity of the full rotation of the helix, around 376 nm, the middle line acts as reflector for green light. (b) Percentage of reflected light as a function of the incident wavelength into the cholesteric LCE. (c) 3D profile of the edge of the cholesteric LCE and the PEI. (d) A series of edge-on images in which the selectivity to reflect specific wavelength of the actuator and light-driven deformation are shown. The images show the actuator underwater. The 365 nm (80 mW cm^{-2}), 455 nm (145 mW cm^{-2}) and laser lights were all applied from the left side.

The potential use as a dynamic reflector was investigated (**Figure 5.6d**). The light-responsive actuating reflector was suspended underwater and the CLC line exposed to light from either green (λ = 532 nm) or red (λ = 633 nm) lasers. At rest, red light was transmitted while green light was partially reflected as anticipated, **Figure 5.6b**. 365 nm light was then used to trigger the responsive LCE in the stripes, causing film bending. As a result, the middle, reflective region, was removed from the path of both lasers, permitting the transmission of the green laser through the water. This demonstrator embodies the potential of using DIW to fabricate bilayer actuators that perform various tasks; in this case, motion and light reflection within a single object.

5.3 Conclusions

This chapter demonstrates using DIW to fabricate LC-based bilayer films leads to actuators that can deliver alternative, controlled shape deformations. The systematic study performed in this work revealed passive layers can be made responsive without full coverage with the active material without negatively affecting performance. Partial coverage offers the possibility to have discrete active regions on the foils that can be individually triggered. As a result, we could achieve reversible light-driven twisting in addition to bending or induce bending parallel and perpendicular to one of the axes when light and temperature were combined. Additionally, partially covering the passive layer also allows a facile combination of different materials that have distinct functionalities in a single device. This was demonstrated by fabricating a photonic light-responsive actuator that could selectively reflect a specific wavelength on-demand.

Chapter 4 and **Chapter 5** combined have shown the development of an LC ink and its innovative use in fabricating centimeter-scale actuators. The results discussed in these chapters embody the potential of using DIW to fabricate soft actuators with multiple functions and deformations modes on-demand.

5.4 Experimental Details
Materials and Reagents

1,4-Bis-[4-(6-acryloyloxyhexyloxy) benzoyloxy]-2-methylbenzene (**1**) was obtained from Merck. 4,4′-Bis(6-acryloyloxyhexyloxy) azobenzene (**2**) was acquired from Synthon. 2,22-(ethylenedioxy) diethanethiol (**3**) and 1,8-diazabicyclo[5.4.0]undec-7-ene (DBU) were purchased from Sigma-Aldrich. The photoinitiator bis(2,4,6-trimethylbenzoyl)-phenylphosphineoxide (**4**) was obtained from Ciba. The chiral dopant, (3*R*,3a*R*,6*S*,6a*R*)-hexahydrofuro[3,2-b]furan-3,6-diyl bis(4- ((4-(((4-

(acryloyloxy)butoxy)carbonyl)oxy)benzoyl)oxy)benzoate) (**5**) used to prepared the CLC ink was purchased from BASF SE. 1,8-diazabicyclo[5.4.0]undec-7-ene (**6**, DBU) and dime-thylphenylphosphine (**7**, Me2PPh) were acquired from TCL Chemicals Europe N.V. Dichloro-methane (DCM) was obtained from Biosolve. Polyetherimide foil (Ultem™ UTF 120) of 10±2 µm was supplied from Sabic.

Characterization

The number average molecular weight (M_n) of the oligomers and their average repeating unit were obtained from the ^{1}H NMR spectrum performed on a 400 MHz Bruker Advance III HD spectrometer with deuterated chloroform as solvent. A Shimadzu UV-3102 PC apparatus was utilized to perform gel permeation chromatography to measure the weight average molecular weight (M_w) and polydispersity index (PDI); using polystyrene (PS) with an average M_w of 350,000 g mol^{-1} as reference. The locations of the phase and glass transitions were determined from the DSC traces obtained in a TA Instruments DSC Q1000 at cooling and heating rates of 10 °C min^{-1}. The mechanical properties of freestanding PEI and LC films were measured on a TA instruments Q800 dynamic mechanical analyzer (DMA). Storage moduli as a function of temperature (5 °C min^{-1}) were measured at multi-frequency-strain (1 Hz) with an amplitude of 20 µm. Expansion coefficients were determined in controlled force (10 mN) experiments, in which the reversible changes in length were monitored as a function of temperature (5 °C min^{-1}). Optical micrographs were recorded in a Leica DM 2700M polarized optical microscope equipped with a Leica MC170 HD camera. All structures were visualized in bright field and transmission modes. An optical profiling system (S Neox 3D Optical profiler, equipped with a ×5 objective) was employed to record 3D profiles of the edges of the printed polymers to measure their thickness. UV–vis spectroscopy was recorded on a Perkin Elmer Lambda 750 spectrometer equipped with a 150 mm integrating sphere and tungsten halogen light source for measurements 320 - 850 nm. The samples were place before the inlet of the integrating sphere for transmissions and absorption measurements and at the back of the outlet for reflection measurements.

Preparation of the LC Ink

The LC-oligomer was prepared as previously reported.[19] The synthesis is based on a catalyzed thiol-acrylate Michael addition reaction of diacrylate mesogen **1** and diacrylate azobenzene **2** using **3** as a spacer. The acrylate-to-thiol ratio was set to 1.0:0.9 to obtain acrylate terminated oligomers. The final concentration of azobenzene was 7 wt% **2**. In short, **1-3** are first dissolved in DCM, and a few drops of DBU (**6**) are added into the solutions during mixing. The solution was left to react

for at least 2h followed by washing of the oligomer with 1 M HCl (2×) and saturated brine (1×) to remove the remaining DBU. Subsequently, the organic phase was collected and dried with $MgSO_4$ and the residual solvent removed in a vacuum oven at 90°C overnight. The LC ink was prepared by mixing the LC-oligomer (98 wt%) with the photoinitiator (2 wt% **4**) in DCM. After complete dissolution of the different components, the solvent was removed by casting the solution in a Teflon petri dish and by leaving it at room temperature under vacuum overnight.

Preparation of the CLC Ink

The photonic CLC ink was prepared as previously described.[28] In short, the CLC ink was prepared via a based catalyzed thiol-acrylate Michael addition. In this case **1** and **5** were combined with **3**, which acted again as a change extender. Here the molar ratio diacrylate to dithiol was 3:2. The final concentration of chiral dopant was 5.7 wt% **5**. After dissolving all components in DCM at room temperature, the catalyst **7** was added and the reaction left under strong stirring for 1h. Subsequently, the residual solvent was removed at room temperature overnight at ambient conditions. The CLC ink was prepared by mixing the CLC-oligomer (98 wt%) with the photoinitiator (2 wt% **4**) in DCM. The solvent was removed at room temperature overnight at ambient conditions.

Direct Ink Writing

Controlled depositions of the inks on the 10 µm thick PEI foil were performed using a commercial 3D printer (EHR, Hyrel 3D). The inks were loaded at room temperature into a stainless-steel reservoir with 335 µm nozzle diameter (27 ga A.W.G, Fisnar QuantX Micron-S Red). Optimal printing conditions, resulting in either uniaxially alignment parallel to the printing direction or cholesteric alignment were, respectively, 7 mm s^{-1} with the syringe at 70 °C and the bed at room temperature, and 2 mm s^{-1} with the syringe at 90 °C and the bed at 53 °C. The G-code that controlled the printing path was generated by the printer software. After printing, photopolymerization was induced under N_2 using an Exfo Omnicure S2000 light source in which 57% of the light intensity is 395 – 445 nm and 43% 320–390 nm. For samples containing azobenzene (**2**), a high-pass filter (405 nm) was employed to avoid undesired isomerization and exposure took place over 2h, in which the films were flipped every 30 min to circumvent a gradient formation in the crosslink density through the printed line thickness.[19] Polymerization for CLC lines took place in 30 min. The difference on the polymerization time of the two inks arises from the different viscosities (effecting the mobility of free radicals), crosslink densities (effecting on the probability for crosslinks to form), and filter use (lowering the maximum light intensity available). After fabrication, the optical

5

properties, thickness and alignment of the printed lines were characterized using UV-Vis spectroscopy, a 3D profiling system, and a microscope, respectively.

Gel fraction

The crosslinked fraction of the LCE network is defined as the gel fraction. To measure, a film was immersed in DCM for 24 h at room temperature. The sample was filtered and dried at 60 °C in a vacuum oven. The fraction of gel in the network was determined using the **Equation 1**, in which $m_{initial}$ is the mass of the film before immersion in DCM and m_{dry} after it, filtration, and subsequent drying.

$$\text{Percentage of gel fraction} = (m_{dry} \,/\, m_{initial})\, 100 \qquad (1)$$

Laser Cutting

Slicing of the PEI foil and LCE were performed using a laser cutter (Universal Laser Systems VLS 3.50, VersaLASER) equipped with a 40 W max. CO_2 laser beam. The actual intensity incident on the sample depends on the scanning speed (set at 80%), dots per inch (set to 500), the focus (0.1mm above the sample holder), material absorbance, and the cleanness of the equipment. As a result, the laser power is difficult to reproduce from day-to-day, so before every cutting session the optimal laser power was determined. All samples in which actuations were compared were cut the same day. The cutting path used to slice the samples was defined using the AutoCAD software (Autodesk). The high temperatures created during cutting appear to induce a pre-bend in the samples, even in bare PEI foil samples.

Underwater Photoactuation of the Actuators

The different films, either suspended or laying on the floor, were located inside a transparent container with flat sides filled with water. UV (365 nm, Thorlabs M365L2) and blue (455 nm, Thorlabs M455L3-C2) lights were used to switch between the two-isomerization states of the azobenzene groups. The light intensities were adjusted using a controller (ThorLabs DC4104). Before illumination, the samples were pre-exposed to 455 nm light to ensure all azobenzene groups were in the *trans*-isomer. The light-driven deformations were recorded using a camera (Nikon D7200, Olympus OM-D E-M10 Mk III). The temperature of the water was controlled with a digital thermometer: unless specificized, its temperature was 19 °C. The tip displacement of the bilayer films was analyzed using ImageJ software. When investigating the selectivity of the printed CLCE to reflect certain wavelength, green ($\lambda = 532$ nm, <1 mW, BASETech) and red ($\lambda = 633$ nm, <4 mW, JDS Unlphase) lasers were employed.

5.5 References

1   M. del Pozo, J. A. H. P. Sol, A. P. H. J. Schenning and M. G. Debije, *Adv. Mater.*, 2021, 2104390.
2   A. Sydney Gladman, E. A. Matsumoto, R. G. Nuzzo, L. Mahadevan and J. A. Lewis, *Nat. Mater.*, 2016, **15**, 413–418.
3   F. Momeni, S. M.Mehdi Hassani.N, X. Liu and J. Ni, *Mater. Des.*, 2017, **122**, 42–79.
4   X. Wan, L. Luo, Y. Liu and J. Leng, *Adv. Sci.*, 2020, **7**, 2001000.
5   A. Kotikian, C. McMahan, E. C. Davidson, J. M. Muhammad, R. D. Weeks, C. Daraio and J. A. Lewis, *Sci. Robot.*, 2019, **4**, eaax7044.
6   M. O. Saed, C. P. Ambulo, H. Kim, R. De, V. Raval, K. Searles, D. A. Siddiqui, J. M. O. Cue, M. C. Stefan, M. R. Shankar and T. H. Ware, *Adv. Funct. Mater.*, 2019, **29**, 1806412.
7   L. Ceamanos, Z. Kahveci, M. López-Valdeolivas, D. Liu, D. J. Broer and C. Sánchez-Somolinos, *ACS Appl. Mater. Interfaces*, 2020, **12**, 44195–44204.
8   A. Kotikian, R. L. Truby, J. W. Boley, T. J. White and J. A. Lewis, *Adv. Mater.*, 2018, **30**, 1706164.
9   K. Kim, Y. Guo, J. Bae, S. Choi, H. Y. Song, S. Park, K. Hyun and S. Ahn, *Small*, 2021, **17**, 2100910.
10   X. Lu, C. P. Ambulo, S. Wang, L. K. Rivera-Tarazona, H. Kim, K. Searles and T. H. Ware, *Angew. Chemie Int. Ed.*, 2021, **60**, 5536–5543.
11   M. López-Valdeolivas, D. Liu, D. J. Broer and C. Sánchez-Somolinos, *Macromol. Rapid Commun.*, 2018, **39**, 1700710.
12   J. Zhang, Y. Guo, W. Hu and M. Sitti, *Adv. Mater.*, 2021, **33**, 2100336.
13   D. Li, S. Wang, J. He, H. Zeng, K. Yao, Z. Gao, M. Wu, Y. Liu, L. Wang, Z. Xie and X. Yu, *Adv. Mater. Technol.*, 2021, **6**, 2001095.
14   M. Pilz da Cunha, M. G. Debije and A. P. H. J. Schenning, *Chem. Soc. Rev.*, 2020, **49**, 6568–6578.
15   C. Huang, J. Lv, X. Tian, Y. Wang, Y. Yu and J. Liu, *Sci. Reports 2015 51*, 2015, **5**, 1–8.
16   M. Pilz da Cunha, H. S. Kandail, J. M. J. den Toonder and A. P. H. J. Schenning, *Proc. Natl. Acad. Sci.*, 2020, 202004748.
17   M. Pilz da Cunha, S. Ambergen, M. G. Debije, E. F. G. A. Homburg, J. M. J. den Toonder and A. P. H. J. Schenning, *Adv. Sci.*, 2020, **7**, 1902842.
18   D. Rus and M. T. Tolley, *Nature*, 2015, **521**, 467–475.
19   M. del Pozo, L. Liu, M. Pilz da Cunha, D. J. Broer and A. P. H. J. Schenning, *Adv. Funct. Mater.*, 2020, **30**, 2005560.
20   M. Pilz da Cunha, Y. Foelen, R. J. H. Raak, J. N. Murphy, T. A. P. Engels, M. G. Debije and A. P. H. J. Schenning, *Adv. Opt. Mater.*, 2019, **7**, 1801643.
21   M. Pilz da Cunha, Y. Foelen, T. A. P. Engels, K. Papamichou, M. Hagenbeek, M. G. Debije and A. P. H. J. Schenning, *Adv. Opt. Mater.*, 2019, **7**, 1801604.
22   R. C. P. Verpaalen, M. Pilz da Cunha, T. A. P. Engels, M. G. Debije and A. P. H. J. Schenning, *Angew. Chemie Int. Ed.*, 2020, **59**, 4532–4536.
23   T. J. White and D. J. Broer, *Nat. Mater.*, 2015, **14**, 1087–1098.
24   S. Timoshenko, *J. Opt. Soc. Am.*, 1925, **11**, 233.
25   G. N. Mol, K. D. Harris, C. W. M. Bastiaansen and D. J. Broer, *Adv. Funct. Mater.*, 2005, **15**, 1155–1159.
26   J. A. H. P. Sol, A. R. Peeketi, N. Vyas, A. P. H. J. Schenning, R. K. Annabattula and M. G. Debije, *Chem. Commun.*, 2019, **55**, 1726–1729.
27   M. Pilz da Cunha, E. A. J. van Thoor, M. G. Debije, D. J. Broer and A. P. H. J. Schenning, *J. Mater. Chem. C*, 2019, **7**, 13502–13509.
28   J. A. H. P. Sol, H. Sentjens, L. Yang, N. Grossiord, A. P. H. J. Schenning and M. G. Debije, *Adv. Mater.*, 2021, **33**, 2103309.

5

Chapter 6

Future Challenges for
Additive Manufacturing of Liquid Crystals
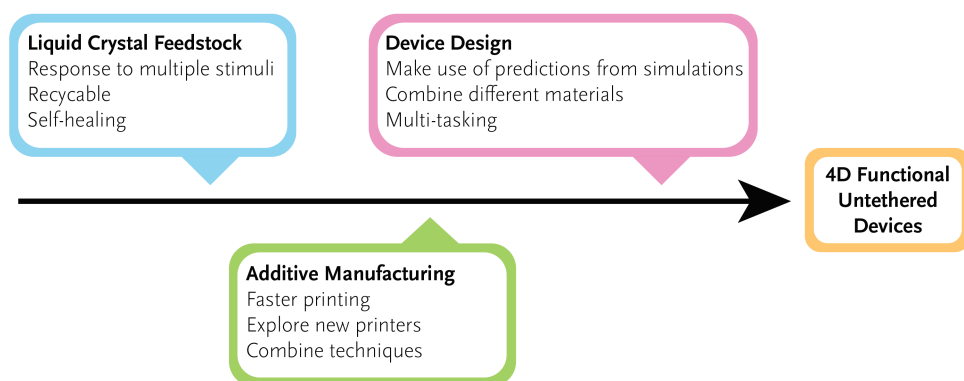
Abstract

Liquid crystal materials are finding their place in additive manufacturing for fabricating 4D functional untethered devices across different length scales. While impressive progress has been made, there are still several challenges to be addressed before the full potential of 4D printing of liquid crystals may be unleashed. In this chapter future challenges and unexplored avenues are discussed from the perspective of material, additive manufacturing equipment, and device design.

6.1 Introduction

The field of 4D printing of liquid crystals (LC) has been growing at an increasing rate in recent years. While remarkable examples of functional untethered devices have been reported[1] which embody the potential and appeal of 4D printing LCs for many different fields, there is still considerable room for future developments, both in terms of the feedstock materials as well as additive manufacturing (AM) processes. The field of 4D printing with LCs is still in its infancy, which means that considerable knowledge acquired from previous studies of liquid crystal networks (LCN) films, actuators and liquid crystals displays (LCD) screens has not yet been exploited by AM techniques. While reactive LCs might not achieve the commodity status of common polymers, and most AM techniques are not suited for mass production, 4D printing can still help meet future needs in biomedical applications or personalized soft human-interface devices, for instance. In this chapter, possible research avenues to meet these needs in future, and what follows from the results described in this thesis are presented.

6.2 Stimuli-responsive Materials

Stimuli

In this thesis, actuators that can be addressed with more than one stimulus are presented that embody the advantages of combining responsivity to multiple stimuli in a single device. For example, it can provide additional ways to control the actuation (**Chapter 3** and **Chapter 4**) or it can open new deformations modes that are otherwise inaccessible (**Chapter 5**). LCs mixtures used in AM currently reported lack of this beneficial dual response, which calls for the exploration of new liquid crystalline polymers. There already is widespread knowledge on the combination of functionalities and/or responses in a single LCN formulation to obtain humidity- and chemical-sensitive optics,[2–4] humidity-gated UV-responsive actuators,[5] or humidity-gated temperature-responsive IR reflective coatings.[6] These systems benefit from additional properties, or increase control of device performance thanks to these double functionalities or responses. Translating these combinations into extrudable LC-oligomers or into LC photoresists for direct laser writing by two-photon polymerization (DLW-TPP) would be of great interest. As an alternative to making the entire network response to different stimuli, one can also focus on combining different materials in the device to achieve the same result as shown in **Chapter 5**, where a light-responsive green light-reflective actuator is fabricated.

Reactive Mesogens

To date, most reported reactive mesogens (RM) formulations for AM make use of acrylate free-radical polymerization for final crosslinking steps. Significant downsides of radical polymerization reactions is that these are notoriously sensitive to chain growth termination by atmospheric oxygen, and suffer from polymerization shrinkage.[7] The effects of the latter was seen in **Chapter 2**, in which the direction of the alignment suffered significant shrinkage in the microstructures. Epoxide and oxetane moieties as reactive groups, both of which polymerize through a cationic mechanism, have limited polymerization shrinkage, and their polymerization is oxygen-insensitive.[7] The use of these moieties have only limitedly been explored in thin-film LCNs, been reported once for a photoresists for DLW-TPP (**Figure 6.1a**)[8] and never explored for direct ink writing (DIW) inks. The reduced polymerization shrinkage would be beneficial for the fabrication of microstructures and the oxygen-insensitivity could help in ensuring the highest possible polymerization conversion and thereby long-term integrity in centimeter-scale objects.

Circular Materials

The development of recyclable LCE materials is a research area that is underexplored. Recyclability becomes increasingly important as the volumes of LC materials increase to meet the demands of mass production. Given that currently most polymeric LC devices are thermosets which are difficult to recycle, most will end up in landfills after use, or mechanically ground down into low-quality filler materials.[9] The development of more sustainable, circular LC materials for additive manufacturing can be approached by: (*1*) developing self-healing dynamic covalent crosslinked LC formulations, (*2*) thermoplastic LC designs, or (*3*) LC mesogens that can be degraded in a functional manner. A final option, (*4*) design of liquid crystalline materials based on renewable sources, should also be investigated.

One of the foremost solutions (*option 1*) is to develop thermosets with reversible crosslinks, which would allow for reconfiguration of the material into new shapes, or complete melting for recycling. At the same time, many chemistries that allow for reconfigurability also inherently bring (self-)healing capabilities, which would extend the useful lifetime of the materials.

Currently, thermoplastic LCs (*option 2*) are mainly limited to engineering polymers such as Kevlar™ or Vectra™, which show extraordinary Young's moduli but also require harsh conditions for processing—Kevlar is spun from concentrated H_2SO_4 [10] and fused filament fabrication (FFF) of Vectra requires nozzle temperatures above 280 °C.[11] Furthermore, while they share the strong
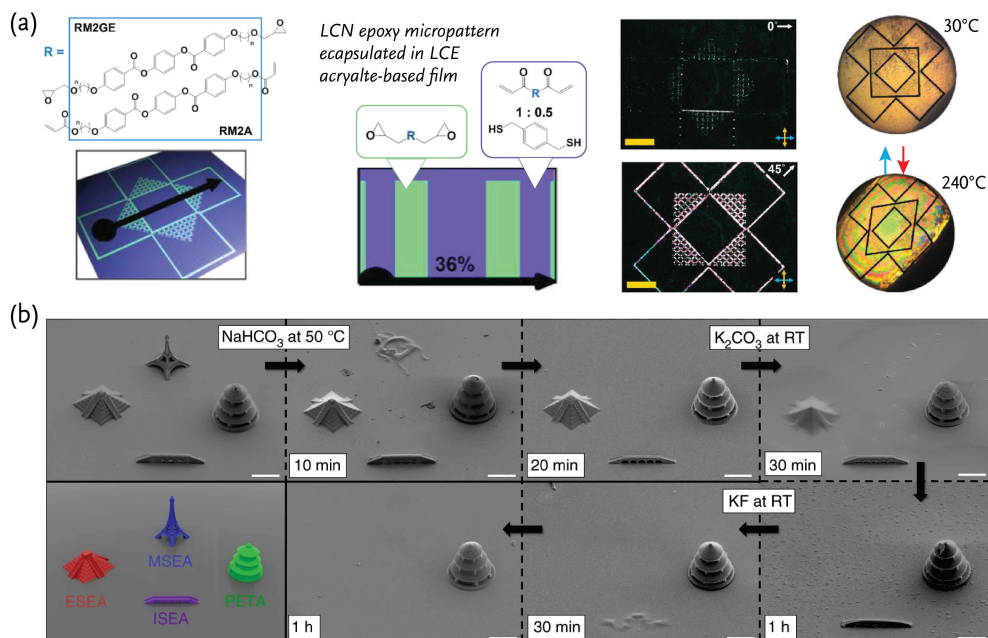
6

Figure 6.1 (a) A hybrid actuator composed of DLW-TPP LCN epoxy pattern encapsulated in LCE acrylate-based film. (Top) the design of the actuator and the molecules used to prepare the different parts; (middle) crossed polarized light micrograph; (bottom) micrograph of the structure at different temperature showing its response. The scale bars from represent 500 μm. Adapted with permission.[8] Copyright 2019, Wiley-VCH. (b) Scanning electron micrographs showing selective cleavage of different structures. The "responsive" 3D microstructures are made from a silyl ether linkage in which different crosslinkers are used, which contained methyl (MSEA), ethyl (ESEA) or isopropyl (ISEA) substituents on the silicon atom. The structure that does not dissolve is made from pentaerythritol triacrylate (PETA). Scale bars represent 20 μm. Modified with permission under a CC BY license (Creative Commons Attribution 4.0 International License).[12]

anisotropy found in LC materials, importing the functionalities known from LCNs and LCEs into the polymers has not yet found widespread attention. Developing thermoplastic LCEs could be the middle road here, where short chains of LC oligomers physically bind. Since the material originates as a reactive mesogenic oligomer, this leads to easy incorporation of functional groups known from LCN and LCE research into the chains, while the physical crosslinking allows for remolding, reshaping, and eventually, recycling.

Easy breakdown of crosslinked LC materials (*option 3*) would require the design of new mesogens with labile chemical groups. Non-mesogenic formulations have been developed for DLW-

TPP that make use of silyl ether groups which readily disintegrate in alkaline conditions, depending on the substituents on the labile group (**Figure 6.1b**).[12]

Securing a sustainable future for the materials presented in this review also requires reviewing methods of synthesizing mesogens from renewable sources instead of from the petrochemicals that many organic compounds are currently derived from (*option 4*). Such a route is to consider alternative natural materials that show LC properties. An example of this are aqueous dispersions of cellulose nanocrystals which display cholesteric phases at specific concentrations.[13,14]

6.3 Additive Manufacturing Processes

To date, a few AM techniques have been proven applicable for LC-based materials. While direct ink writing and direct laser writing by two-photon polymerization have led to promising results and interesting devices, there are plenty of remaining techniques that can fill specific niches when combined with an LC feedstock. Some of these processes have been demonstrated just once, while others have not been reported at all.

Vat polymerization

A key challenge for any vat polymerization equipment is the relative volume of material required in the vat itself. Generally, LC-based materials are not inexpensive, and there is considerable "wasted" volume that make most conventional vat polymerization setups, *e.g.* stereolithography (SLA) or digital light projection (DLP), cost-prohibited. This may be alleviated by restructuring the vats to accommodate smaller volumes,[15] but the real challenge for these equipment is achieving bulk alignment. Since alignment is key to harnessing the unique properties of LC materials, it is not a trivial task to print LCs layer-by-layer and maintain proper alignment characteristics. Presumably, a thin alignment layer applied to the baseplate would allow alignment of the initial layers, but subsequent layers would need to rely on the already-deposited layers, so rapid degradation of the alignment fidelity would be expected. On top of that, SLA and DLP equipment have stages in the vat that move during the fabrication process, which can also disturb the alignment. These challenges have left vat polymerization techniques out of the race of fabrication of centimeter scale objects, and their use has been primarily for producing LC microstructures, at least for now.

Direct Laser Writing by Two-Photon Polymerization

When considering the use of LC photoresist in a DLW-TPP, there is one main limitation arising from the equipment: commercial printers do not have a heating stage incorporated. As a result,

6

the possibility to use well-known and quantified LC mixtures directly in DLW-TPP set-ups is not possible since reactive mesogenic mixtures with room temperature liquid crystalline phases are uncommon and challenging to prepare. These challenges unnecessarily slow progress on LC-based microdevices. Additionally, it has been shown that control over the temperature during the DLW-TPP process can reduce the swelling of the polymerized structure during fabrication and so enhance resolution of the LC microstructures;[16] thus, incorporating a heating stage in commercially available equipment is of significant value.[8,16]

While DLW-TPP can print with outstanding resolution, it comes at a high price: its production speed for large quantities of microstructures is extremely low. While for fundamental research application this is not a problem, it limits its possibilities to compete with other AM techniques in industry. In order to solve this, efforts are being made to increase the production speed by focusing multiple laser beams in the vat at the same time, by developing stages with faster scanning speeds and by exploring quicker polymerization mechanisms.[17,18] While these advances are still at its infancy, they show promising results towards faster production speeds for DLW-TPP.

As demonstrated in **Chapter 2** and **Chapter 3**, micro-actuators are of increasing interest for many reasons. One of the approaches to accomplish these actuators is by combining different functional materials, as showed in **Chapter 5** for centimeter-scale actuators. At the moment, there are examples of multiple materials combined in a single structure using DLW-TPP,[19–21] but numerous steps were necessary for fabrication, making the process tedious and long. Recently, DLW-TPP inside a microfluidic device was presented as a facile approach to accomplish multi-material micro-objects.[22] These kinds of innovations when translated for LC photoresist will advance the possible designs and increase complexity of responsive microstructures.

Digital Light Projection
Light-based manufacturing techniques such as DLW-TPP are often combined with alignment layers or cells to ensure proper orientation of the molecules for the intended function after the AM procedure. At the millimeter scale, a similar technique is digital light processing, although the issue here is the moving printer parts between light exposure steps may disturb the molecular alignment, and make it difficult to easily fit alignment layers around the LC resin. Nonetheless, three-dimensional LCN object have been made through a magnetic field-aligned DLP procedure (**Figure 6.2a**).[15] This alignment procedure could be extended to LC elastomer materials by using magnetic fields (B = 300 mT) to (re)align the LC monomers before crosslinking.[23] The LC

elastomer used in the latter work is a "side-on" LC, a reactive mesogen with acrylate moiety fixed to the central phenyl ring of the mesogenic core. After crosslinking such LCs, more freedom in movement is retained, leading to larger actuator responses. Both works also incorporated diacrylate azobenzene photoswitches and demonstrated photoinduced bending in their engineered structures. While one of the advantages of DLP is that it can utilize low molecular weight LCs, which is generally not possible in DIW to produce at the centimeter scale; LC elastomers should be more appropriate in centimeter-scale devices due to their larger range-of-motion, see **Chapter 1**.

3D Microextrusion

Extrusion based printing uses two main types of equipment: fused filament fabrication, FFF, for thermoplastic and direct ink writing for thermosets. LCs have found limited use with FFF, mainly due to material properties. Typical stimuli-responsive LCs are a viscous liquid or resin before crosslinking, meaning fabricating a solid-state filament spool is not possible. Obviously, processing crosslinked LCNs is not possible with FFF either; although the development of LCEs with reversible, physical crosslinks might prove an entry point of stimulus-responsive LC materials to
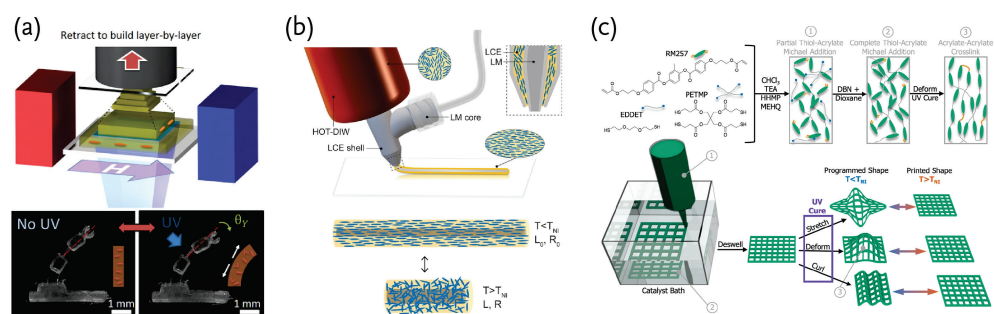
Figure 6.2 (a) Schematic of a DLP printer capable of printing layer-by-layer 3D objects with different molecular alignment using magnetic field (top). A two-axis robotic arm fabricated with the DLP printer that bends upon UV light illumination (bottom). Reproduced with permission.[15] Copyright 2019, American Chemical Society. (b) Schematic illustration of a core-shell 3D printing. The core of the extruded fiber is a liquid metal (LM) and the shell is made of liquid crystal elastomer (LCE), whose molecular director is parallel to the printing direction. Upon heating, the LCE goes a nematic to isotropic phase transitions that triggers an anisotropic shape. Reproduced with permission.[25] Copyright 2021, Wiley-VCH. (c) Schematic drawing of direct ink writing in a catalyst bath. (Top) synthetic scheme of the network forming and the different reactive steps during the fabrication process. (Bottom) overview of the fabrication process, shape preprogramming and actuation. Reproduced with permission.[28] Copyright 2020, American Chemical Society.

FFF. So far, the only LC materials reported that have been processed using FFF are high molecular weight thermoplastic LC polymers, such as the engineering plastic Vectra™.[11] Here, the strongly anisotropic properties of this material were encoded in computer-designed objects designed to have high-impact resistance, or act as load-bearing biomedical implants.

Direct Ink Writing

The light responsive green reflector fabricated in **Chapter 5** shows that it is greatly desirable for devices to be made of more than a single material.[24] Using non-responsive, mechanically superior materials as the skeleton of a device allows for application of the generally more expensive, responsive elements just as the actuating hinges, rather than designing the entirety of the object to out of LCs. An alternative way to those demonstrated in this thesis to achieve similar benefits is through coaxial DIW, where filaments are formed consisting of a heterogeneous core-shell makeup (**Figure 6.2b**). In such architectures, the inner and outer regions can perform different functions, such as a core that contracts upon heating with an outer layer that is optically active, or a core that conducts electricity or heat and an actuating outer shell that bends or twists.[25]

A completely different way to use DIW than discussed in **Chapter 1**, or used in **Chapter 4** and **Chapter 5**, harkens back to the original processing of LCEs: crosslinking after mechanical stretching of a partially polymerized network.[26,27] This stepwise fabrication of a monodomain, uniaxially aligned LCE was also used for thiol-acrylate-based LCE slabs.[27] Since after the first partial polymerization step a network is created that cannot be extruded, a workaround is needed for adaptation to DIW. The solution is dividing the first step into two:[28] synthesizing a partially crosslinked LCE network with a small fraction of thiol than the intended and adding to the printing syringe, along with the amounts of unreacted di- and tetrathiol required for proper conversion of the acrylate groups. After DIW printing into a solvent bath containing thiol-acrylate catalyst, the partially crosslinked printed network swiftly incorporates the thiol monomers to fully crosslink. This 3D written material can then be dried, deformed, and photopolymerized with UV light. During deformation, the LCE mesogen alignment reorients such that when thermally activated, the printed object shifts between the "as-printed" and "as-deformed" states (**Figures 6.2c**). While printing into the solvent bath significantly reduces printing resolution, physically shaping the low-temperature actuation state through physical molding circumvents the need for the (sometimes impossible) design of intricate molecular director patterns and suitable print paths.[28]

Fused Filament extrusion

Despite FFF being mostly unsuitable for LCNs due to their mechanical properties, it has been recently shown that incorporating densely crosslinked LCNs in an FFF procedure is possible.[29] In this contribution, stimuli-responsive cholesteric flakes as dopant in conventional 3D printing polymer filament are used. However, in this first report the flake response was not maintained after printing as a result of the humidity response of the LCN flake dopant being compromised by the barrier properties of the host polymer. Finding or developing more suitable water-permeable host polymers, or a new LCN formulation that works in this confined environment would open up a myriad of possibilities, given the widespread use of FFF printers and the current boom in filament material development.[30–32]

Inkjet Printing

Among drop-on-demand manufacturing techniques, inkjet printing (IJP) is the most common, and has been used for additive manufacturing of a variety of devices—organic light emitting diodes (LED)s and photovoltaics and hydrogels.[33,34] When used with crosslinkable inks, this technique can be used to rapidly build multi-material polymer objects at high resolution,[35] qualities that make it appropriate for mass production. For LCNs, IJP has been demonstrated, where through a combination of different LC formulations and sacrificial layers, a cilia array was printed, built up by segmented films emulating the motion cycle of cilia in the human lungs.[36] Despite this promising result, no follow-up efforts using IJP for LCN based devices has been reported. In contrast, IJP of LCE has not been reported at all and we deem it to be quite promising as these show larger actuation strokes, see **Chapter 1.** Nonetheless, the increased viscosity of LCE precursors may prove a significant obstacle to overcome for IJP. In addition, any alignment of the LC will need to rely on substrates, which will also limit the structures achievable.

Combining Multiple Additive Manufacturing Techniques in the Same Printer

Liquid crystal networks and elastomers provide significantly different amplitudes of response to external stimuli, so combination of these two materials, which also have distinct mechanical properties, in a single object through the use of AM techniques best suited for each material could open new avenues for the design of 4D objects. Additionally, it will also facilitate the realization of multi-responsive devices. To achieve this, the design of multi-process printers that combine multiple AM technique in one set-up are of interest. Intriguing developments in this direction are the recently reported set-ups that combines inkjet printing and direct ink writing[37] or digital light
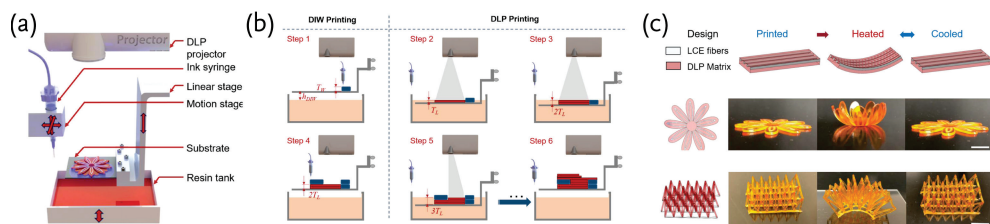
6

Figure 6.3 (a) Schematic of a hybrid 3D printer integrating DLP and DIW techniques in the same equipment. (b) Overview of the different steps to fabricate 3D objects using the hybrid printer. (c) Examples of fabricated objects. On the top, schematic of the working principal of the response. On the middle and bottom, two examples of a flower and a bi-stable lattice respectively. From left to right, computer aided design (CAD), after printing, when the object is heated, and when it is cooled down. Reproduced with permission.[38] Copyright 2021, Elsevier B.V.

projection with DIW (**Figure 6.3**).[38] These two examples show how it could be possible to combine in a single object the different mechanical properties and responses of LCNs and LCEs, an exciting new line of research.

6.4 Devices

The combination of additive manufacturing techniques with liquid crystal materials can lead to functional objects that self-propel,[24] walk,[39] grasp,[20] and act as optical sensors.[40] When designing LC-based 4D objects, not only does the geometry need to be carefully chosen to perform the desired tasks, but the mesogenic alignment must also be precisely selected. As discussed in **Chapter 1**, changes to geometry and/or alignment can both lead to significantly different deformation modes. For instance, identical shapes with differing alignments[41] or identical alignments in different geometries[42] can result in distinctive actuations. The results from **Chapter 2** presented an example of this tunability of the performance in the same LCN by changing the LC-based object. Fortunately, most deformation modes reported to date can be predicted using digital modelling.[43–47] Through simulation the interaction of alignment and geometry can be exploited to determine the optimal configuration for the desired device. For example, the actuators presented in **Chapter 5** would benefit from such predictions to, for instance, fabricate origami- and kirigami-inspired actuators. By using simulations to design LC-based objects via AM, new vistas of responsive devices that could be imagined but were not possible to fabricate just a few years ago could be revealed.[48]

6.5 Conclusions

Mostly due to economics of scale, additive manufacturing is positioning itself as a small-scale manufacturing technique for prototyping or producing short production runs of one-offs.[49] For most materials, conventional techniques such as casting, molding or extrusion are more cost-effective at large production runs. Vat polymerization techniques such as DLW-TPP and DLP are unlikely to conquer the mass market when used for reactive LC materials, but can fill very specific niche uses. In the case of DLW-TPP, highly accurate reproductions of computer aided designs at the micrometer-scale can be designed, possibly for use in biomedical engineering. On the other side, DIW is positioning as the best technique for the fabrication of centimeter-scale objects and might well develop into a manufacturing technique at all production scales. Compared to conventional techniques, DIW allows for easy programming of the molecular director and thus anisotropic mechanical properties. In additions to the necessary advances on the equipment side required for their use as mass production techniques, there still interesting research lines on the material side to be explored. Feedstocks for AM technique that result in networks responsive to various stimuli are much desired to achieve 3D multi-functional untethered devices. Finally, these advances, both in equipment and material sides, should be accompanied by innovative object design that make use of simulation prediction to uncover their full potential. Altogether, future progress in additive manufacturing of liquid crystals will bring 4D multi-functional untethered devices to realization with a widespread use in many fields.

6

6.6 References

1   M. del Pozo, J. A. H. P. Sol, A. P. H. J. Schenning and M. G. Debije, *Adv. Mater.*, 2021, 2104390.
2   J. E. Stumpel, E. R. Gil, A. B. Spoelstra, C. W. M. Bastiaansen, D. J. Broer and A. P. H. J. Schenning, *Adv. Funct. Mater.*, 2015, **25**, 3314–3320.
3   J. E. Stumpel, C. Wouters, N. Herzer, J. Ziegler, D. J. Broer, C. W. M. Bastiaansen and A. P. H. J. Schenning, *Adv. Opt. Mater.*, 2014, **2**, 459–464.
4   M. Moirangthem, R. Arts, M. Merkx and A. P. H. J. Schenning, *Adv. Funct. Mater.*, 2016, **26**, 1154–1160.
5   O. M. Wani, R. Verpaalen, H. Zeng, A. Priimagi and A. P. H. J. Schenning, *Adv. Mater.*, 2019, **31**, 1805985.
6   E. P. A. van Heeswijk, J. J. H. Kloos, N. Grossiord and A. P. H. J. Schenning, *J. Mater. Chem. A*, 2019, **7**, 6113–6119.
7   D. C. Hoekstra, A. P. H. J. Schenning and M. G. Debije, *Soft Matter*, 2020, **16**, 5106–5119.
8   J. M. McCracken, V. P. Tondiglia, A. D. Auguste, N. P. Godman, B. R. Donovan, B. N. Bagnall, H. E. Fowler, C. M. Baxter, V. Matavulj, J. D. Berrigan and T. J. White, *Adv. Funct. Mater.*, 2019, **29**, 1903761.
9   W. Post, A. Susa, R. Blaauw, K. Molenveld and R. J. I. Knoop, *Polym. Rev.*, 2020, **60**, 359–388.
10 D. Tanner, J. A. Fitzgerald and B. R. Phillips, *Adv. Mater.*, 1989, **1**, 151–156.
11 S. Gantenbein, K. Masania, W. Woigk, J. P. W. Sesseg, T. A. Tervoort and A. R. Studart, *Nature*, 2018, **561**, 226–230.
12 D. Gräfe, A. Wickberg, M. M. Zieger, M. Wegener, E. Blasco and C. Barner-Kowollik, *Nat. Commun.*, 2018, **9**, 2788.
13 Y. Liu and P. Wu, *Adv. Funct. Mater.*, 2020, **30**, 2002193.
14 G. Guidetti, H. Sun, A. Ivanova, B. Marelli and B. Frka-Petesic, *Adv. Sustain. Syst.*, 2021, **5**, 2000272.
15 M. Tabrizi, T. H. Ware and M. R. Shankar, *ACS Appl. Mater. Interfaces*, 2019, **11**, 28236–28245.
16 I. De Bellis, S. Nocentini, M. G. Delli Santi, D. Martella, C. Parmeggiani, S. Zanotto and D. S. Wiersma, *Laser Photon. Rev.*, 2021, 2100090.
17 L. Yang, A. El-Tamer, U. Hinze, J. Li, Y. Hu, W. Huang, J. Chu and B. N. Chichkov, *Opt. Lasers Eng.*, 2015, **70**, 26–32.
18 C. N. LaFratta and L. Li, in *Three-Dimensional Microfabrication Using Two-Photon Polymerization*, Elsevier, 2019, pp. 385–408.
19 H. Zeng, P. Wasylczyk, C. Parmeggiani, D. Martella, M. Burresi and D. S. Wiersma, *Adv. Mater.*, 2015, **27**, 3883–3887.
20 D. Martella, S. Nocentini, D. Nuzhdin, C. Parmeggiani and D. S. Wiersma, *Adv. Mater.*, 2017, **29**, 1704047.
21 D. Martella, D. Antonioli, S. Nocentini, D. S. Wiersma, G. Galli, M. Laus and C. Parmeggiani, *RSC Adv.*, 2017, **7**, 19940–19947.
22 A. C. Lamont, M. A. Restaino, M. J. Kim and R. D. Sochol, *Lab Chip*, 2019, **19**, 2340–2345.
23 Y. Yao, J. T. Waters, A. V. Shneidman, J. Cui, X. Wang, N. K. Mandsberg, S. Li, A. C. Balazs and J. Aizenberg, *Proc. Natl. Acad. Sci.*, 2018, **115**, 12950–12955.
24 A. Kotikian, C. McMahan, E. C. Davidson, J. M. Muhammad, R. D. Weeks, C. Daraio and J. A. Lewis, *Sci. Robot.*, 2019, **4**, eaax7044.
25 A. Kotikian, J. M. Morales, A. Lu, J. Mueller, Z. S. Davidson, J. W. Boley and J. A. Lewis, *Adv. Mater.*, 2021, **33**, 2101814.
26 H. Wermter and H. Finkelmann, *e-Polymers*, 2001, **1**, 1–13.
27 C. M. Yakacki, M. Saed, D. P. Nair, T. Gong, S. M. Reed and C. N. Bowman, *RSC Adv.*, 2015, **5**, 18997–19001.
28 M. Barnes, S. M. Sajadi, S. Parekh, M. M. Rahman, P. M. Ajayan and R. Verduzco, *ACS Appl. Mater. Interfaces*, 2020, **12**, 28692–28699.
29 J. A. H. P. Sol, L. M. Kessels, M. del Pozo and M. G. Debije, *Adv. Photonics Res.*, 2021, **2**, 2000115.
30 V. Mazzanti, L. Malagutti and F. Mollica, *Polymers (Basel).*, 2019, **11**, 1094.
31 S. C. Ligon, R. Liska, J. Stampfl, M. Gurr and R. Mülhaupt, *Chem. Rev.*, 2017, **117**, 10212–10290.
32 B. Brenken, E. Barocio, A. Favaloro, V. Kunc and R. B. Pipes, *Addit. Manuf.*, 2018, **21**, 1–16.
33 P. Calvert, *Chem. Mater.*, 2001, **13**, 3299–3305.
34 K. Pataky, T. Braschler, A. Negro, P. Renaud, M. P. Lutolf and J. Brugger, *Adv. Mater.*, 2012, **24**, 391–396.
35 A. R. Studart, *Chem. Soc. Rev.*, 2016, **45**, 359–376.
36 C. L. van Oosten, C. W. M. Bastiaansen and D. J. Broer, *Nat. Mater.*, 2009, **8**, 677–682.
37 D. J. Roach, C. M. Hamel, C. K. Dunn, M. V. Johnson, X. Kuang and H. J. Qi, *Addit. Manuf.*, 2019, **29**, 100819.
38 X. Peng, X. Kuang, D. J. Roach, Y. Wang, C. M. Hamel, C. Lu and H. J. Qi, *Addit. Manuf.*, 2021, **40**, 101911.
39 H. Zeng, D. Martella, P. Wasylczyk, G. Cerretti, J.-C. C. G. Lavocat, C.-H. H. Ho, C. Parmeggiani and D. S. Wiersma, *Adv. Mater.*, 2014, **26**, 2319–2322.
40 M. del Pozo, C. Delaney, C. W. M. Bastiaansen, D. Diamond, A. P. H. J. Schenning and L. Florea, *ACS Nano*,

2020, **14**, 9832–9839.

41 Y. Guo, H. Shahsavan and M. Sitti, *Adv. Mater.*, 2020, **32**, 2002753.

42 J. A. H. P. Sol, A. R. Peeketi, N. Vyas, A. P. H. J. Schenning, R. K. Annabattula and M. G. Debije, *Chem. Commun.*, 2019, **55**, 1726–1729.

43 C. D. Modes and M. Warner, *Phys. Rev. E*, 2011, **84**, 021711.

44 L. T. de Haan, V. Gimenez-Pinto, A. Konya, T.-S. Nguyen, J. M. N. Verjans, C. Sánchez-Somolinos, J. V. Selinger, R. L. B. Selinger, D. J. Broer and A. P. H. J. Schenning, *Adv. Funct. Mater.*, 2014, **24**, 1251–1258.

45 A. H. Gelebart, D. J. Mulder, M. Varga, A. Konya, G. Vantomme, E. W. Meijer, R. L. B. Selinger and D. J. Broer, *Nature*, 2017, **546**, 632–636.

46 A. R. Peeketi, N. Swaminathan and R. K. Annabattula, *J. Appl. Phys.*, 2021, **129**, 145107.

47 R. C. P. Verpaalen, M. G. Debije, C. W. M. Bastiaansen, H. Halilović, T. A. P. Engels and A. P. H. J. Schenning, *J. Mater. Chem. A*, 2018, **6**, 17724–17729.

48 C. D. Modes and M. Warner, *Europhys. Lett.*, 2012, **97**, 36007.

49 I. J. Petrick and T. W. Simpson, *Res. Technol. Manag.*, 2013, **56**, 12–16.

6

Acknowledgements

Dear colleagues, friends, and family, after four years as a PhD candidate I can proudly present my thesis to you. During these past years I received a lot of support from you, both at a professional and at a personal level, and for that I want to thank you. Without you this thesis would not have been the same and so it is also a bit yours.

First, I would like to thank my promotor, **prof. Albert Schenning**, and co-promotors, **prof. Cees Bastiaansen** and **dr. Michael Debije**. Dear **Albert**, I remember that after my job interview with you I was convinced that doing a PhD at SFD under your supervision would be one of my best decisions in life. I am happy to say after four years that I was not wrong. You are an extraordinary supervisor that offers a well-balanced amount of guidance and freedom to your students. You taught me how to focus, be more concise (except when giving acknowledgements), and showed me how good stories are told. For all these fantastic enriching years, I want to thank you. Next in line is **Cees**: I gladly enjoyed our meetings and your tough questions. You always want to go one step ahead (or back) on the discussion. Your mind is focused on the application of the projects, which was challenging but it gave me new perspective on what I was doing and why. For all the interesting discussions, I thank you. **Michael**, together we have supervised many students and I must say that I admire your patient and creativity. Also, your passion for science and (crazy) ideas on what to try next have been a source of inspiration. I very much appreciate all your guidance and help through these years and I enjoyed all the non-scientific discussion too. Thanks!

Secondly, I would like to thank the rest of my graduation committee: **dr. Taylor Ware**, **prof. Jaap den Toonder**, **prof. Patricia Dankers**, and **dr. Larisa Florea**. **Taylor**, **Jaap**, and **Patricia**, I hope that you have enjoyed reading this thesis and I appreciate the time that you took to carefully assess it. **Larisa**, our long-lasting collaboration have happened via many enjoyable and productive visits to Dublin, at least most of them (let's not talk about the snow incident!), that led to two beautiful publications. Your pool of ideas has no-end and you spark an admirable enthusiasm for your work. I loved our online meetings and brainstorming session; they were always a shot of energy to continue with the projects.

A key partner of the research conducted in Chapter 2-3 was **dr. Colm Delaney. Colm**, your passion and creativity are amazing! Your curious mind, or better phrased: your thirst for liquid crystal knowledge, was a joy to experience. Many thanks for taking me and **Larisa** to unique and cool place to eat during our lunch breaks. I will always remember your performance playing the concertina; I hope to hear it again soon! Furthermore, **dr. Li Liu** thanks for all the time spent in the lab together to make Chapter 4 and the fibers paper possible. I always enjoyed discussing and designing experiments with you. Likewise, **Akhil Peeketi** and **dr. Ratna Annabattula** were essential contributors to Chapter 5. Thanks so much for performing the computational work necessary to understand our experimental results. Moreover, I would like to also thanks **dr. Tom Engels** and **dr. Nadia Grossiord** for their help also on Chapter 5. **Tom** for providing useful inside and ideas behind the mechanism responsible for the observed tendencies and **Nadia** for facilitating the most important part of the project: the PEI sheets! Finally, I would like to thank all the students that have contributed with their end projects to the research presented here: **Fateme**, **Stefan**, **Rik**, **Robin**, and **Robin**.

Furthermore, I would like to thank my partners from the **DynAM** consortium. During these four years we have kept bi-yearly meetings that have served as check-point for the direction of the projects while offering a more industrial perspective of their value; thanks **dr. Francesco Pizzocolo** and **dr. Tessa ten Cate** for organizing them! Many thanks too to **prof. Rint Sijbesma**, **dr. Hans Heuts**, **Huiyi Zhang**, **Soumabrata Majumdar**, **prof. Lorenzo Moroni**, **dr. Matt Baker**, **Francis Morgan**, and **dr. Aldana Agustina** for the fruitful discussions. To the PhD students, good luck finishing the theses!

The other staff members of SFD also deserves a big thanks. **dr. Danqing Li** and **prof. Dick Broer**, I want to thank you for your smart ideas and suggestion on how to fix problems or for helping to create striking demonstrator for my projects. **Dick**, I will always remember your good sense of humor and creativity during our meetings when working on the light-responsive fibers together with **dr. Li Liu**. Also, I want to thank **dr. Johan Lub**, internally known as the SFD police, for his help on synthetizing a suitable chiral dopant for Chapter 3 and for making sure that there are no mistake drawing or naming molecules at SFD. Additionally, I would also like to thank **Audrey Debije** for contributing that every piece of work at SFD has perfect grammar and readability. Finally, many thanks to: **Marjolijn Voragen** and **Tom Bus**. You both make sure that everything goes smoothly every day; without your crucial work we couldn't work as well as we do now. **Tom**, thanks for providing interesting topics to discuss during lunch. **Marjolijn**, thanks for your inside on many practical aspects. Furthermore, thank you for giving me the opportunity to organize several SFD events; despite the stress, and sometimes last-minute chaos, they were always the best SFD event ever! (or so **Albert** always said, or lied?)

My PhD experience would not had been the same without all the great colleague at SFD (or borrowed from SMO). The atmosphere of the group was unique and difficult to find elsewhere. The lunches always had fun and weird conversations, on Thursdays, thanks to **Gilles**, we religiously went to the F.O.R.T. to have some beers, and we had now and then amazing karaoke nights at the Amazing. For making these past years remarkable, a super-big thanks to **Alberto**, **Annelore**, **Arne**, **Daniëlle**, **Davey**, **Dirk-Jan**, **Ellen**, **Eveline**, **Fabian**, **Gilles**, (big) **Jeroen**, **Jeroen Sol**, **Li**, **Marina, Matthew**, **Patricia**, **Pei**, **Roel**, **Rob**, **Sarah**, **Sean**, **Sebastian**, **Shajesh**, **Simon**, **Sterre**, **Stijn**, **Yari**, **Yuanyuan**, **Xinglong**, **Wilson**, and the rest of the incredible family of SFD.

Some people that have already been thanked in the previous paragraph deserve additional mention. To the Wednesday swimming crew: **Eveline**, **Davey**, **Ellen**, en **Gilles**, bedankt dat je me de afgelopen jaren fit hebt gehouden; ook al werd er meer geroddeld dan hard gezwommen. **Gilles**, bedankt om me altijd te ontvangen als ik uitging in Eindhoven en om ervoor te zorgen dat de borrel bij de F.O.R.T. op donderdag altijd doorging. **Davey** en **Eveline**, bedankt om altijd zo goed voor me te zorgen en spelletjesavonden te organiseren. **Simon**, ik heb enorm genoten van ons gesprekken over vanalles en nog wat en je advies over nieuwe Netflix-series. Je bruiloft was een geweldig feest, vraag maar aan je schoonzus en schoonmoeder! Tegen mijn geliefde kantoorgenoten **Stijn** en **Sean** moet ik zeggen dat het een eer was om met jullie het kantoor te delen. Bedankt voor het accepteren van mijn rommelige tafel en dat ik altijd wat muziek mocht opzetten. **Daniëlle**, bedankt dat je met mij op avontuur bent gegaan om wat organische chemie te doen. Het was geen groot succes, maar we hebben het in ieder geval geprobeerd. Bedankt voor alle leuke momenten en gin-tonic-avonden. **Marina**, como tu disseste anteriormente: obrigada por sempre refletires o meu caos. Estes últimos anos não teriam sido os mesmos sem as várias

discussões que tivemos sobre os tópicos mais diversos. Gosto sempre de conversar contigo! Mal posso esperar para continuar a praticar a arte de fazer caipirinhas na tua nova casa em Portugal!

Now, it is time to thank my two amazing paranymphs: **Patricia** and **Jeroen**. También es el momento de practicar mi castellano. **Patri**, creo que el proverbio "Dios los cría y ellos se juntan" nos describe bastante. Desde el principio tuvimos una afinidad mutua inmediata. Estos años hemos vivido muchas cosas juntos y mutuamente hemos montado la montaña rusa emocional que es hacer un doctorado. Muchas gracias por todo tu apoyo. Por fin esto ya se ha acabado. ¡Tú que puedes, huye a un país más cálido que aquí hace un frío que te cagas! Aunque me abandones a la intemperie, tu casa siempre será mi casa (¿Has visto lo que he hecho ahí?) y no tengo ninguna duda que seguiremos siendo amigos por el resto de nuestras vidas. No lo olvides: ¡eres una persona extraordinaria! Nu schakelen we over op het Nederlands. **Jeroen**, er zijn zoveel dingen waarvoor ik je moet bedanken dat ik niet zeker weet of het me gaat lukken. Hoewel het niet gepland was, deden we het doctoraat zij aan zij. Onze onderzoeksprojecten waren met elkaar verweven en als resultaat wist ik op elk moment wat jij aan het doen was en jij ook wat ik deed. Dit maakte jou de perfecte collega om te komen helpen, brainstormen en rare resultaten te bespreken. Niet alleen voor je kennis, maar ook voor je humor en creatieve geest. Ik vond het erg leuk om samen met jou het practicum van de OGO te begeleiden, vooral om de studenten te benadrukken dat we hele mooie figuren wilden. Ik wil je ook bedanken voor het introduceren van mij in de Adobe-wereld (of niet, want nu ben ik net zo geobsedeerd als jij) en voor het altijd hebben van positieve feedback over hoe ik mijn figuren kan verbeteren. Als mijn figuren mooi zijn, is dat dankzij jou. Ten slotte, omdat dit erg lang begint te worden, zijn onze schrijfsessies een van mijn take-aways van het doctoraat, zeer constructief en leuk tegelijkertijd. Maar onthoud, de volgende keer moeten we samen een Mario Car-race doen om de eerste auteur te bepalen, en ik zal winnen! Finally, **Jaime** and **Maartje** also deserve a big thanks for always welcoming me into their homes and for being part of many fun evenings.

Let's move now to Tilburg: "Je bent er!". Ik wil een groot bedankje geven naar: **Amanda**, **Debbie**, **Eva**, **Maikel** en **Tessa**. Bedankt dat jullie mijn vrienden zijn geworden en dat jullie altijd de moeite hebt genomen om me geïntegreerd te laten voelen. Ik waardeer vooral alle goede momenten, feesten en vieringen die we samen hebben doorgebracht. **Amanda**, bedankt voor het bingewatchen en het samen genieten van alle dramatische realityshows. Het is altijd leuk om met je om te gaan. **Eva**, bedankt voor het altijd steunen en geloven in mij. Zonder jou had ik mijn wederhelft nooit gevonden. **Debbie**, **Maikel** en **Tessa**, bedankt dat jullie gek waren en dat jullie carnaval en elk ander feest uniek, leuk en gedenkwaardig maakten. Met vrienden zoals jij verveel je je nooit! Enne **Debbie**... Ik heb nu eindelijk twee PhD's!

Ara, amics i amigues, en català! Vull també donar les gràcies al grup Hotmaileros: **Alba**, **Alex**, **Anna**, **Arnau**, **Axel**, **Blanca**, **Esteve**, **Gerard**, **Judith**, **Laura**, **Maria**, **Marina**, **Marta**, **Mercè**, **Nadia**, **Xess**. Des de la distància sempre heu estat al meu costat. Aprecio molt el temps i l'esforç que feu cada cop que vinc per terres catalans per veure'ns. El millor de la nostra relació és que cada cop que ens veiem és com si el temps no hagués passat; això és fantàstic! Venir-vos a veure ha estat, és, i sempre serà, un xute de felicitat. Moltíssimes gràcies per tots aquests anys d'amistat. Us estimo molt a tots i ja sabeu que teniu casa aquí, a Tilburg. Esteu sempre convidats! També vull donar les gràcies a la **Mireia**, qui ha estat des de l'institut una persona constant al meu costat i qui m'ha donat molt de suport personal i professional. Ja saps que ets la meva germana adoptada i t'estimo molt! **Mireia**, quan vulguis tornem a ballar la cançó del Coconut per Harrys Nilsson.

Hannie, **Ap**, **Opa**, **Aniek**, **Jorg**, **Boudewijn**, **Manoek**, **Deniz** en de rest van de **Geboertjes** bedankt dat jullie mij met open armen als onderdeel van de familie hebben ontvangen. Het duurde niet lang voordat ik me geaccepteerd en op mijn gemak voelde bij jullie. Ik waardeer echt de liefde die jullie me hebben gegeven. Zonder jullie had ik me niet zo goed in Nederland gevestigd. Jullie hebben allemaal een speciaal plekje in mijn hart.

Als **pares**, al meu **germà**, a l'**Anna**, en **Pau** i la **Fiona** us vull agrair tota l'estima que m'heu donat al llarg de la meva vida; i els més petits, des que heu arribat. **Mama** i **Papa**, tot el que he aconseguit és gràcies a vosaltres. Tots els meus èxits són també vostres. Sense la vostra educació, valors i estima no ho hauria aconseguit. **Miquel**, gràcies per estar sempre al meu costat i ser un germà gran comprensiu, divertit i model a seguir. També vull donar les gràcies a la resta de la família **del Pozo Ortiz**, **Puigs Hors** i per descomptat també als **Vegas**! No podria haver triat una família millor.

Wart, je verdient mijn grootste dankbaarheid. Met jouw liefde en steun heb je dit doctoraat mogelijk gemaakt. Er zijn geen woorden die correct uitdrukken hoeveel je voor mij betekent. Mijn partner in crime, zullen we naar de volgende uitdaging gaan? Een wijngaard in Toscane of toch een jacht? Wat zou het zijn...?

Moltes gràcies a tots!

Marc

Curriculum Vitae

Marc del Pozo Puig was born in Girona 1993, Catalonia. In 2015 he received a Bachelor's degree in Nanoscience and Nanotechnology at the Universitat Autónoma de Barcelona (UAB). Marc did his bachelor project at the Institut de Ciència de Materials de Barcelona (ICMAB) in nanocomposites of graphene and an internship at the Electron Microscopy Unit at the Catalan Institute of Nanoscience and Nanotechnology (ICN2). Complementary to his undergraduate courses, he undertook three extracurricular research stays at the UAB, ICN2, and Queen Mary University of London (QMUL). In 2015 he moved to the Netherlands to perform the research master degree in Nanomaterials at the Utrecht University (UU). Marc performed his master's thesis at the Molecular Biophysics group at the UU in synthesis and characterization of core-shell particles. After a six months internship at the University of Amsterdam (UvA) in anisotropically-shaped magnetic core-shell particles he graduated in 2017. That same year, Marc started his Doctor of Philosophy (PhD) research in the Stimuli-responsive Functional Materials and Devices (SFD) group at the Eindhoven University of Technology (TU/e) under the supervisions of prof. Albert Schenning, dr. ing. Cees Bastiaansen, and dr. Michael Debije on 4D printing of liquid crystals materials. The most important results of his research are presented in this thesis.

List of Publications

Publications related to this work

1. <u>M. del Pozo</u>, J. A. H. P. Sol, A. P. H. J. Schenning, M. G. Debije, "*4D printing of liquid crystals: what's right for me?*", Advanced Materials, **2021,** 2104390

2. <u>M. del Pozo</u>, C. Delaney, M. Pilz da Cunha, M. G. Debije, L. Florea, A. P. H. J. Schenning, "*Temperature responsive 4D liquid crystal microactuators fabricated by direct laser writing by two-photon polymerization*", Small Structures, **2021**, 2100158

3. <u>M. del Pozo</u>, C. Delaney, C. W. M. Bastiaansen, D. Diamond, A. P. H. J. Schenning, L. Florea, "*Direct laser writing of four-dimensional structural color microactuators using a photonic-photoresist*", ACS Nano, **2020**, 14, 8, 9832–9839

4. L. Liu, <u>M. del Pozo</u>, S.F. Mohseninejad, M. G. Debije, D. J. Broer, A. P.H.J. Schenning, "*Light tracking and light guiding fiber arrays by adjusting the location of photoresponsive azobenzene in liquid crystal networks*", Advanced Optical Materials, **2020**, 18, 8, 2000732

5. <u>M. del Pozo</u>, L. Liu, M. Pilz Da Cunha, D. J. Broer, A. P.H.J. Schenning, "*Direct ink writing of a light-responsive underwater liquid crystal actuator with atypical temperature-dependent shape changes*", Advanced Functional Materials, **2020**, 50, 30, 2005560

6. <u>M. del Pozo</u>, A. R. Peeketi, J. A. H. P. Sol, S. H.P. van Uden, S. J. D. Lugger, R. K. Annabattula, A. P. H. J Schenning, M. G. Debije, "*Patterned actuators via direct ink writing of liquid crsytals*", ACS Applied Materials & Interfaces, **2021** (*Accepted/In press*)

7. J. A. H. P. Sol, L. Kessels, <u>M. del Pozo</u>, M. G. Debije, "*Responsive photonic liquid crystalline flakes produced by ultrasonication*", Advanced Photonics Research, **2021**, 4, 2, 2000115

Other publications

8. E. B. van der Wee, J. Fokkema, C. L. Kennedy, <u>M. del Pozo,</u> D. A. M. de Winter, P. N. A. Speets, H. C. Gerritsen, A. van Blaaderen," *3D test sample for the calibration and quality control of stimulated emission depletion (STED) and confocal microscopes*", Communications Biology, **2021**, 4, 909

9. Y. Foelen, D. A.C. van der Heijden, <u>M. del Pozo</u>, J. Lub, C. W.M. Bastiaansen, A. P.H.J. Schenning, "*An optical steam sterilization sensor based on a dual-responsive supramolecular cross-linked photonic polymer*", ACS Applied Materials & Interfaces, **2020**, 14, 12, 16896-16902

10. M. Galli, C. J. Fletcher, <u>M. del Pozo</u>, S. M. Goldup, "*Scalable anti-Markovnikov hydrobromination of aliphatic and aromatic olefins*", Organic & Biomolecular Chemistry, **2016**, 14, 5622-5626